B O L T   B E R A N E K   A N D   N E W M A N   I N C

C O N S U L T I N G · D E V E L O P M E N T · R E S E A R C H

Report No. 1431
Job No. 11211

TRANSMISSION OF SOUND AND VIBRATION TO A SHROUD-ENCLOSED SPACECRAFT

Jerome E. Manning
Richard H. Lyon
Terry D. Scharton

GPO PRICE $ ________

CFSTI PRICE(S) $ ________

Hard copy (HC) 3.00

Microfiche (MF) .65

ff 653 July 65

1 15 October 1966 10
Contract No. NAS5-9601

FACILITY FORM 602

67 18035	
(ACCESSION NUMBER)	(THRU)
183	1
(PAGES)	(CODE)
CR 81688	32
(NASA CR OR TMX OR AD NUMBER)	(CATEGORY)

Submitted to:

National Aeronautics and Space Administration
Goddard Space Flight Center
Greenbelt, Maryland 20771

TRANSMISSION OF SOUND AND VIBRATION
TO A SHROUD-ENCLOSED SPACECRAFT

By: Jerome E. Manning, Richard H. Lyon,
and Terry D. Scharton

Prepared under Contract No. NAS5-9601 by
BOLT BERANEK AND NEWMAN INC.
Cambridge, Massachusetts

For

NATIONAL AERONAUTICS AND SPACE ADMINISTRATION

TABLE OF CONTENTS

TABLE OF CONTENTS (cont'd)

TABLE OF CONTENTS (cont'd)

TABLE OF CONTENTS (cont'd) Page

LIST OF ILLUSTRATIONS

LIST OF ILLUSTRATIONS (cont'd)

LIST OF TABLES

LIST OF SYMBOLS

a_2	radius of the shroud model
AF	acoustically fast (see p. 30)
A_i	surface area of the ith element
AL	acceleration level <u>re</u> 1 g (see p. 99)
A_p	area of a radiating panel
AS	acoustically slow (see p. 30)
$c_b, c_f^{(i)}$	bending-wave speed in the ith element
$c_\ell^{(i)}$	longitudinal- (compressional-) wave speed in ith element
c_o	speed of sound in the acoustic media
$c_t^{(i)}$	torsional-wave speed for ith element
$\mathcal{E}_A$	time-average total energy of oscillator A
$E_i^{res.}$	time average total energy of resonant modes in element i
E_n	time-average total energy in modal group n
f	frequency in Hertz (cycles per second)
f_c	critical frequency [defined by Eq. (25)]
f_r	ring frequency [defined in Eq. (28)]
g_o	acceleration of gravity

LIST OF SYMBOLS (cont'd)

h	thickness of the shroud wall
i	constant equal to $\sqrt{-1}$
k	wavenumber magnitude (see p. 40)
k_o	acoustic wavenumber
k_y	axial component of the wavenumber, $k_y = m\pi/\ell$
k_x	circumferential component of the wavenumber $k_x = n/a$
K	static stiffness of the mounting trusses
K_A	spring constant of spring in oscillator A
K_c	spring constant of the coupling spring
ℓ_2	axial length of the shroud
ℓ_{2a}	separation between the base of the shroud and the first ring frame
ℓ_{2b}	separation between the first and second ring frames
L_4	length of the connected edges of the spacecraft
m,n	axial and circumferential mode number, (see p. 39)
M_A	mass of oscillator A
$n_t^{(i)}$	density of torsional modes in the element
$n(f),n$	modal density

LIST OF SYMBOLS (cont'd)

$\overline{n}(f)$	average modal density in a frequency band
$N(f)$	number of modes with resonance frequencies below f
NR	noise reduction [defined by Eq. (80)]
$NR^{(res)}$	noise reduction resulting from resonant shroud motion
$NR^{(nonres)}$	noise reduction resulting from nonresonant shroud motion
P_{inc}	complex amplitude of the incident acoustic wave
P_r	radiating perimeter (see p. 53)
P_{rad}	complex amplitude of the radiated acoustic wave
P_{trans}	complex amplitude of the transmitted acoustic wave
R_A	damping parameter of oscillator A
R_{rad}	radiation resistance [defined by Eq. (51)]
R_6	real part of Z_6
$S_a^{(i)}(f)$	mean square acceleration spectral density (Ref. 13)
$S_p^{(i)}(f)$	mean square sound-pressure spectral density (Ref. 13)
SPL	sound-pressure level re 0.0002 μbar [see Eq. (99)]

LIST OF SYMBOLS (cont'd)

TL	transmission loss [defined by Eq. (74)]
v_A	velocity of oscillator A
V_i	volume of ith acoustic space
V_{panel}	complex amplitude of the infinite-panel velocity
x_1, x_2, x_3	a set of coordinates (shown in Fig. 21)
Z_5	source impedance of element 5
Z_6	input impedance of element 6
Z_6^t	input impedance of element 6 for torsional waves
Z_6^f	input impedance of element 6 for flexural waves
Z_{panel}	infinite-panel impedance to a surface-pressure load
Z_{rad}	radiation impedance of an infinite panel
α_3	absorption coefficient of the interior acoustic space, [see Eq. (59)]
β	cylinder constant [defined in Eq. (28)]
Δ	frequency bandwidth in Hertz
η_i	dissipation loss factor of ith modal group
$\eta_{i,j}$	coupling loss factor from modal group i to j
η_3^{eq}	composite loss factor for the internal acoustic space [see Eq. (76)]
η_A	dissipation loss factor of oscillator A

LIST OF SYMBOLS (cont'd)

θ, r	dimensionless polar coordinates in k-space (see p. 40)
θ	an angle (shown in Fig. 21)
$\kappa_i, \kappa_f^{(i)}$	flexural radius of gyration of ith element
κ_ϕ	polar radius of gyration
λ_c	acoustic wavelength at the critical frequency
λ_o	acoustic wavelength
Π_{AB}	power flow from oscillator A to B
Π_i^{diss}	time-average power dissipated by modal group i
$\Pi_{n,n+1}$	time average power flow from modal group n to modal group n+1
Π_{trans}	time-average power transmitted through the shroud
$\rho_\ell^{(i)}$	lineal density of ith element
ρ_o	volume density of the acoustic media
$\rho_s^{(i)}$	surface density of ith element
σ	dimensionless wavenumber [defined in Eq. (28)]
σ_{rad}	radiation efficiency [defined by Eq. (51)]
$\bar{\tau}$	average sound transmission coefficient [defined by Eq. (73)]
τ_f	torque due to flexure

LIST OF SYMBOLS (cont'd)

τ_t	torque due to torsion
τ_3	torque in x_3 direction (see Fig. 21)
ν	dimensionless frequency [defined in Eq. (28)]
ν_c	dimensionless critical frequency [defined by Eq. (91)]
ϕ	angle of incidence measured from the normal
ϕ_{AB}	oscillator coupling factor
$\overline{\Phi}_{n,n+1}$	group-average mode-to-mode coupling factor between subsystem n and n+1
ω	radian frequency
Ω_f	angular velocity due to flexure
Ω_t	angular velocity due to torsion
Ω_3	angular veloxity in x_3 direction, (see Fig. 21)
$\langle\ \rangle_t$	average with respect to time

TRANSMISSION OF SOUND AND VIBRATION TO A SHROUD-ENCLOSED SPACECRAFT

By: Jerome E. Manning, Richard H. Lyon,
a d Terry D. Scharton

ABSTRACT

An analytical approach toward predicting the flow of vibratory energy to a shroud-enclosed spacecraft is presented. In the approach, two paths of energy flow are considered: first, the acoustical path along which energy flows from the external exciting field through the shroud and interior acoustic space to the spacecraft; and second, the mechanical path along which energy flows from the external field through the shroud and spacecraft mounting-trusses to the spacecraft. Theoretically predicted response levels in octave frequency bands for a model of the OGO spacecraft assembly are presented. These predictions show that the spacecraft response to energy transmitted along the acoustic path is a factor of ten to one hundred greater than the response due to energy transmitted along the mechanical path over the frequency range, 250 to 8000 Hz.

1. INTRODUCTION

The goal of the studies reported here has been the development of an analytical procedure for predicting the mechanical and acoustic excitation environment of a shroud-enclosed spacecraft. An estimation procedure known as statistical energy analysis is described. This estimation procedure is applicable to prediction of the vibration environment of any spacecraft-shroud assembly. To illustrate the procedure, we have focused our attention on prediction of the vibration environment for a class of spacecraft-shroud assemblies that are similar to the OGO spacecraft assembly. The basic spacecraft structure for this class of assemblies is an array of panels that are supported by a series of trusses. The trusses are connected to a ring frame that is, in turn, connected to the shroud. The predictions in this report give spectral acceleration levels on the spacecraft panels in terms of the gross structural properties of the assembly. Fine details of the assembly, such as the exact details of the shroud/ring-frame/mounting-truss connection, are not needed for the predictions. As a further example of the predictions, numerical results are obtained for a model of the OGO spacecraft. These results show that, for this particular assembly, the dominant excitation of the spacecraft is by energy transmitted from the exterior sound field through the interior acoustic space; the excitation by energy transmitted along the mounting trusses is of lesser significance. With certain reservations, we can regard this result as fairly general for the class of spacecraft assemblies considered here.

The major limitation of the prediction method is that it is applicable only at high frequencies in which many modes of each structure are resonant in each octave band. For the OGO assembly and other assemblies of similar size, the lower-frequency limit of the predictions is approximately 200 Hz. Another limitation of the prediction method is that it requires knowledge of the damping properties of the structural and acoustic elements in the assembly. In this report, we do not present an analytical method for predicting the damping of the structures. Rather, we have used empirical relationships of which we are reasonably confident. We expect that the dissipation-loss factors predicted by these empirical relationships will be within a factor of 5 of the true dissipation-loss factor for the structure.

Our model of the spacecraft-assembly is briefly described in the following sections of this chapter. In addition, we give brief descriptions of the environment considered in the analysis and the prediction scheme itself. In Chapter II, the prediction scheme is discussed in greater detail. The power-balance equations that are used in the analysis are derived from a basic result for two coupled oscillations. In Chapter III, we predict the environment due to energy transmitted by the acoustic space. Similarly, in Chapter IV, we predict the environment due to energy transmitted by the mounting trusses. The organization of Chapter III parallels that of Chapter IV. First, the model is described. Then, using the results of Chapter II, power-balance equations for the model are obtained. Next, the necessary parameters are derived in terms of the basic structural properties of the system. The spectral response of each element in the assembly is obtained in terms of their structural and acoustic properties. Finally, numerical results are obtained for a model of the OGO spacecraft.

In Chapter V, the predictions of the previous two chapters are combined. This gives the over-all spacecraft-panel environment due to acoustically and structurally transmitted energy. In Chapter VI, we discuss the conclusions that can be obtained from this study. Appendix A of this report describes an experimental study that could be conducted to complement the analytical prediction. A list of parameters that are appropriate for the OGO assembly are given in Table I.

1.1 Description of a Model that Retains the Vibrational Response and Transmission Properties of the OGO Spacecraft-Shroud Assembly

The estimation procedures described in this report could be used for any spacecraft-shroud assembly. To help fix our ideas, however, we will make reference to the structure shown in Fig. 1. This structure is an idealized model of the OGO spacecraft-shroud assembly. In this model, the shroud is a rib-stiffened cylindrical shell. The base of the shroud attaches to a mounting ring frame which provides the principal support for the spacecraft. The spacecraft proper is attached to the ring frame by a series of mounting trusses. The actual OGO spacecraft is a complicated aggregation of solar panels, antennas, center-of-gravity control rods, jets, instruments, etc. We have simplified it to be simply a rectangular box of flat panels.

The mechanical descriptors of these major segments will be put in a form that is as general as possible, to allow for different kinds of construction. One-dimensional structures such as ribs, ring frames, and trusses are described in terms of lineal density (mass per unit length), radii of gyration for bending and torsional motion, radius of curvature, and over-all length. Panellike structures such as the shroud and the spacecraft box are described by surface density (mass per unit area), radius of gyration for bending, and over-all dimensions, including radius of curvature. The elastic properties of the elements are described by Young's modulus or by the longitudinal wavespeed.

1.2 Definition of the Environment Considered in the Analysis

The highest pressure load sustained by the shroud is achieved during the launch and the maximum q phases of the flight. During the launch, excitation is due to the sound waves that are generated by the turbulent exhaust impinging on the shroud from below. During periods of high dynamic pressure, excitation is due to convected turbulent pressure fluctuations that arise in the boundary layer of the flow about the shroud.

In a sound field, there is a distinct relationship between frequency (f) and wavelength (λ) scales that is governed by the speed of propagation, i.e.,

$$f\lambda = c_o, \tag{1}$$

where c_o is the speed of sound. In turbulent flow, by contrast, there is no specific relationship between frequency and wavelength, and, in fact, a particular wavelength of pressure disturbance may have a complete spectrum of excitation frequencies. The result of this distinction is that a pressure spectrum measured at the surface of the shroud may give rise to two completely different mechanical-vibration-response spectra, depending on whether the pressure field is due to sound or a turbulent boundary layer. The relative efficiencies of sound fields and turbulent flow in producing mechanical excitation has been discussed in Refs. 1 and 2.

If one knows the mechanical power absorbed from the environment by groups of modes that are similarly coupled to the interior acoustic field, then the analyses developed in this report will apply equally well, whether that power is due to aerodynamic or acoustic excitations. For the purposes of calculating the power absorbed by each group of modes, however, we shall assume that the exterior field is a reverberent sound field. This means that there is equal probability for acoustic energy to be incident from all angles. As we shall see, this has a particularly simple interpretation theoretically, and represents a relatively easy condition to achieve experimentally. If the signal is filtered into narrow frequency bands, the spatial crosscorrelation pattern for such a field is isotropic and has the form shown in Fig. 2, where λ is the acoustic wavelength at the center frequency of the band.[3]

1.3 A Brief Description of The Prediction Scheme

An examination of Fig. 1 will show that there are two primary paths along which energy can be transferred to the spacecraft structure. One of these is an acoustic path through the interior volume of the shroud and by acoustic transduction into the spacecraft panels. The second is a mechanical path through the mounting truss and into the base of the spacecraft. Figure 3 shows the major elements involved in the transmission of energy from the shroud to the spacecraft. One of the goals of this study is to assess the relative importance of the acoustic and the mechanical excitation. Thus, we shall treat these paths separately in the prediction calculations.

In addition to this separation into transmission paths, we also make a distinction between energy transferred by "resonant" and "nonresonant" motions. If we consider a specific frequency band, then, by resonant transmission, we mean energy transferred by vibrational modes of the connecting system that resonate in this band. By nonresonant transmission, we mean energy transferred in that frequency band by the motion of modes of the connecting system that are resonant outside of that frequency interval.

The standard calculations of sound transmission by building walls are usually based on a "mass-law" nonresonant behavior of the walls. This is because, in a wall, modes that are well-coupled to a sound field (their wavelength is longer than the acoustic wavelength) are excited by a sound wave at frequencies above their natural resonances. Therefore, they respond in a mass-controlled nonresonant fashion. The collective motion of such modes gives a fairly large amount of sound transmission, even though the amplitudes of the wall motion may be quite small. In contrast, although there can be considerable wall motion due to modes that resonate in the test frequency band, the contribution of these modes to the sound transmission is small, since they are usually inefficient sound radiators.

In space vehicles where the structures are lightweight and flexurally stiff and there is a small distance between supporting frames and stringers, the amount of acoustic energy transmitted by the resonant motions is increased in comparison with the amount transmitted by nonresonant motion. Energy transmission in such systems is, therefore, a competition between resonant modes that respond with large amplitudes but are inefficient in transferring acoustic energy and nonresonant modes that have small response amplitude but are efficient acoustic-energy-transfer agents. The analysis developed in this report considers both types of energy transfer and attempts to assess the relative role of each.

The basic approach that we use to develop the prediction methods is that of statistical energy analysis[4]. This approach, which is outlined in the following chapter, treats a complex system as a set of modes that are coupled together more or less intimately, depending on the structural configuration. The motion of each section or element of the structure is determined by the energy of the modes that describe its motion. In this sense, the response of acoustical and mechanical elements is described by precisely the same type of variable.

A basic result of statistical energy analysis allows us to predict power transfer between sets of modes that are excited to unequal energies in the same frequency band. Using the laws of energy transfer, it is then possible to build up a fairly simple prediction of the average energy distribution in a complex system. If more information than the expected mean value of vibration is desired, then it is possible to build up estimates of variance and construct confidence coefficients for "estimation intervals." Unfortunately, however, variance calculations become very complex for transmission problems, and it will not be feasible to develop them for the present application.

2. AN OUTLINE OF STATISTICAL ENERGY ANALYSIS

In this chapter, we discuss the main ideas or concepts of the statistical energy analysis of vibration response and transmission. A complete recapitulation of all the theoretical developments and applications that have been made of this type of analysis is not possible or desirable in this report. The reader is referred to Ref. 4 for a more complete discussion. It is possible, nevertheless, to outline the main results in such a way as to give an appreciation of the role that various components play in the calculations, and the way in which the present application is related to other applications in the literature.

2.1 A Fundamental Observation on Power Flow Between Two Oscillators Excited by Wide-Band Noise

Statistical energy analysis is useful because of a fundamental observation on the energetics of two coupled linear oscillators excited by wide-band* random-noise sources. If one calculates the time-average power flow between these two oscillators, one finds that it is proportional to the difference in their time-average total energies[5], and that the power flow is always from the oscillator of higher energy to that of lower energy. This result was first established by Lyon and Maidanik,[6] for the case of oscillators with small linear coupling and damping. Recently, Scharton[7] has shown that this result is independent of the strength of the coupling between oscillators if their energies are suitably defined.

---

*By wide-band noise, we mean noise with a spectrum that encompasses the resonance frequencies of both oscillators.

For example, let us consider the pair of stiffness coupled oscillators shown in Fig. 4. The time-average total energy of oscillator A is defined as

$$\mathcal{E}_A \equiv \frac{1}{2} M_A \langle v_A{}^2\rangle_t + \frac{1}{2} (K_1 + K_c) \langle X_A^2\rangle \tag{2}$$

and the time-average total energy of oscillator B is

$$\mathcal{E}_B \equiv \frac{1}{2} M_B \langle v_B{}^2\rangle_t + \frac{1}{2} (K_2 + K_c) \langle X_B^2\rangle \ . \tag{3}$$

The referenced analyses predict that the time-average net power flow Π_{AB} is given by

$$\Pi_{AB} = \phi_{AB}(\mathcal{E}_A - \mathcal{E}_B) \ , \tag{4}$$

where the coupling factor ϕ_{AB} is given in terms of parameters of the two oscillators and is independent of the source strengths:

$$\phi_{AB} = \frac{K_c{}^2}{K_A K_B} \frac{\omega_A{}^2\omega_B{}^2(\omega_A\eta_A+\omega_B\eta_B)}{(\omega_A{}^2-\omega_B{}^2)^2+(\omega_A\eta_A+\omega_B\eta_B)(\omega_A\omega_B{}^2\eta_A+\omega_B\omega_A{}^2\eta_B)} \tag{5}$$

where

$$\omega_A{}^2 \equiv \frac{K_A+K_c}{M_A} \ , \quad \omega_B{}^2 \equiv \frac{K_B+K_c}{M_B}$$

and

$$\eta_A \equiv \frac{R_A}{M_A\omega_A} \quad , \quad \eta_B \equiv \frac{R_B}{M_B\omega_B} \quad .$$

We note from Eq. (5) that the coupling factor ϕ_{AB} is positive definite, so that the power Π_{AB} always flows from the oscillator of higher average energy to the oscillator of lower average energy. We note also that the coupling factor has a maximum value when the resonance frequencies [defined in Eq. (5)] of the two oscillators coincide. Let us now suppose that oscillator A is excited by an external wide-band noise source but that oscillator B is excited only through its connection to oscillator A. In this event, the dissipated power in oscillator B must equal the power that flows to it from oscillator A. The power dissipated by oscillator B is given by

$$\Pi_B^{\text{diss}} = \omega_B \eta_B \mathcal{E}_B \quad . \tag{6}$$

Equating relations (4) and (6) results, then, in an expression for the time-average total energy ratio of the two oscillators,

$$\frac{\mathcal{E}_B}{\mathcal{E}_A} = \frac{\phi_{AB}}{\phi_{BA} + \omega_B \eta_B} \quad . \tag{7}$$

This particular result is appropriate only for the case where two oscillators are coupled together. In the following sections of this chapter, we will consider power balance equations for more-complex multimodal systems.

2.2 Power Flow in Multimodal Systems Excited by Wide-Band Noise

Armed with our fundamental result on the time-average power flow between two coupled oscillators excited by wide-band noise, let us now consider the system diagrammed in Fig. 5. This system is divided into two subsystems, each of which has several modes of oscillation and is excited by wide-band noise sources. The attachments between the subsystems correspond to the coupling spring K_c in Fig. 4, and result in a power flow between the modes of vibration of subsystem n and subsystem n+1.

The modes of each subsystem can be treated as a set of coupled oscillators. Based on the results when only two oscillators are coupled together, we hypothesize that the power flow between any two of the coupled oscillators in subsystem n and n+1 is proportional to the difference in their time-average total energies. Then, the power transferred from subsystem n to subsystem n+1 can be given as

$$\Pi_{n,n+1} = \sum_A \sum_B \phi_{AB}(\mathcal{E}_A - \mathcal{E}_B) \quad , \tag{8}$$

where summation over A refers to a summation over all modes in subsystem n, summation over B refers to a summation over all modes in subsystem n+1, and ϕ_{AB} is the coupling factor between mode A and mode B.

We will assume that the subsystems are so chosen that one of the following conditions holds:

a. the coupling factors between modes are all equal,

b. modes within the same subsystem have the same time-average total energy,

c. the time-average total energy of a mode is independent of its coupling to any particular mode in the other subsystem.

In a practical application of statistical energy analysis, the above conditions are usually not satisfied exactly. However, in most cases, the modes of a system can be divided such that all of the above conditions are approximately satisfied. The need for and significance of the assumption that one of the above conditions hold is discussed further in Ref. 4.

If one of the above conditions is valid, then the mode-to-mode coupling factors in Eq. (8) can be replaced by an average coupling factor between a mode in n and a mode in n+1. The indicated summation can now be carried out to give

$$\Pi_{n,n+1} = \overline{\Phi}_{n,n+1} N_{n+1} N_n \left[\frac{E_n}{N_n} - \frac{E_{n+1}}{N_{n+1}} \right] , \qquad (9)$$

where $\overline{\Phi}_{n,n+1}$ is the average mode-to-mode coupling factor between the two subsystems, E_n is the total time-average energy of a subsystem n, and N_n is the number of modes in subsystem n.

Up to this point, we have restricted our discussion to systems excited by wide-band noise. In the calculations to follow, however, we wish to find the vibrational response of the structural elements in bands of frequency. Toward this end, we will consider, in the next section, power flow in a multimodal system excited by a band of noise. As it turns out, the basic calculations of time-average power flow between two groups of modes excited by wide-band noise can still be used to advantage.

2.3 Power Flow in Multimodal Systems Excited by a Band of Noise

Let us consider a multimodal system excited in a band of frequencies. We can divide the modes of this system into resonant and nonresonant modes according to whether or not their resonance frequencies are within the band of excitation. We can further divide the modes into groups of modes which are similarly coupled to modes in other groups. The power flow between two groups of similarly coupled resonant modes can be given by Eq. (9), since the excitation band encompasses the resonance frequencies of the modes within these groups. The power-flow interactions with groups of nonresonant modes, however, cannot be predicted by the results of the last two sections, since the resonance frequencies of these modes lie outside the band of excitation.

Power flow between resonant and nonresonant modes is generally not proportional to modal energy difference. Fortunately, the response and energy transmission of nonresonant modes can usually be calculated by more-classical vibrational analyses. For example, the response and energy transmission of nonresonant modes in a panel excited by an acoustic field are given by the so-called "mass law".[8] In the formulation to follow, we assume that the nonresonant response and power-flow interactions are known.

Let us consider the system diagrammed in Fig. 6. This system is excited by a band of noise and has accordingly been divided into groups of resonant modes and groups of nonresonant modes. We assume that the modes within each group are similarly coupled to modes in other groups.

If the vibration of this system has reached a time-average equilibrium level, then in the band of excitation we can identify an amount of power received by the nth group from the environment, denoted Π_n^{in}. We can also identify the power dissipated, Π_n^{diss}, the power flow to the other groups of resonant modes, $\Pi_{n,n-1}$ and $\Pi_{n,n+1}$, and the power flow to the nonresonant groups of modes, $\Pi_{n,m-1}^{NR}$ and $\Pi_{n,m+1}^{NR}$. Since the modes are at equilibrium, a power-balance equation for the nth group of modes is

$$\Pi_n^{in} = \Pi_{n,n+1} + \Pi_{n,n-1} + \Pi_n^{diss} + \Pi_{n,m-1}^{NR} + \Pi_{n,m+1}^{NR} \quad . \qquad (10)$$

The power dissipated in the frequency band of excitation by the nth group of resonant modes is classically given in terms of a dissipation or internal loss factor η_n:

$$\Pi_n^{diss} = \omega\eta_n E_n, \tag{11}$$

where ω is the center frequency of the excitation band and E_n is the time-average kinetic energy in the nth group. For consistency with the dissipation loss factor when E_{n+1} approaches zero, we define a coupling loss factor $\eta_{n,n+1}$ by

$$\Pi_{n,n+1} = \omega\eta_{n,n+1} N_n \left[\frac{E_n}{N_n} - \frac{E_{n+1}}{N_{n+1}} \right] , \tag{12}$$

where N_n is the number of modes in the nth group. Comparison of this equation with Eq. (9) indicates that the coupling loss factor is related to the average mode-to-mode coupling factor by the equation

$$\omega\eta_{n,n+1} = \Phi_{n,n+1} N_{n+1} \quad . \tag{13}$$

For a general system, we do not know the exact number of modes in each resonant group. However, it turns out that we can arrive at a reasonably good estimate from the modal density. Modal density is defined as the limit, as the bandwidth approaches zero, of the expected number of modes that occur in a given frequency band divided by the bandwidth:

$$n(f) = \lim_{\Delta \to 0} \frac{N(f+\Delta) - N(f)}{\Delta} , \tag{14}$$

where n(f) is the modal density, N(f) is the average number of modes with resonance frequencies below f in an ensemble of systems, and Δ is the bandwidth. Quantitatively, the modal density is the number of modes per unit frequency, although of course that number may be considerably less than unity.

For our calculations we will find it convenient to use the average modal density over a band of frequencies. This average density is defined as

$$\overline{n}(f) = \frac{N(f + \frac{\Delta}{2}) - N(f - \frac{\Delta}{2})}{\Delta} \quad , \tag{15}$$

so that the number of modes of the nth group in the frequency band Δ is simply

$$N_n = \overline{n}_n(f)\Delta \quad . \tag{16}$$

The power-balance equation, Eq. (10), can now be expressed in terms of the loss factors, modal densities, and time-average total energy of each group of modes, through Eqs. (11), (12), and (16):

$$\Pi_n^{in} = \omega\eta_{n,n+1} \; \bar{n}_n\Delta \left[\frac{E_n}{\bar{n}_n\Delta} - \frac{E_{n+1}}{\bar{n}_{n+1}\Delta} \right]$$

$$+ \omega\eta_{n,n-1} \; \bar{n}_n\Delta \left[\frac{E_n}{\bar{n}_n\Delta} - \frac{E_{n-1}}{\bar{n}_{n-1}\Delta} \right]$$

$$+ \omega\eta_n \, E_n + \Pi_{n,m-1}^{NR} + \Pi_{n,m+1}^{NR} \quad , \tag{17}$$

where Δ is the bandwidth of the frequency band being considered. Similar power-balance equations can be obtained for the other groups of resonant modes. These, together with Eq. (17), form a set of linear equations that can be solved for the energy of the resonant modal groups in terms of the power flows from the environment and the nonresonant modal groups, the loss factors, and the modal densities. We assume that the needed power flows can be calculated by classical methods.* It remains, then, to find the loss factors and modal densities. These must be either calculated or estimated on the basis of experiment. In this report, we shall use the former approach. However, equally valid experimental methods are described in Appendix A.

---

* In Sections 3.5 and 4.5, this will be found to be a valid assumption for the problem that we are considering.

2.4 Calculation of Loss Factors and Modal Densities

In this section, we deal with the procedures for calculating the coupling loss factors, dissipation loss factors, and modal densities.

Two different approaches are possible in the calculation of a coupling loss factor. The first approach can be used when the "uncoupled systems" are well defined, with calculable normal modes of vibration. Then one can consider the system coupling to be a series of mode-by-mode interactions. This approach reduces the system to modal interactions of the type shown in Fig. 4. In such a system, it is possible to obtain the modal-coupling loss factor by direct computation. The interactions between groups of resonant modes can then be computed and statistical averages of these interactions can be performed. Such an approach was the basis for the calculations in Ref. 9, and it has been used to compute the interaction between a simple linear oscillator and a vibrating plate in Ref. 10.

A second approach was suggested by the calculations in Ref. 10, which showed that the average power flow between the mass-spring oscillator and a random ensemble of plates was the same as that between the oscillator and an infinite plate. The generation of average interactions by the consideration of infinitely extended systems has also been utilized and was employed in the calculation of the coupling factors between beams and plates and between connected plates, in Refs. 10 and 11. The equivalence between the average interaction of finite systems (where one takes the average by assuming that the resonant frequencies of the modes are equally probable over some frequency interval) and the interaction of infinite systems has been demonstrated in a few particular instances and has a strong intuitive appeal, but it has not yet been given the solid analytical foundation that would establish it as a general theorem. It is, nevertheless, the approach that we shall take for the calculations in this study.

In using the second approach, we imagine that a mechanical wave in one of the two connected systems is incident on the junction between them. The amount of power that flows to the second system is computed by imagining that the junction is severed and establishing and "unloaded" motion of the junction point. This motion then acts as a source of power transfer through the "internal impedance" of the exciting system into a "load impedance" of the second system. For this particular direction and type of wave incidence on the junction, the power flow is expressible in terms of a ratio of two impedances of the incident system. This approach is particularly valuable, since many of these impedances have been previously calculated and tabulated.[29] One can then average over directions of incidence of the wave (where this is appropriate) and calculate an average power flow between the systems. The intensity of the incident wave establishes the strength of the "reverberant field" in the exciting system.

The dissipation loss factors cannot be calculated theoretically at the present time. However, an empirical estimate of these factors based on a number of past experimental and field results can be made. In the absence of any experimental evidence, these estimates can be used, but of course with some uncertainty.

It has long been known that one does not need to calculate the modes of a system in detail in order to achieve useful expressions for the modal density at high frequencies. A well-known theorem by Weyl[12] shows that at sufficiently high frequencies, the modal density of three-dimensional spaces depends only on the total volume of the space and that the modal density of two-dimensional spaces depends only on the area. These asymptotic results have long been used in the theory of specific heats of crystals and in calculating the modal density of acoustic spaces. They imply that one can find the modal density of an irregularly shaped plate by computing the modal resonance frequencies of a simply supported plate having the same area. The detailed boundary conditions are important in establishing the precise resonance frequencies, but the average frequency separation of the modes depends only on the total area of the plate. Similarly, the modal density of truss systems can be found by computing the modal resonance frequencies and their distribution in a simply supported beam having the same total length as the truss system. We shall make use of specific examples of such calculations in later sections of this report.

In addition to implying an ease of calculation of modal density, Weyl's results also suggest that the modal density of combined systems--e.g., a beam that can carry flexural and torsional waves simultaneously--can be calculated simply by adding the modal densities of each component of the system or of the motion. This is true because, if modal density is proportional to volume, then the modal density of two volumes is simply the modal density of the combined volume or, equivalently, the sum of the modal densities of the component systems.

The concept behind the simple asymptotic approach has been used to calculate the modal density for beams, plates, and cylindrical shells. In all cases where the experiment has been able to count effectively the modes of vibration, the simple asymptotic formulas have been shown to be surprisingly accurate.

2.5 Review of Assumptions Made in Statistical Energy Analysis

Before we proceed with specific calculations of the energy transmission in the spacecraft-shroud assembly, it is perhaps wise to review some of the assumptions that are to be made in the analysis.

Most of the assumptions that we mention here are the result of our selection of statistical energy analysis as a means of calculation. Other assumptions are made for the convenience of specific calculations and applications; these, however, are discussed as they occur.

The first major underlying assumptions that we make are (a) that the motion of the structural systems is linear, and (b) that the coupling between the structural elements and with acoustic fields is also linear. It is not anticipated that significant nonlinear effects will occur at the levels encountered in the OGO system, although sound levels in some of the larger booster-spacecraft systems are approaching a point where nonlinear effects can be expected.

The basic calculations of statistical energy analysis assume that the systems are driven by independent random noise sources with an excitation spectrum uniform at least over the bandwidth of the individual modes. As a practical matter, this means that the excitation acoustic spectrum must be reasonably smooth, without discontinuities or spikes that occur within the bandwidth of a mode. In some special applications, particularly where the modal density is quite high, statistical energy analysis will provide good estimates of response even when the excitation is a single frequency (pure tone). We do not, however, have that condition in the OGO spacecraft-shroud assembly and shall not assume that the calculations that we obtain are in fact applicable to the pure-tone case.

Another major assumption in our analysis is that each mode of a subsystem in a prescribed frequency band (octave, one-third octave, or other) has the same coupling to the modes of the other subsystems or the same modal time-average energy as the other modes in the subsystem. In cases where there is a large discrepancy between the coupling or modal energy between two classes of modes in the same structural element, one has to form subsystems for each class of modes. This was done in Ref. 11, for example, when the power transfer by torsional and bending motion of a beam was considered for each type of motion independently, and the total power transfer was obtained as the summed effect of these two classes of modes. The formation of subsystems for two classes of modes will be necessary for our analysis of the shroud acoustic transmission.

The calculation that one usually makes with statistical energy analysis is the power transfer between a set of modes of one system and a set of modes of a second system in a prescribed frequency interval. It is assumed that a useful statistic of this interaction is the average power flow when the resonant frequencies of the modes are allowed to vary uniformly over the band. The usefulness of such a calculation can frequently be assessed by calculating the standard deviation of the power flow as the resonance frequencies are varied. When the number of modes in the interacting sets are high, then this variance is small and the average calculation gives a good estimate of the power flow at any set of resonance frequency locations. When the number of modes in each set is relatively low, then the variance can be high and an average estimate in itself may have relatively little utility. The variance calculation can be useful in this case, however, in estimating how much change one is likely to find in the energy transfer when slight changes are made in a system and the resonant frequencies of modes are altered.

3. ANALYSIS OF THE ACOUSTIC TRANSMISSION PATH

In this chapter, the transmission of vibratory energy along the acoustic path is formulated in terms of basic structural and acoustic parameters of the spacecraft-shroud assembly. Where useful, specific calculations are made, using parameter values that are appropriate for a model of the OGO spacecraft. These values are listed in Table I.

The elements of the acoustic transmission path are indicated in Fig. 3. A necessary step in our analysis is the replacement of these elements in the actual spacecraft-shroud assembly by idealized models. In selecting models, we have been guided by two basic considerations. First, we have tried to pick models that are idealized enough to be analyzed, but still retain the acoustic response and transmission characteristics representative of the actual spacecraft elements. Second, we have tried to pick models that can be easily constructed, so that our theoretical analysis can be checked experimentally. The models we have selected are described in the following paragraphs.

3.1 Detailed Description of the Acoustic Path Elements

As a model of the exterior acoustic field, element 1 in Fig. 3, we select a diffuse reverberant field of noise which can be described by a mean-square sound-pressure spectral density,[13] $S_p^{(1)}(f)$. The acoustic space containing this field has a volume V_1 and contains air with density ρ_o, speed of sound c_o, and zero mean velocity relative to the missile. The volume of the acoustic space will cancel out of the calculations and therefore is arbitrary for our theoretical analysis.

In an actual flight, we would expect that the noise impinging on the shroud would be more intense at axially grazing and near-grazing angles of incidence. Franken and Lyon[14] have studied the differences in the coupling between a diffuse noise field and the Titan missile skin, and between an axially weighted noise field and the missile skin. Their analysis showed less than 1 dB difference in the coupling loss factor for the two cases, except at the first few modes of the skin, where a 5 dB difference occurred. A similar analysis could be made for our model of the spacecraft shroud. In such an analysis, the coupling between each mode of the shroud and the sound field must be calculated separately.[15] Although a detailed analysis of this type is beyond the scope of this report, we have estimated the differences between the coupling of the shroud to a diffuse and a nondiffuse sound field. For most frequencies, the difference in the coupling loss factors for the two types of field is less than 1 dB. Near the ring frequency a difference of around 3 dB occurs. These differences in coupling loss factor, however, have less than 1 dB effect on the noise transmission through our model of the shroud. Since the diffuse reverberant field is easily simulated experimentally in a large room, it is a better model of the exciting noise field for our purposes than the axially weighted field.

In analyzing the acoustic response and transmission characteristics of the shroud, element 2, we model it by a ring-framed thin-walled cylindrical shell of radius a_2 and length ℓ_2. The ring frames are separated by distances ℓ_{2a}, ℓ_{2b}, ℓ_{2c}, etc. The structural properties of the shell wall are described, sufficiently for our analysis, by a longitudinal wavespeed $c_{\ell}^{(2)}$, a bending radius of gyration* κ_2, and a surface density $\rho_s^{(2)}$. We assume for our analysis that the compressional wavespeed is independent of frequency and that the radius of gyration is independent of the direction of bending.

The wall of the actual shroud may be inhomogeneous. In this case, the model described will be a valid representation for frequencies at which the free-bending wavelength is longer than the spacing between inhomogeneities. The actual shroud wall may also be nonisotropic. In such a case, two isotropic models can be used as limiting cases. The first model has a bending stiffness equal to the maximum bending stiffness of the nonisotropic wall, while the second has a stiffness equal to its minimum bending stiffness. If the maximum and minimum wall stiffnesses are less than a factor of two apart, the two limiting estimates will not differ greatly.

The structural properties of the ring frames and the shell end conditions are not critically important to our analysis. Only the over-all length of the frames must be known. The ends of the cylindrical shell model are taken to be closed by baffles that do not transmit acoustic energy and are structurally isolated from the shell.

---

* We mean here a bending radius of gyration that does not take into account the wall curvature, i.e., the bending stiffness in a flattened section of the shell wall.

An actual shroud is terminated on one end by a conical cap and on the other end by a structural bulkhead separating the spacecraft compartment from the interior of the launch vehicle. The acoustic acceptance and transmission properties of a conical structure are not completely understood. We assume that they can be represented sufficiently for our analysis by replacing the conical structure by a cylindrical extension to the shroud model with an area equal to that of the conical structure.

We further assume for our analysis that no vibratory energy is exchanged between the launch-vehicle structural members and the shroud-spacecraft assembly. For a particular case in which such energy exchange is important, the analysis of this report could be extended.

The interior of the shroud model is taken to be lined with a lightweight, acoustically absorptive material. The surface density and bending stiffness of this material are negligible as compared with those of the shell wall, so that the shell vibrational behavior is unaffected. We also take the thickness of the liner to be sufficiently thin so that radiative properties of the shell are not significantly changed. The effect of the liner on the absorption of the interior space has been included.

The interior acoustic space, element 3 in Fig. 3, has a very complicated geometry. It is sufficiently defined for our purposes by the speed of sound in the media c_o, the volume density ρ_o, the free volume V_3, and an absorption coefficient α_3. The absorption coefficient α_3 accounts for losses in the acoustic space and into the shroud acoustic liner. It does not account for losses due to transmission of acoustic energy through the shroud or in the spacecraft. We assume that the absorption coefficient of the interior acoustic space is small enough, $\alpha_3 < 0.3$, that the interior sound field is reverberant.

The liner in the actual OGO assembly is a 1/2- to 1-in.-thick, 3.5 lb/cu ft microquartz felt thermal blanket that covers approximately one-half of the surface area of the shroud. The acoustical properties of this material were not readily available for this project. However, we were able to obtain a small sample of the material and make an approximate experimental estimate of the absorption coefficient. This estimation is discussed in more detail in Section 3.4.6.

Finally, we model the spacecraft, element 4 of Fig. 3, by a rectangular open box of four flat panels. The box is sufficiently defined by its surface area A_4, and the length of its connected edges L_4. The panels are defined by a bending radius of gyration κ_4, and a surface mass density $\rho_s^{(4)}$.

The previous discussion concerning nonhomogeneous shell walls and the effect of ring frames and boundary conditions applies also to the spacecraft panels.

3.2 Division of Modes of Each Element into Groups of Similar Modes

The elements shown in Fig. 3 and described in the previous section are each lightly coupled to the neighboring elements and are lightly damped. Thus, to perform a statistical energy analysis in bands of frequencies, we group the modes within each element according to their coupling to modes in other elements and their resonance frequencies. An appropriate grouping for a particular frequency band is shown in Fig. 7. The modes of the shroud model are separated into four groups. First, modes that are both resonant within the band and spatially well-coupled to the acoustic field are grouped together.* Second, modes that are resonant but not well-coupled to the sound field are grouped together.** Third, modes that are spatially well-coupled but not resonant are grouped together. Finally, modes that are neither well-coupled nor resonant are grouped together.

The modes of the interior acoustic space are grouped into resonant and nonresonant modes. Finally, the modes of the spacecraft model are divided into AF and AS modes and nonresonant well-coupled and poorly coupled modes.

Certain groups of modes can be neglected in our analysis. Some modes in the cylindrical shell and the spacecraft are neither well-coupled nor resonant; these can be neglected, since their response and energy transmission will be negligible compared with that of the other modes. Nonresonant modes in the interior space can also be neglected, since their response is small and

---

* These modes are termed acoustically fast (AF), since their associated bending wavespeed is greater than the speed of sound in the acoustic space.

** These modes are termed acoustically slow (AS).

and they transmit negligible energy to the spacecraft compared with the resonant modes.* In addition, we have assumed that groups of modes in an element are uncoupled with other groups in the same element.**

The paths of energy flow that we consider are shown in Fig. 7. Note that we have neglected the power flow into the mechanical path. This neglect is valid provided that the dissipation loss factors of the ring frame and mounting trusses are not larger than that of the shroud. In the following Sections, we calculate the response of each element in bands of frequencies. Energy transmitted by resonant and nonresonant modes is considered separately.

3.3 Formulation of the Power-Balance Equations

The spectral response levels of the elements in the acoustic path can be found by using the statistical energy analysis described in Chapter 2. We first set up the power-balance equations for each group of modes selected in the previous section. These equations can be solved for the energy of each modal group in bands of frequencies. Then, to complete

---

* Note that we restrict our analysis to the frequency range in which resonant interior space modes exist.

** This may or may not be true. An experimental study is needed to support the hypothesis. The role of intermodal coupling in the same structure can be assessed theoretically by an additional calculation in which the modes are intimately coupled and equipart their total energy. For the OGO spacecraft assembly, the noise reduction increases approximately 5 dB below the ring frequency; this increase is due to intermodal energy sharing.

the analysis, we relate the space-average mean-square spectral acceleration or sound pressure response level of each element, $S_a^{(i)}(f)$ or $S_p^{(i)}(f)$, to these modal group energies.

When modes of the system reach steady-state energy levels, the net power flow in a band of frequencies into each group of modes must be zero. For example, a power balance in a band of frequencies on the acoustically fast (AF) group of shell modes gives

$$\Pi_{2AF,1} + \Pi_{2AF,3} + \Pi_{2AF}^{diss} = 0, \tag{18}$$

where $\Pi_{a,b}$ represents net power flow in the frequency band from modal group a to modal group b, and 1,2AF, 2AS, 2NR, 3, 4, and 4NR represent the modal groups. Using Eqs. (12) and (16), we can express the terms of Eq. (18), and of other similar equations, in terms of the modal densities, the loss factors, and the group time-average total energies. In this way, five linear algebraic equations are obtained. By power balance, we obtain for modal group 2AF

$$\omega\eta_{2AF,1}\,\bar{n}_{2AF}\left[\frac{E_{2AF}}{\bar{n}_{2AF}} - \frac{E_1}{\bar{n}_1}\right] + \omega\eta_{2AF,3}\,\bar{n}_{2AF}\left[\frac{E_{2AF}}{\bar{n}_{2AF}} - \frac{E_3}{\bar{n}_3}\right]$$

$$+ \omega\eta_{2AF}\,E_{2AF} = 0 \tag{19a}$$

For modal group 2AS, we obtain

$$\omega\eta_{2AS,1}\,\bar{n}_{2AS}\left[\frac{E_{2AS}}{\bar{n}_{2AS}}-\frac{E_1}{\bar{n}_1}\right]+\omega\eta_{2AS,3}\,\bar{n}_{2AS}\left[\frac{E_{2AS}}{\bar{n}_{2AS}}-\frac{E_3}{\bar{n}_3}\right]$$

$$+\,\omega\eta_{2AS}\,E_{2AS}=0 \qquad (19b)$$

Similarly, for modal group 3, we obtain

$$\omega\eta_{2AF,3}\,\bar{n}_{2AF}\left[\frac{E_{2AF}}{\bar{n}_{2AF}}-\frac{E_3}{\bar{n}_3}\right]+\omega\eta_{2AS,3}\,\bar{n}_{2AS}\left[\frac{E_{2AS}}{\bar{n}_{2AS}}-\frac{E_3}{\bar{n}_3}\right]$$

$$+\,\omega\eta_{4AF,3}\,\bar{n}_{4AF}\left[\frac{E_{4AF}}{\bar{n}_{4AF}}-\frac{E_3}{\bar{n}_3}\right]+\omega\eta_{4AS,3}\,\bar{n}_{4AS}\left[\frac{E_{4AS}}{\bar{n}_{4AS}}-\frac{E_3}{\bar{n}_3}\right]$$

$$-\,\omega\eta_3\,E_3+\Pi_{2NR,3}=0 \qquad (19c)$$

In Eq. (19c) we have included the power flow from nonresonant shell modes. In future calculations, this power flow will be set to zero to evaluate the transmission by resonant modes alone. Then, the power flow to resonant shell modes from the exterior field will be set to zero to evaluate the transmission by nonresonant modes alone.

$$\omega\eta_{4AF,3}\, n_{4AF} \left[\frac{E_{4AF}}{\bar{n}_{4AF}} - \frac{E_3}{\bar{n}_3} \right] + \omega\eta_{4AF}\, E_{4AF} = 0 \qquad (19d)$$

For modal group 4AS, we obtain

$$\omega\eta_{4AS,3}\, \bar{n}_{4AS} \left[\frac{E_{4AS}}{\bar{n}_{4AS}} - \frac{E_3}{\bar{n}_3} \right] + \omega\eta_{4AS}\, E_{4AS} = 0 \quad . \qquad (19e)$$

These five linear algebraic equations can be solved for the time-average total energies of each group, in bands of frequencies in terms of the time average total energy in group 1, which we take to be specified, and the modal densities and loss factors for each group. Solutions for the modal energies of each group will be presented in Sections 3.6 through 3.8. The loss factors and modal densities needed to evaluate these expressions are found in Section 3.4. Finally, the nonresonant response and transmission is found in Section 3.5.

The space-average mean-square spectral acceleration levels or sound-pressure levels of each element in the acoustic path can be found in terms of the time-average total energies of the modal groups representing the element. We calculate the resonant and nonresonant energies separately. The resonant time-average total energy in each element in a band of frequencies is simply the sum of the time-average total energies of each modal group within the element, i.e.,

$$E_2^{res.} = E_{2AS} + E_{2AF} \quad . \qquad (20)$$

Since the time-average kinetic and potential energy of a lightly damped multimodal system excited by broad-band noise are equal, the spectral acceleration levels of structural elements are given as

$$S_a^{(i)}(f) = \frac{\omega^2 E_2^{res}}{\rho_s^{(i)} A_i \Delta} , \tag{21}$$

where Δ is the frequency bandwidth being considered. The spectral sound-pressure levels are given by

$$S_p^{(i)}(f) = \frac{\rho_o c_o^2 E_i}{V_i \Delta} . \tag{22}$$

In summary, the group time-average total energies can be found from Eqs. (19) and then used to calculate the resonant response of each element in the acoustic path.

In the next two sections, the parameters needed to evaluate Eqs. (19) are found.

3.4 Calculation of the Modal Densities and Loss Factors

In this section, we obtain expressions for the modal densities and coupling loss factors needed to analyze resonant energy flow in the acoustic path. The expressions that are obtained give averages of these quantities for an ensemble of structures or acoustic spaces that have the same gross properties but differ in fine detail. Also, we estimate the dissipation loss factors, since a theoretical calculation is not possible and experimental evidence is not available.

3.4.1 Acoustic-Space Modal Density

The average modal density of an ensemble of acoustic spaces of volume V and speed of sound c_o is given in Refs. 16 and 17. In our notation, this expression is

$$n(f) = \frac{4\pi f^2 V}{c_o^3} \quad , \tag{23}$$

where n(f) is the ensemble average number of modes per unit frequency, f is the frequency in cycles per second, V is the acoustic-space volume, and c_o is the speed of sound. It follows that the average number of modes in a band of frequencies is given approximately by

$$N_{\text{in band } \Delta} \approx n(f)\Delta \quad , \tag{24}$$

where f is the center frequency of the band and Δ is the bandwidth. The variance of the number of modes in a frequency band from the mean value will depend on the magnitude of the mean. If the mean number of modes is high, the variance throughout the ensemble will be small. Thus, for sufficiently high frequencies or wide bandwidths, Eq. (24) will be an accurate estimation of the number of modes in a frequency band for any given acoustic space of volume V.

3.4.2 Flat Panel Modal Density

In our analysis of the acoustic path, we need the flat-panel AF and AS modal densities in bands of frequencies. These densities are particularly easy to find, since, by definition, all modes below the panel critical frequency are acoustically slow, while all modes above this frequency are acoustically fast. The panel critical frequency is defined as the frequency at which the free-bending wavelength in the panel is equal to the acoustic wavelength:

$$f_c = \frac{1}{2\pi} \frac{c_o^2}{\kappa c_\ell} \quad , \tag{25}$$

where f_c is the critical frequency, c_o is the acoustic speed of sound, κ is the panel-bending radius of gyration, and c_ℓ is the longitudinal wavespeed in the panel.

The average density of resonant modes in an ensemble of panels of area A, radius of gyration κ, and longitudinal wavespeed c_ℓ is given in reference 17 as

$$n(f) = \frac{A}{2\kappa c_\ell} \quad . \tag{26}$$

Thus, the density of AF and AS modes above the critical frequency can be given as

$$n_{AF}(f) = \frac{A}{2\kappa c_\ell} \quad ,$$

$$f > f_c \tag{27a}$$

and

$$n_{AS}(f) = 0 \quad .$$

The AF and AS modal density below the critical frequency is

$$\begin{aligned} n_{AF}(f) &= 0 \quad , \\ & \qquad\qquad\qquad f < f_c \qquad\qquad (27b) \\ n_{AS}(f) &= \frac{A}{2\kappa c_{\ell}} \quad . \end{aligned}$$

The average number of modes in a band of frequency for an ensemble of panels is given by $n(f)\Delta$. The variance from this average throughout the ensemble will decrease as the bandwidth increases. Our analysis is restricted to bands in which many modes resonate, so that the average number of modes will be a valid estimation for any of the panels within the ensemble.

3.4.3 Cylindrical Shell Modal Density

For analysis of the transmission of resonant acoustic energy through the shroud, we require the density of AF and AS shell modes in bands of frequencies. The approach that we follow is similar to that used in Refs. 18 and 19 to obtain the density of resonance frequencies in a cylindrical shell. We review the derivation of this density, and then extend the approach to find the density of AF modes. The density of AS modes follows as the difference between the densities of all resonant modes and AF modes.

The modal densities that will be obtained are average modal densities over an ensemble of cylindrical shells that differ only in details, such as boundary conditions.

Following the approach of Ref. 18, we find an expression for the resonance frequencies of a thin-walled simply supported cylindrical shell. This expression is given in Ref. 18 as

$$\nu^2 = (1-\mu^2)\,\frac{\sigma^4}{(\sigma^2+n^2)^2} + \beta^2[\sigma^2+n^2]^2$$

$$- \beta^2\,\frac{1}{2}\left[\frac{(4-\mu)n^2 - 2 - \mu}{1-\mu}\right] , \qquad (28)$$

where

$$\nu = \frac{f}{f_r} , \qquad f_r = \frac{c_\ell}{2\pi a} ,$$

$$\beta = \frac{h}{2\sqrt{3a}} , \ \sigma = \frac{m\pi a}{\ell} ,$$

ν is a dimensionless resonance frequency, f_r is the ring frequency, c_ℓ is the longitudinal wavespeed in the shell wall, a is the shell radius, μ is Poisson's ratio for the wall material, m is the axial mode number (m+1 equals the number of nodes in the axial direction), n is the circumferential mode number (one-half the number of nodes in the circumferential direction), ℓ is the length of the shell, and h is the shell-wall thickness. Eq. (28) is valid if $\sigma \gg \nu$. Since this condition is violated only for the lowest-order modes in very long cylinders, it is not judged to be a serious restriction. The first term of Eq. (28) results from membrane stresses in the cylinder, the second term results from bending stresses, and the third term is a correction that accounts for beam motions of the shell. In future calculations, we neglect this correction term, since it affects only a small number of modes in the complete groups that we consider. Also we neglect μ, since it is small as compared with unity.

It is useful for our calculations to rewrite Eq. (28) in two forms. First, we can write Eq. (28) in terms of wavenumbers (with the previously discussed simplifications) as

$$\nu^2 = \left(\frac{k_y}{k} \right)^4 + \beta^2 a^4 k^4 \ , \qquad (29)$$

where

$$k^2 = k_x{}^2 + k_y{}^2 \ ,$$

k is the wavenumber magnitude, k_x is the circumferential wavenumber, and k_y is the axial wavenumber.

Second, we write Eq. (29) in terms of dimensionless variables as

$$\nu^2 = \sin^4\theta + r^4 \ , \qquad (30)$$

where

$$r^2 = \beta \ a^2 k^2 \ ,$$

and

$$\sin\theta = \frac{k_y}{k} \quad .$$

From Eq. (29) or (30), lines of constant resonance frequency ν can be plotted in dimensionless wavenumber space as a function of $\sqrt{\beta}\, a\, k_x$ and $\sqrt{\beta}\, a\, k_y$ (see Fig. 8). Owing to the use of dimensionless variables, this plot is valid for all thin-walled cylindrical shells. In Fig. 8, the region in which the membrane effects--the first term of Eq. (29)--dominate is shown along with the region in which bending effects--the second term--dominate. The borderline between these two regions is given by the condition that the first and second terms of Eq. (28) or (29) are equal.

In a simply supported cylindrical shell, two modes with the same resonance frequency lie at intersections of lines of $k_y = m\pi/\ell$, where m is an integer, and $k_x = n/a$, n an integer. For other boundary conditions, the modes will shift from these positions by varying extents up to 1/2 unit in m and n. However, the average number of modes with resonance frequencies below a particular value of ν is given by the average density of modes in the dimensionless wavenumber space times the area under the line of constant resonance frequency corresponding to that value of ν.

If we assign to each pair of modes the rectangular area in the dimensionless wavenumber space extending half way to their nearest neighboring pair, then the density of a mode in dimensionless wavenumber space is twice* the reciprocal of this area

$$n(\sqrt{\beta}\ a\ k_x \quad , \quad \sqrt{\beta}\ a\ k_y) = \frac{2}{(\sqrt{\beta})(\sqrt{\beta}\ \pi a/\ell)} = \frac{2\ell}{\pi a\beta} \tag{31}$$

Thus, the total number of modes with dimensionless resonance frequencies below ν is given by

$$N(\nu) = \frac{2\ell}{\pi a\beta}\,\frac{1}{2}\int_0^{\theta_{max}(\nu)} r^2\, d\theta \quad , \tag{32}$$

where $N(\nu)$ is the average number of modes with resonance frequencies below ν, and $\theta_{max}(\nu)$ is the largest θ between zero and $\pi/2$ radians for which Eq. (30) can be solved for a real r:

$$\theta_{max}(\nu) = \arcsin\sqrt{\nu} \quad , \quad \text{for } \nu < 1,$$

$$\theta_{max}(\nu) = \pi/2 \quad \text{for } \nu > 1.$$

By substituting the value of r^2 from Eq. (30) into Eq. (32), we obtain the expression

$$N(\nu) = \frac{\ell}{\pi a\beta}\int_0^{\theta_{max}(\nu)} (\nu^2 - \sin^4\theta)^{1/2}\, d\theta. \tag{33}$$

---

*The factor of two arises because modes occur in pairs.

Eq. (33) was evaluated numerically. The results are presented graphically in Fig. 9, and can be compared with a more approximate expression obtained in Ref. 18.[20] The most significant difference between these results is that Eq. (29) is applicable at and near the ring frequency.

The ensemble average modal density is found from Eq. (33) by differentiation:

$$n(\nu) = \frac{\partial N}{\partial \nu} \quad , \tag{34}$$

where $n(\nu)$ is the average number of modes per unit ν. The indicated differentiation gives

$$n(\nu) = \frac{\ell}{\pi a \beta} \int_0^{\theta_{\max}(\nu)} \left[1 - \frac{\sin^4\theta}{\nu^2} \right]^{-1/2} d\theta . \tag{35}$$

This equation agrees with that obtained in Ref. 19.[20] Eq. (35) was evaluated numerically and is presented in Fig. 10.

The density of modes in even a small band of frequencies must be found by integration of the modal density, because of the singularity at the ring frequency, $\nu = 1$. For calculations in this report, we have calculated an average modal density over third-octave frequency bands. This density is defined as

$$\langle n(\nu)\rangle_{1/3 \text{ octave}} = \frac{N(\nu_2) - N(\nu_1)}{\nu_2 - \nu_1} \quad , \tag{36}$$

where $\langle \ \rangle_{1/3 \text{ octave}}$ represents an average over 1/3-octave bands, ν is the band center frequency, and ν_2 and ν_1 are the upper and lower limits of the band. The density predicted by Eq. (36) is plotted in Fig. 10, in dimensionless form.

At frequencies above the ring frequency, $\nu > 1$, the cylindrical-shell modal density becomes that of a flat plate with the same surface area.

An AF mode satisfies the condition that its associated bending wavespeed is greater than the speed of sound,

$$c_{b\ AF} \geq c_o \quad . \tag{37}$$

For the cylindrical shell, the wavespeed associated with a particular mode can be found in terms of the dimensionless variables introduced in Eq. (30).

$$c_b = \frac{\omega}{k} = c_\ell \frac{\sqrt{\beta}}{r} \left(\sin^4\theta + r^4\right)^{1/2} \quad . \tag{38}$$

Thus, the condition for an AF mode is

$$\frac{\beta}{r_{AF}^{\ 2}}\left(\sin^4\theta_{AF} + r_{AF}^{\ 4}\right) \geq \frac{c_o^{\ 2}}{c_\ell^{\ 2}} \quad , \tag{39}$$

where r_{AF} and θ_{AF} are the coordinates of an AF mode in dimensionless k-space. The solution of Eq. (39) for r_{AF} is

$$r_{AF}^2 \gtrless \frac{1}{2\beta}\frac{c_o^2}{c_\ell^2} \pm \left[\frac{1}{4\beta^2}\frac{c_o^4}{c_\ell^2} - \sin^4\theta_{AF} \right]^{1/2} , \qquad (40)$$

where ">" applied to the "+" solution and "<" applies to the "-" solution. If we define ν_c as the ratio of the critical frequency to the ring frequency,

$$\nu_c \equiv \frac{f_c}{f_r} = \frac{1}{\beta}\frac{c_o^2}{c_\ell^2} , \qquad (41)$$

then Eq. (40) can be written as

$$r_{AF}^2 \gtrless \frac{\nu_c}{2} \pm \frac{\nu_c}{2}\left[1 - \frac{4\sin^4\theta_{AF}}{\nu_c^2} \right]^{1/2} . \qquad (42)$$

The "+" solution of Eq. (42) corresponds to AF modes with resonance frequencies near and above the critical frequency. These modes would also be acoustically fast in the flat panel. The "-" solution, however, corresponds to AF modes with resonance frequencies near and below the ring frequency. For thin-walled cylindrical shells, where β<<1, the ring frequency will lie well below the critical frequency, so that AF modes occur below the critical frequency. AF modes do not occur below the critical frequency in flat panels. Therefore, the response, below the critical frequency, of a flat panel can be significantly less than that of a cylindrical shell of equal area.[21,22] The region of AF modes near the ring frequency, for a value of $\nu_c = 8$, which is appropriate for the OGO shroud model, is indicated in Fig. 8. This region is well within the membrane-controlled region and indicates that the increased stiffness due to curvature is responsible for the occurrence of AF modes in this region.

When ν_c is large, Eq. (42) takes on a simple form,

$$r_{AF}^2 > \nu_c \quad ,$$

and

$$\nu_c \gg 1$$

$$r_{AF}^2 < \frac{\sin^4\theta_{AF}}{\nu_c} \quad . \tag{43}$$

We now follow the same procedure as was used to find the density of resonant modes of the cylindrical shell. The expression $N_{AF}(\nu)$ is the average total number of AF modes with resonance frequencies below ν, for an ensemble of cylindrical shells. $N_{AF}(\nu)$ is given by the average density of modes in the dimensionless wavenumber space times the area of the AF mode region below the line of constant resonance frequency ν. When $\nu_c \gg 1$, the lines of constant resonance frequency in the AF mode region are given by

$$\theta = \arcsin\sqrt{\nu}. \tag{44}$$

Thus, the number of AF modes with resonance frequencies below ν is

$$N_{AF}(\nu) = \frac{2\ell}{\pi a\beta}\int_0^{\theta_{max}} \frac{1}{2}\,\frac{\sin^4\theta}{\nu_c}\,d\theta , \tag{45}$$

where θ_{max} equals the smaller of $\arcsin\sqrt{\nu}$ and $\pi/2$. Eq. (45) can be evaluated to give

$$N_{AF}(\nu) = \frac{\ell}{8\pi a\beta\nu_c}\left[3\sin^{-1}\sqrt{\nu} - 5(\nu-\nu^2)^{1/2} + 2\sqrt{\nu}(1-\nu)^{3/2}\right],$$

$$\text{if } \nu < 1, \tag{46}$$

and

$$N_{AF}(\nu) = \frac{3\ell}{16a\beta\nu_c} , \quad \text{if } \nu > 1.$$

A modal density can be obtained by differentiation of this equation:

$$n_{AF}(\nu) = \frac{\partial N_{AF}}{\partial\nu} \tag{47}$$

For the purposes of the analysis in this report, however, it is more convenient to obtain the average modal density in third-octave bands, defined by

$$\langle n_{AF}(\nu)\rangle_{1/3 \text{ octave band}} = \frac{N_{AF}(\nu_1)-N_{AF}(\nu_2)}{\nu_1 - \nu_2} , \tag{48}$$

where ν is the center frequency of the band, and ν_1 and ν_2 are the upper and lower frequency limits of the band. The 1/3-octave average AF modal density is plotted in dimensionless form in Fig. 11. Expression (49)gives the average number of AF modes for an ensemble of similar cylindrical shells:

$$\langle n_{AF}(\nu)\rangle_{1/3 \text{ octave}} \Delta\nu, \tag{49}$$

where $\Delta\nu$ is a third-octave bandwidth in units of dimensionless frequency. As previously described, if this quantity is sufficiently large, it will be an accurate estimate for the number of modes occurring in a third-octave band for any member of the ensemble.

The density of AS modes is found as the difference between the density of all resonant modes and AF modes. The density of all resonant modes is plotted in Fig. 11 and can be compared with the AF modal density to obtain the AS modal density.

For future calculations, we need the cylindrical-shell modal densities as a function of frequency. These are given by

$$\langle n(f)\rangle_{1/3\ \text{octave}} = \langle n(\nu)\rangle_{1/3\ \text{octave}} \frac{2\pi a}{c_\ell} \qquad (50)$$

We need also the modal densities of shell segments separated by ribs. Since the modal density of two connected structures is the sum of the modal densities for each individual structure, the modal density of a ribbed shell is simply the sum of the densities of each segment. For our model of the OGO shroud, each segment is the same except for axial length. Therefore, the modal density of the shroud model can be found in terms of the total length of the shell.

3.4.4 The AF Mode-Acoustic-Space Coupling Loss Factor

For our analysis, we need the coupling loss factors between an AF mode and an acoustic space for both a cylindrical shell and a flat panel. As discussed in Section 2.4, our approach is to calculate the coupling loss factor between an AF mode and an infinite acoustic space. We hypothesize that this coupling loss factor is the average coupling loss factor between the AF mode and an ensemble of acoustic spaces with the same volume but different geometries.

If we restrict our analysis to frequencies at which the acoustic wavelength is shorter than the structural dimensions, the coupling loss factor for AF modes in the cylindrical shell and in the flat panel will be similar. Therefore, we can use the coupling loss factor between a flat-panel AF mode and an acoustic space.

The coupling loss factor can be expressed in terms of the radiation resistance or the radiation efficiency as

$$\eta \equiv \frac{R_{rad}}{\omega \rho_s A} \equiv \frac{\rho_o c_o}{\omega \rho_s} \sigma_{rad} \quad , \tag{51}$$

where R_{rad} is the radiation resistance and σ_{rad} is the radiation efficiency. The radiation resistance of an AF mode in a flat panel in an infinite baffle has been calculated in Ref. 23 as

$$R_{rad}^{AF} = \rho_o c_o A \left[1 - \left(\frac{k}{k_o} \right)^2 \right]^{-1/2} , \; k < k_o \; , \tag{52}$$

where k_o is the acoustic wavenumber and k is the modal wavenumber. This expression does not apply at $k = k_o$, where other effects cause the radiation resistance to remain finite. From Eq. (52), we see that all AF modes do not have the same coupling to the acoustic field. This is contrary to our original hypothesis in setting up the modal groupings. We assume that all AF modes have a radiation resistance equal to $\rho_o c_o A$.

$$R_{rad}^{AF} \approx \rho_o c_o A \quad , \tag{53}$$

or

$$\sigma_{rad}^{AF} \approx 1 \quad .$$

Since only a few modes, whose wavenumbers are very close to the acoustic wavenumber, do not agree with this approximation, it is judged to be valid for our analysis. The average coupling loss factor for the AF modal group is given by*

$$\eta_{AF,acoust} = \frac{\rho_o c_o}{\omega \rho_s} \quad . \tag{54}$$

In deriving Eq. (54), we have neglected the effect of structure geometry on the coupling loss factor by assuming that the acoustic wavelength was shorter than the dimensions of the cylinder. For our model of the OGO shroud, the region of frequency where this assumption is valid lies above 200 cps. Below this frequency, the coupling loss factor will lie somewhat below that predicted by Eq. (54).

For the flat panel, Eq. (54) is applicable only above 300 cps; below 300 cps, the acoustic wavelength is longer than the panel dimensions, so that the two sides of the panel become acoustically short-circuited. We do not encounter this problem, however, because no AF modes below 500 cps occur in the spacecraft panels.

3.4.5 The AS Mode-Acoustic-Space Coupling Loss Factor

We assume, as in the previous section, that the acoustic wavelength is shorter than the cylindrical shell radius;

---

* When the baffle is not infinite and the panel can radiate from both sides into the acoustic space, the radiation resistance is $2\rho_o c_o A$, provided the baffle dimensions are greater than the acoustic wavelength.

therefore the coupling loss factor for a flat-panel AS mode in an infinite baffle can be used with only minor corrections for our analysis. The radiation properties of a flat, infinitely baffled panel have been the subject of many papers.[15,23] It has been found that an AS mode radiates power into the far field from its edges or corners, or, in general, from any region surrounding a discontinuity such as a rib or ring frame. It follows that the baffle at the edge of the panel can have a significant effect on the radiation by an AS mode. If the edge is unbaffled, the two sides of the panel are acoustically short-circuited near the edge, so that negligible power is radiated from this region. Also, if the panel is baffled so that it radiates into 3/4- or 1/4-space* rather than 1/2-space, the power radiated from the panel edges is reduced or increased proportionately.

The average radiation resistance of an AS mode in an unribbed infinitely baffled panel in which the panel dimensions are greater than an acoustic wavelength is given in Ref. 23 as

$$R_{rad}^{AS} = \rho_o c_o P_r \lambda_c \, g_2(f/f_c) + \rho_o c_o \lambda_o \lambda_c \, g_1(f/f_c) \quad ,$$

$$\left[1/2 \; k_o \ell_x , \; 1/2 \; k_o \ell_y > 1 \right] , \qquad (55)$$

where P_r is the radiating perimeter, λ_c is the acoustic wavelength at the critical frequency f_c, λ_o is the acoustic wavelength at the frequency under consideration, k_o is the acoustic wavenumber, ℓ_x and ℓ_y are the panel dimensions, and g_2 and g_1 are functions

---

* 3/4-space allows radiation from an edge at angles from grazing to 270°.

given in Ref. 23. Usually, the second term of this equation will be negligible compared to the first. When the panel dimensions are shorter than an acoustic wavelength, the AS mode average radiation resistance is given by

$$R_{rad}^{AS} = \rho_o c_o A_p (4/\pi^4)(P_r \lambda_c / A_p)(f/f_c)^{1/2} \quad ,$$

$$\left[\, 1/2\ k_o \ell_x,\ 1/2\ k_o \ell_y < 1 \,\right] \quad . \qquad (56)$$

For a ribbed panel we assume that the structural bending-wave-length is less than the spacing between ribs and that the vibration fields on the two sides of the ribs are uncorrelated. Then the panel will radiate from its edges and from both sides along the ribs. The radiating perimeter is twice the length of interior ribs plus the length of the baffled panel edges. Unbaffled panel edges are acoustically short-circuited and therefore do not contribute to the radiating perimeter. For the ribbed panel, ℓ_x and ℓ_y in Eqs. (55) and (56) are the rib spacings.

Eqs. (55) and (56) are valid also for a cylindrical shell at frequencies above the ring frequency. This is because the curvature effects are unimportant for these frequencies and the vibrational behavior is that of a flat panel.[22]

The modes within the AS group have varied radiation resistances, contrary to our assumption in setting up the groups. A more detailed division would consider AS-edge and AS-corner modes separately.[24] The errors that result from using one AS mode group rather than two are not great.

3.4.6 Estimation of Dissipation Loss Factors

In spite of recent advances toward an understanding of damping mechanisms in structures, the dissipation loss factors cannot be predicted theoretically at this time. Therefore, when possible, structural dissipation loss factors should be determined by experiments on the spacecraft assembly, so that the theoretical analysis can be based on an accurate estimation of this parameter. Appropriate experimental techniques for determining the dissipation loss factor are described in Appendix A.

Since we do not have experimental results on which to estimate the dissipation loss factors for the OGO shroud and spacecraft panels, we must make an empirical estimate of this parameter based on past experimental and field studies of structures. In our calculations, we estimate the structural dissipation loss factors to be

$$\eta_{\text{structure}} = 10^{-2} \quad . \tag{57}$$

For certain calculations, a value of 3×10^{-2} will also be used to show the role that this parameter plays in the response predictions.

The acoustic-space loss factor is largely controlled by the liner within the shroud. Therefore, if the acoustic absorption properties of this liner are known,[26] the acoustic-space loss factor can be estimated with confidence. Liners used in most spacecraft assemblies are selected for their thermal insulation properties, so that data concerning their acoustic properties is not readily available. Therefore, for our theoretical study, we make an approximate estimate of the expected absorption coefficient for a typical spacecraft assembly:

$$\bar{\alpha}_3 = 0.1 \quad . \tag{58}$$

In some calculations, a value of $\bar{\alpha}_3 = 0.3$ is used to show the role that interior space absorption plays in determining the response levels of the spacecraft.

The actual OGO shroud liner is a microquartz felt blanket. To support the above estimation, we measured the absorption coefficient of this material experimentally for normally incident sound waves using an impedance tube. The results of this experiment indicated absorption coefficients from 0.05, at low frequencies (~400 cps), to 0.7, at high frequencies (~8000 cps). Since approximately one-half of the shroud surface is lined, these absorption coefficient values give average absorption coefficients of 0.025 to 0.35. The impedance tube experiment must be looked upon only as an approximate means to estimate the absorption coefficient in the spacecraft assembly, since only normally incident sound waves are used and the liner backing is rigid. A more appropriate method of estimating the interior space absorption coefficient is described in Appendix A.

The dissipation loss factor is related to the average absorption coefficient by

$$\eta_3 = \frac{c_o A_2}{4\omega V_3} \bar{\alpha}_3 \quad , \tag{59}$$

where A_2 is the surface area of the shroud model.

3.5 Formulation of the Response and Transmission by Nonresonant Modes

The response of a curved or flat flexible panel to a sound field, when the panel dimensions exceed both the acoustic and structural wavelengths, may be thought of as composed of two types of motion. First, the sound pressure will induce a panel motion that matches the pressure field in both frequency and wavelength. This response is often referred to as the "forced-wave" or "forced" response. When the induced wavelength exceeds the free flexural wavelength, the modal responses that make up the forced-wave response are nonresonant and are controlled by the modal mass.

At the boundaries of the panel, the forced wave alone will not satisfy the boundary conditions. In order to do so, bending motions, which are solutions of the homogeneous wave equation, are generated, and these combine with the forced waves to satisfy the boundary conditions. These additional motions are commonly referred to as "free-wave" or "free" response. On a modal basis, the free response is described by resonant modes. We found in the previous section that the resonant response and transmission are best handled on a modal basis. For the nonresonant response, however, it is more convenient to think in terms of forced and free-wave response.

The forced response, since it does not depend on the existence of boundaries, will be the same for the infinite panel as for the finite panel. Our approach is to calculate the forced response and transmission in terms of the infinite-panel impedances. This approach is well-known in architectural acoustics.[8]

The pressure on an infinite panel resulting from a sound wave incident from an angle ϕ, measured from the normal, can be separated into a blocked pressure and a radiation pressure component. The blocked pressure is that pressure that would exist on the panel if it were not allowed to move. The frequency and wavelength of the blocked pressure will be the frequency and trace wavelength of the incident sound wave. The pressure amplitude will be twice that of the incident wave because of the interaction of the incident and reflected waves.* The radiated pressure will be caused by sound waves radiated from each side of the panel, owing to its motion. The frequency and trace wavelength of the radiated sound waves will be the same as those of the panel vibrations, which in turn are the same as those of the incident sound wave. It follows that the radiated sound wave is a plane wave traveling at an angle ϕ from the normal. The radiation pressure opposes the blocked pressure and acts on both sides of the panel with an amplitude equal to that of the radiated plane wave. Therefore, the net pressure difference on the surface of the panel is

$$p(x,t,\phi) = 2\mathrm{Re}\{[P_{inc} - P_{rad}]\, e^{i(k_o \sin\phi\, x - \omega t)}\} , \qquad (60)$$

where $p(x,t,\phi)$ is the net pressure acting on the panel, x is a distance along the panel surface, Re signifies "real part of," P_{inc} is the complex pressure amplitude of the incident

---

* If the radius of curvature of a curved panel is not large as compared with an acoustic wavelength, the incident wave is diffracted by the surface and a description of the blocked pressure acting on the panel is more complicated (Ref. 25).

plane wave, ϕ is the angle of incidence, P_{rad} is the complex pressure amplitude of the radiated plane waves, k_o is the acoustic wavelength, and ω is the frequency of the excitation. The complex velocity amplitude in the infinite panel is related to the complex pressure amplitude on its surface by the panel impedance:

$$V_{panel} = \frac{2[P_{inc} - P_{rad}]}{Z_{panel}} \quad , \qquad (61)$$

where Z_{panel} is the panel impedance. Similarly, the radiated complex pressure amplitude is related to the complex velocity amplitude in the panel by

$$P_{rad} = Z_{rad} V_{panel} \quad , \qquad (62)$$

where Z_{rad} is the acoustic radiation impedance.

We can combine the above equations to find either the response or the transmission of an infinite panel excited by a plane wave. The complex response amplitude is given by

$$\frac{V_{panel}}{P_{inc}} = \frac{2}{Z_{panel} + 2\, Z_{rad}} \quad , \qquad (63)$$

while the complex transmitted-wave amplitude is given by

$$\frac{P_{trans}}{P_{inc}} = \frac{2\, Z_{rad}}{Z_{panel} + 2\, Z_{rad}} \quad . \qquad (64)$$

Since we are considering the region in which the trace wavelength of the exciting plane wave exceeds the free-bending-wave length, the infinite panel impedance is purely reactive:

$$Z_{\text{panel}} = i\omega\rho_s \quad , \tag{65}$$

where ρ_s is the surface mass density. The radiation impedance also takes on a simple form, since the panel vibrations match spatially with a plane sound wave radiated at an angle ϕ. The velocity of the radiated plane wave normal to the panel must match the velocity of the panel. Thus, the acoustic radiation impedance is

$$Z_{\text{radiation}} = \frac{\rho_o\, c_o}{\cos\, \phi} \quad , \tag{66}$$

where $\rho_o c_o$ is the acoustic impedance, and ϕ is the angle in which the wave is radiated (also the angle of incidence of the incoming acoustic plane wave).

Using these impedances, the complex forced response amplitude to an incident plane wave is

$$\frac{V_{\text{panel}}}{P_{\text{inc}}} = \frac{2}{i\omega\rho_s + 2\,\rho_o c_o/\cos\phi} \quad , \tag{67}$$

while the complex amplitude of the transmitted wave is

$$\frac{P_{trans}}{P_{inc}} = \frac{2\rho_o c_o/\cos\phi}{i\omega\rho_s + 2\rho_o c_o/\cos\phi} \quad . \tag{68}$$

When the panel excitation is a diffuse field of noise, the spectral response and the power transmission due to forced wave motion is found by averaging the mean-square response or power transmission over all solid angles of the incident wave. The mean-square response velocity spectrum is given by*

$$\frac{S_v(f)}{S_p(f)} = \frac{\int_0^{\pi/2} \left|\frac{V}{P_{in}}\right|^2 \sin\phi \, d\phi}{2\int_0^{\pi/2} \sin\phi \, d\phi} \quad , \tag{69}$$

where $S_v(f)$ is the mean-square forced response velocity spectrum, $S_p(f)$ is the mean-square sound pressure spectrum in the diffuse field, and $|V/P_{in}|$ is the magnitude of the complex amplitude ratio given by Eq. (67). Equation (69) can be evaluated to give

$$\frac{S_v(f)}{S_p(f)} = \frac{2}{\omega^2 \rho_s{}^2} \left[1 - \frac{2\rho_o c_o}{\omega \rho_s} \tan^{-1} \left(\frac{\omega \rho_s}{2\rho_o c_o}\right) \right] \tag{70}$$

---

* The factor of two arises because the sound field exists only on one side of the panel.

The second term of this equation is important only for very light panels. The spectral velocity predicted by Eq. (70) is referred to as random-incidence mass-law response.

The acoustic power transmitted by a unit area of the panel, Π_{trans}, is also found by summing over all directions of incidence

$$\Pi_{trans} = \pi \int_0^{\pi/2} V_{panel} \, P^*_{trans} \, \sin\phi \, d\phi \quad , \tag{71}$$

where P^*_{trans} is the complex conjugate of P_{trans}, while the acoustic power incident on this panel per unit area, Π_{inc}, is given by

$$\Pi_{inc} = \frac{\pi}{\rho_o c_o} \int_0^{\pi/2} \left| P_{inc} \right|^2 \cos\phi \, \sin\phi \, d\phi \quad . \tag{72}$$

The ratio of the power transmitted to the power incident is referred to as a sound transmission coefficient τ. For diffuse field excitation, the sound transmission coefficient is found from Eqs. (67), (68), (71), and (72):

$$\bar{\tau} = \frac{\Pi_{trans}}{\Pi_{inc.}} = \frac{4\rho_o^{\,2} c_o^{\,2}}{\omega^2 \rho_s^{\,2}} \ln\left(1 + \frac{\omega^2 \rho_s^{\,2}}{4\rho_o^{\,2} c_o^{\,2}}\right), \tag{73}$$

where $\overline{\tau}$ is the random incidence mass-law sound transmission coefficient. It is also common practice to define a transmission loss (TL). This parameter is given by

$$TL = 10 \log_{10} \left(\frac{1}{\overline{\tau}} \right) \quad . \tag{74}$$

The random-incidence mass-law transmission loss predicted by Eqs. (73) and (74) agrees with that plotted in Fig. 13.7 of Ref. 8.

Equations (70) and (73) give the response and power transmission of an infinite panel when the wavelength of the exciting pressure field is much longer than the free-bending-wave length in the panel. These equations can also be used to predict the forced-wave response and power transmission of a finite panel, when the panel dimensions are long in comparison with the exciting pressure wavelength. The region of application for most panels is the frequency range above the first few resonances of the panel and below the critical frequency, at which the acoustic wavelength is equal to the free-bending-wave length. In the following sections our applications of the formulas are restricted to this region of frequency.

3.6 Acoustic Noise Reduction by the Shroud

In Section 3.3, a set of algebraic equations was developed by power balance on the modal groups in the acoustic path. This set of equations can be solved for the vibration or sound-pressure spectrum of each element in the acoustic path, in terms of the exterior sound-pressure spectrum and the structural and acoustic properties of the element.

In the present section, we consider a preliminary step toward the prediction of the spacecraft vibration spectrum: namely, the prediction of the noise reduction by the cylindrical-shell model of the shroud. The noise reduction (NR) is defined as the difference in sound-pressure levels (expressed in decibels) outside and inside the shell.

The noise reduction by the shell can be conveniently studied in three regions of frequency[27]: low frequencies, below the first resonant frequencies of the shell and the interior acoustic space; intermediate frequencies, at which either the shell or the interior space vibrates resonantly; and high frequencies, at which both elements vibrate resonantly. We restrict our attention in this report to high frequencies.

In the calculations that follow, noise transmitted by resonant and nonresonant shell motions are considered separately. The over-all noise transmission will be a superposition of the two contributions.

In Section 3.6.3, the noise reduction by the OGO shroud model is calculated as an example illustrative of the more-general predictions developed in Sections 3.6.1 and 3.6.2.

3.6.1 Noise Reduction by Resonant Motion of the Shroud

The noise reduction by resonant motion in the cylindrical-shell model of the shroud can be found from the power-balance equations, Eqs. (19), with the power flow from nonresonant modes, $\Pi_{2NR,3}$, equal to zero. As a preliminary step, however, we note that the coupling loss factor between cylindrical-shell modes and the exterior sound field is approximately equal to that between shell modes and the interior field. The only difference is due to the baffling at the ends of the shell. The AS modes radiate from the ends of the cylindrical shell into 3/4-space for the external field and 1/4-space for the internal field. Because of the shell ribs, however, the radiating perimeter is much longer than the edges at the ends of the cylinder. Therefore, the difference in baffling will produce only a small difference in the over-all AS mode coupling loss factor to the interior and exterior spaces.

Assuming that the coupling loss factors between the shell modes and the two acoustic spaces are equal, we first solve Eqs. (19) for the ratio of exterior to interior acoustic-space time-average total energies:

$$\frac{E_1}{E_3} = \frac{n_1}{n_3}\left[\frac{\eta_{2AS1}\, n_{2AS} + \eta_{2AF1}\, n_{2AF} + \eta_3^{eq.}\, n_3}{\dfrac{\eta_{2AS1}^2\, n_{2AS}}{2\eta_{2AS1} + \eta_{2AS}} + \dfrac{\eta_{2AF1}^2\, n_{2AF}}{2\eta_{2AF1} + \eta_{2AF}}} - 1\right] , \quad (75)$$

where $\eta_3^{eq.}$ is a composite loss factor accounting for losses in the acoustic space and in the spacecraft panels, and

$$\eta_3^{eq.} = \eta_3 + \frac{n_{4AF}}{n_3}\,\frac{\eta_{4AF}\,\eta_{4AF3}}{\eta_{4AF3} + \eta_{4AF}} + \frac{n_{4AS}}{n_3}\,\frac{\eta_{4AS}\,\eta_{4AS3}}{\eta_{4AS3} + \eta_{4AS}} . \quad (76)$$

The mean-square sound-pressure spectra can be expressed in terms of these group energies through Eq. (22):

$$\frac{S_p^{(1)}(f)}{S_p^{(3)}(f)} = \frac{E_1}{V_1}\;\frac{V_3}{E_3} \quad . \tag{77}$$

A further step toward prediction of the noise reduction is taken by relating the modal densities n_1 and n_3 in Eq. (75) to the volumes V_1 and V_3 through Eq. (23):

$$\frac{n_1}{n_3} = \frac{V_1}{V_3} \quad . \tag{78}$$

It follows now that the ratio of the exterior to interior sound-pressure spectra due to noise transmission by resonant shell modes is given by the bracketed expression in Eq. (75).

$$\frac{S_p^{(1)}(f)}{S_p^{(3)}(f)} = \left[\frac{\eta_{2AS1}\, n_{2AS} + \eta_{2AF1}\, n_{2AF} + \eta_3^{eq.} n_3}{\dfrac{\eta_{2AS1}^2\, n_{2AS}}{2\eta_{2AS1} + \eta_{2AS}} + \dfrac{\eta_{2AF1}^2\, n_{2AF}}{2\eta_{2AF1} + \eta_{2AF}}} - 1 \right] \quad . \tag{79}$$

The noise reduction follows, by definition, as

$$NR^{(res)} = 10 \log_{10} \left[\frac{S_p^{(1)}(f)}{S_p^{(3)}(f)} \right] \quad , \tag{80}$$

where $NR^{(res)}$ indicates noise reduction by resonant shell modes. The parameters needed to evaluate this noise reduction have been calculated or estimated in Section 3.4. It was found in that section that the modal density of AF shell modes is zero for frequencies between the ring frequency and the critical frequency. Therefore, the noise reduction can be simplified in this frequency range:

$$NR^{(res)} = 10 \log_{10} \left\{ 1 + \frac{\eta_{2AS}}{\eta_{2AS,1}} + \left[2 + \frac{\eta_{2AS}}{\eta_{2AS,1}} \right] \left[\frac{n_3}{n_{2AS}} \frac{\eta_3^{eq.}}{\eta_{2AS,1}} \right] \right\} ,$$

$$f_r < f < f_c \quad . \qquad (81)$$

Similarly, above the critical frequency, no AS modes occur, so that $NR^{(res)}$ can be written as

$$NR^{(res)} = 10 \log_{10} \left\{ 1 + \frac{\eta_{2AF}}{\eta_{2AF,1}} + \left[2 + \frac{\eta_{2AF}}{\eta_{2AF,1}} \right] \left[\frac{n_3}{n_{2AF}} \frac{\eta_3^{eq.}}{\eta_{2AF,1}} \right] \right\} ,$$

$$f > f_c \quad . \qquad (82)$$

For frequencies below the ring frequency, Eq. (79) cannot generally be simplified. However, we can make an approximation that is appropriate for most spacecraft assemblies. We assume that the AF modes below the ring frequency dominate the acoustic acceptance and radiation properties of the shell, i.e., that

$$n_{2AF} \, \eta_{2AF,1} \gg n_{2AS} \, \eta_{2AS,1}.$$

With this assumption, the noise reduction becomes approximately

$$NR^{(res)} \approx 10 \log_{10} \left\{ 1 + \frac{\eta_{2AF}}{\eta_{2AF,1}} + \left[2 + \frac{\eta_{2AF}}{\eta_{2AF,1}} \right] \left[\frac{n_3}{n_{2AF}} \frac{\eta_3^{eq.}}{\eta_{2AF,1}} \right] \right\} ,$$

$$f_{min} < f < f_R, \qquad (83)$$

where f_{min} is the lowest band center frequency for which a sufficient number of AF modes occur in the test band to make the ensemble average loss factors and modal densities accurate estimates for each member of the ensemble.

The above equations can be used to calculate the noise reduction by resonant modes in the OGO shroud model. First, however, we continue our general formulation by predicting the noise reduction by nonresonant motion of the shell.

3.6.2 Noise Reduction by Nonresonant Modes in the Shroud Model

The noise reduction by nonresonant modes can also be found from the power-balance equations, Eqs. (19), and the results of Section 3.5. Since we have considered noise transmission by resonant modes separately, we set the power input to the resonant modes from the exterior acoustic space equal to zero. This is done by setting E_1 equal to zero in Eqs. (19a) and (19b). In addition, we restrict our consideration to frequencies between the ring frequency and the critical frequency, since it is only in this region that the standard mass-law prediction of the noise transmission is valid. Since we restrict our analysis to this frequency range, we can set the density of AF modes equal to zero in the power balance equations. Equations (19) can now be solved for the total energy E_3:

$$\Pi_{2NR,3} = \left[\frac{n_{2AS}}{n_3} \eta_{2AS1} \left(\frac{\eta_{2AS1} + \eta_{2AS}}{2\eta_{2AS1} + \eta_{2AS}} \right) + \eta_3^{eq.} \right] \omega E_3 \ , \quad (84)$$

where $\eta_3^{eq.}$ is given by Eq. (76) and η_{2AS3} is assumed to be equal to η_{2AS1}. Equation (84) expresses a power balance between net power into the interior space modes from the nonresonant modes and net power lost by AS mode dissipation resulting from radiation to the exterior space and dissipation into the interior space and the spacecraft panels.

The net power transmitted to the interior acoustic space by nonresonant modes, $\Pi_{2NR,3}$ can be expressed in terms of the sound transmission coefficient $\overline{\tau}$, given by Eq. (73):

$$\Pi_{2NR,3} = \overline{\tau} \ \Pi_{inc} \quad , \qquad (85)$$

where Π_{inc} is the net acoustic power incident on the shroud and is given by

$$\Pi_{inc} = \frac{A_2 \Delta}{4\rho_o c_o} \left[S_p^{(1)}(f) - S_p^{(3)}(f) \right] . \qquad (86)$$

The group time-average total energy E_3 can be expressed in terms of the spectral sound pressure by Eq. (22):

$$S_p^{(3)}(f) = \frac{2\rho_o c_o^2}{V_3 \ \Delta} \ E_3 \quad , \tag{22}$$

Finally, Eq. (84) can be solved for the ratio of external to internal sound-pressure spectra and the resultant noise reduction by nonresonant modes:

$$NR^{(\text{nonres})} = 10 \log_{10} \left\{ 1 + \frac{4\omega V_3}{\bar{\tau} A_2 c_o} \left[\frac{n_{2AS}}{n_3} \eta_{2AS1} \left(\frac{\eta_{2AS1} + \eta_{2AS}}{2\eta_{2AS1} + \eta_{2AS}} \right) + \eta_3^{\text{eq.}} \right] \right\}. \tag{87}$$

For most spacecraft assemblies, the bracketed term [ ] can be adequately approximated by η_3. In this case, the noise reduction can be expressed approximately by

$$NR^{(\text{nonres})} = 10 \log_{10} \left\{ 1 + \frac{4\omega V_3}{A_2 c_o} \ \frac{\eta_3}{\bar{\tau}} \right\} \quad . \tag{88}$$

For the sake of convenience in future sections, we express the nonresonant noise reduction in terms of an absorption coefficient $\bar{\alpha}_3$. This coefficient is related to the loss factor η_3 by Eq. (59) so that Eq. (88) can be written as

$$NR^{(\text{nonres})} = 10 \log_{10} \left\{ 1 + \frac{\bar{\alpha}_3}{\bar{\tau}} \right\} \quad . \tag{89}$$

3.6.3 Noise Reduction by a Model of the OGO Shroud

In this section, we calculate the noise reduction by a model of the OGO shroud. These calculations serve as an illustrative example of the general formulation of noise reduction by a spacecraft shroud.

An appropriate model of the OGO is shown in Fig. 1 and is described in greater detail in Section 3.1. Parameter values describing this model are given in Table I. The dissipation loss factors of the actual structural elements in the OGO assembly are not known. Furthermore, they cannot be estimated with confidence theoretically. Thus, we were forced to make a rough estimate of these loss factors based on past experimental studies of similar structures. Because of the uncertainty in these estimates, the predicted noise reduction for the OGO shroud may not agree with that found experimentally. Support of the theoretical predictions in this report must come from experimental studies in which both the noise reduction and the dissipation loss factors are found.

Even though the predictions in this section may not be accurate for the OGO shroud, they do show the role that various parameters play in determining the noise reduction. In this way, the calculations suggest suitable methods by which the noise reduction in the actual shroud can be increased.

The noise reduction by resonant motion of the shroud is given in various frequency ranges by Eqs. (81-83). The coupling loss factors and modal densities required to evaluate these equations are plotted in Figs. 12 and 13. These parameters have been obtained for the OGO model from the equations developed in Section 3.4. Equation (83) was obtained by assuming that the AF modes below the ring frequency control the acceptance and transmission by resonant modes of the shroud. Reference to Figs. 12 and 13 shows that for the OGO model the factor $n_{2AF}\, \eta_{2AF,3}$ is more than 8 dB above the factor $n_{2AS}\, \eta_{2AF,3}$. Thus, the assumption that the AF modes control the noise transmission by resonant modes is valid.

The noise reduction predicted by Eqs. (81-83) for the OGO shroud model is plotted in Fig. 14. Two values of the dissipation loss factors η_3, η_{2AF}, and η_{2AS} have been used in these calculations to show the role of these parameters in determining the noise reduction. Note that between the ring frequency and the critical frequency a 5 dB increase in either η_{2AS} or η_3 produces a 5 dB increase in noise reduction. As it turns out, however, the noise transmission in this range of frequency is controlled by the forced wave or nonresonant motion of the shell.

Above the critical frequency, a factor of 3 increase* in the interior-space loss factor η_3 produces a 5 dB increase in the noise reduction. A similar increase in η_{2AF}, however, increases the NR by only 4 dB. This lack of proportionality can be explained physically. Increasing the dissipation loss factor of a group of modes acts to reduce the vibration amplitude of these modes. However, if the total losses by the modal group are dominated by the acoustic radiation losses, then an increase in the dissipation loss factor will not significantly reduce the vibration amplitude of the modes. This is often the case with AF modes, which are strongly coupled to the acoustic field. Thus, an increase in η_{2AF} does not produce a proportionate decrease in modal vibration amplitudes so that the noise reduction is not increased proportionately.

---

* A factor of 3 increase corresponds to a 5 dB increase.

The lack of proportionality between increases in shell modal loss factor and noise reduction is more significantly shown below the ring frequency. Here, a factor of 3 increase in η_{2AF} increases the NR by only 1 or 2 dB. Note also that below the ring frequency a similar increase in the interior acoustic space loss factor produces only a 4 dB increase in NR. This comes about because the net power flow into the interior space increases significantly as the modal energy of the space decreases due to the increased dissipation losses.

It can be said, in general, that the lower the noise reduction the more difficult it is to increase it by increasing the dissipation loss factors of the shell or the interior acoustic space. But, more importantly, it can generally be said that increases in acoustic space absorption are more effective in increasing the noise reduction by resonant modes than increases in structural damping.

To gain a more complete understanding of the role that various parameters play in determining the noise reduction by resonant modes, it is useful to obtain simple expressions that give an approximate value for the NR in a particular case. For example, we can find simplified expressions that give the NR of the OGO shroud model within 1 or 2 dB of the NR plotted in Fig. 14. For frequencies between the ring frequency and the critical frequency, Eq. (81) can be simplified by noting that the dissipation loss factor η_{2AS} is much larger than the coupling loss factor $\eta_{2AS,1}$, and that η_3 dominates η_3^{eq}. Thus, the NR is given approximately as

$$NR^{(res)} \approx 10 \log_{10} \left[\frac{\eta_{2AS}\,\eta_3}{\eta_{2AS,1}^{2}} \; \frac{n_3}{n_{2AS}} \right] , \qquad (90)$$

in the frequency range between the ring frequency, which is 650 Hz, and the critical frequency, which is 5000 Hz. Equation (87) explicitly shows those parameters that play the greatest role in determining the noise reduction.

Simplifications can be made also in Eq. (83). For our model of the OGO shroud, the coupling loss factor $\eta_{2AF,1}$ is larger than the loss factor η_{2AF}. Again, η_3^{eq} is dominated by η_3. Thus, the noise reduction can be expressed approximately as

$$NR^{(res)} \approx 10 \log_{10} \left[1 + \frac{2\eta_3}{\eta_{2AF1}} \frac{n_3}{n_{2AS}} \right] , \qquad (91)$$

for frequencies below the ring frequency. This equation indicates that the structural loss factor of the shell does not influence the NR below the ring frequency. As shown by the more exact calculations in Fig. 14, this is not exactly true. However, it represents a reasonable approximation.

To this point we have not considered the noise transmitted by nonresonant modes of the OGO shroud. The noise reduction due to nonresonant modes is given by Eq. (86) and Eq. (73). The parameter values used to evaluate these equations are listed in Table I. The noise reduction is calculated for assumed values of $\overline{\alpha}_3$ equal to 0.1 and 0.3. The results of these calculations are plotted in Fig. 14 and can be compared with the noise reduction due to resonant modes. Note that a factor of 3 increase in interior absorption increases the noise reduction 5 dB, while an increase in the shroud dissipation loss factor does not affect the noise reduction. This is physically explained by the fact that the nonresonant vibration amplitude is controlled by the coupling to the acoustic field and does not depend on the shroud damping.

The total noise reduction is found by superposition of the noise transmitted by resonant and nonresonant shell modes. Thus, the total noise reduction is given by the lower of $NR^{(res)}$ and $NR^{(nonres)}$ in Fig. 14. The total noise reduction is dominated by nonresonant modes for frequencies between the ring frequency and the critical frequency. For other frequencies, our calculation of $NR^{(nonres)}$ is not valid. It is clear from Fig. 14, however, that the total noise reduction for these frequencies is controlled by resonant shroud modes.

In conclusion, we can state as a general result for most spacecraft shrouds that the noise reduction is controlled by modes that are well-coupled to the sound field, whether they are resonant or nonresonant. It can be further stated that increased damping of the shroud will be less effective in increasing the noise reduction than will the addition of acoustically absorptive material in the interior acoustic space.

3.7 Response of the Shroud to Acoustic Excitation

Before proceeding to a general formulation of the spacecraft panel response to acoustic excitation, we formulate the response of the shroud. This formulation is used in Chapter 5 to predict the amount of vibratory energy that flows into the mechanical transmission path.

The resonant and nonresonant response of the shroud is treated separately. As would be expected, the resonant response is much greater than the nonresonant response of the shroud. The nonresonant response, however, which follows the mass law, serves as a reference level for the total response.

Finally, in Section 3.7.3 the response of a model of the OGO shroud is calculated as an example.

3.7.1 Resonant Response of the Shroud

The resonant response of the shroud can be found through the power-balance Eqs. (19a) and (19b). The remaining power-balance equations are not needed, since we can express the internal acoustic-space modal group energy through the calculation of noise reduction in the preceding section. Equations (19a) and (19b) can be solved to give

$$E_{2AF} = \frac{\eta_{2AF,1} \, (n_{2AF}/n_1) \, E_1 + \eta_{2AF,3} \, (n_{2AF}/n_3) \, E_3}{\eta_{2AF,1} + \eta_{2AF,3} + \eta_{2AF}} \qquad (92)$$

and

$$E_{2AS} = \frac{\eta_{2AS,1} \, (n_{2AS}/n_1) \, E_1 + \eta_{2AS,3} \, (n_{2AS}/n_3) \, E_3}{\eta_{2AS,1} + \eta_{2AS,3} + \eta_{2AS}} \quad . \qquad (93)$$

The interior-space modal group energy in these equations is given by

$$\frac{E_3}{E_1} = \frac{n_3}{n_1} \, 10^{-0.1 \, NR} \quad . \qquad (94)$$

As in the last section, we assume that the coupling loss factors $\eta_{2AS,1}$ and $\eta_{2AF,1}$ equal $\eta_{2AS,3}$ and $\eta_{2AF,3}$, respectively. With these results and with Eqs. (21) and (22), the mean square resonant-response spectrum is given by

$$\frac{S_a^{(2)}(f)}{S_p^{(1)}(f)} = \frac{\pi c_o}{\rho_s^{(2)} A_2 \rho_o} \left[\frac{n_{2AF}\,\eta_{2AF,1}}{2\eta_{2AF,1}+\eta_{2AF}} + \frac{n_{2AS}\,\eta_{2AS1}}{2\eta_{2AS1}+\eta_{2AS}}\right]\left[1+10^{-0.1NR}\right] . \tag{95}$$

For particular cases, Eq. (95) can be simplified. The NR by most shrouds is greater than 5 dB in the multimodal frequency range. Thus, the excitation of the shroud by the interior sound field can be neglected in comparison to the excitation by the external field. Also, the response of AS modes can usually be neglected in comparison to that of AF modes. Thus, Eq. (95) can be written in different frequency ranges as

$$\frac{S_a^{(2)}(f)}{S_p^{(1)}(f)} \approx \frac{\pi c_o}{\rho_s^{(2)} A_2 \rho_o} \left[\frac{n_{2AF}\,\eta_{2AF,1}}{2\eta_{2AF,1}+\eta_{2AF}}\right] , \text{ for } f<f_r \text{ or } f>f_c , \tag{96a}$$

and

$$\frac{S_a^{(2)}(f)}{S_p^{(1)}(f)} = \frac{\pi c_o}{\rho_s^{(2)} A_2 \rho_o} \left[\frac{n_{2AS}\,\eta_{2AS,1}}{2\eta_{2AS,1}+\eta_{2AS}}\right] , \text{ for } f_r<f<f_c . \tag{96b}$$

Note that, if the coupling loss factor is much greater than the dissipation loss factor, then the shroud response does not depend on its dissipative damping but is controlled by its acoustic radiation losses.

3.7.2 Nonresonant Response of the Shell

For the frequency range between the ring frequency and the critical frequency, the composite response of nonresonant modes follows the random-incidence mass law. The mean square nonresonant velocity spectrum is given in Eq. (70). It can be directly used to obtain the nonresonant acceleration spectrum:

$$\frac{S_a(f)}{S_p(f)} = \frac{2}{\left[\rho_s^{(2)}\right]^2} \left\{ 1 - \frac{2\rho_o c_o}{\omega\, \rho_s^{(2)}} \tan^{-1}\left(\frac{\omega \rho_s^{(2)}}{2\rho_o c_o}\right) \right\} . \quad (97)$$

The second term in this equation is a correction to account for radiation loading of the structure. Most structures radiating into air are sufficiently heavy that the correction term is unimportant at the frequency range being considered. Thus, we can express an approximation of the forced, nonresonant response as

$$\frac{S_a(f)}{S_p(f)} \approx \frac{2}{\left[\rho_s^{(2)}\right]^2} . \quad (98)$$

The mass-law response predicted by Eq. (98) represents a limit in that the addition of structural damping cannot reduce the total response of the structure below this level.

3.7.3 Response of a Model of the OGO Shroud

As an example of the general formulation in the previous two sections, we calculate the response of a model of the OGO shroud. This calculated response is used in Chapter 5 to predict the amount of energy transmitted along the mechanical path to a model of the OGO spacecraft.

The predicted response in this section may not be accurate for the actual OGO shroud, since the disspation loss factors of the OGO shroud are not known. The calculations indicate, however, that in certain frequency ranges the dissipation loss factors do not control the response of the shroud. For these frequencies, reasonable agreement is expected between the predicted and actual response levels of the OGO shroud.

The resonant response of the OGO shroud model is given by Eqs. (96). These equations require that the noise reduction be greater than 5 dB. Reference to Fig. 14 shows that this condition is satisfied by the OGO shroud.

The predicted response levels in dB re 1 g for two values of the loss factor η_{2AF} and η_{2AS} are presented in Fig. 15. These levels are obtained from Eq. (95) by the relationship

$$AL_2 - SPL_1 = 10 \log_{10} \frac{S_a^{(2)}(f)}{980^2} - 10 \log \frac{S_p^{(1)}(f)}{0.0002^2} , \qquad (99)$$

where AL is the acceleration level re 1 g, SPL is the excitation sound pressure level re 0.0002 μbar, and S_a and S_p are in cgs units. Below the ring frequency and above the critical frequency, the predicted acceleration levels are greatly increased due to the presence of AF modes in the shell. Note that a factor of 3 increase in the structural loss factor reduces the response 5 dB for all frequencies, except below the ring frequency. In this frequency range, the AF modal responses are radiation-loss controlled so that a factor of 3 increase in damping does not reduce the response proportionately.

Since the shroud response is not strongly dependent on the dissipation loss factor it is expected that the predicted response will be reasonably accurate for the actual shroud.

3.8 Response of the Spacecraft Panels to Acoustic Excitation

In this section, we calculate the response of the spacecraft panels to acoustic excitation by the interior sound field. This calculation is combined with the calculation of noise reduction in Chapter 5 to predict the response of the OGO spacecraft panels to acoustic excitation of the shroud. In the present section, we treat resonant and nonresonant response separately.

3.8.1 Resonant Response of the Spacecraft Panels

The resonant response of the spacecraft panels can be calculated through the power-balance Eqs. (19d) and (19e). These equations predict that

$$E_{4AF} = \frac{\eta_{4AF,3}}{\eta_{4AF,3} + \eta_{4AF}} \frac{n_{4AF}}{n_3} E_3 \qquad (100)$$

and

$$E_{4AS} = \frac{\eta_{4AS,3}}{\eta_{4AS,3} + \eta_{4AS}} \frac{n_{4AS}}{n_3} E_3 \quad . \tag{101}$$

In the flat spacecraft panels, all modes below the critical frequency are AS, while all modes above this frequency are AF. Thus, either Eq. (100) or (101) gives the total energy of resonant modes in the panels. Using Eqs. (21 - 23), the spectral acceleration of the panel is

$$\frac{S_a^{(4)}(f)}{S_p^{(3)}(f)} = \frac{\pi c_o n_3}{\rho_s^{(4)} A_4 \rho_o} \frac{E_4}{E_3} \quad , \tag{102}$$

where E_4 equals E_{4AF}, above the critical frequency, and E_{4AS} below this frequency.

3.8.2 Nonresonant Response of the Spacecraft Panels

The nonresonant response below the critical frequency of the spacecraft panels is given by the mass-law response, Eq. (98). As in the case of the shroud model, the radiation loading can be neglected, so that the forced response of the spacecraft panels can be written as*

$$\frac{S_a^{(4)}(f)}{S_p^{(3)}(f)} = \left[\frac{2}{\rho_s^{(4)}}\right]^2 \quad . \tag{103}$$

---

* The panels are excited on both sides by the sound field, so that the response predicted by Eq. (99) must be multiplied by two.

This response represents the smallest response that can be achieved by the addition of panel damping.

3.8.3 Response of a Model of the OGO Spacecraft Panels

As an example of the general formulation of the spacecraft panel response, we calculate the response of a model of the OGO spacecraft to excitation by the interior sound field. The spacecraft model is shown in Figs. 1 and 16, and is described in Section 3.1. The parameters describing this model are listed in Table I.

The resonant panel response is given by Eq. (102). The loss factors and modal densities required to evaluate this expression have been calculated from the equations in Section 3.4. These parameters are plotted in Figs. 12 and 13. The critical frequency of the OGO spacecraft panels is at 500 Hz, and is a factor of ten below the shroud critical frequency. This large difference occurs because the spacecraft panels are sandwich panels and have a higher bending-stiffness-to-weight ratio than the shroud. Since the critical frequency of the OGO panels is low, the panel response is radiation-loss controlled over a large range of frequencies. The resonant response predicted by Eq. (102) is plotted in Fig. 16, for two values of the dissipation loss factors η_{4AF} and η_{4AS}. In the range 200 to 2000 Hz, the response is reduced only slightly by a factor of 3 increase in the dissipation loss factor. For this reason, the predicted response of the panels to excitation by the interior noise field should be in reasonable agreement with the response of the actual OGO spacecraft panels.

The nonresonant mass-law response of the OGO panel models is given by Eq. (104), and is only a function of the panel surface density. This response, which is plotted in Fig. 16, can be compared with the resonant response. Because of the high bending-stiffness-to-weight ratio of the spacecraft sandwich panels, the resonant response is very much greater than the mass-law response. A similar result was found below the ring frequency for the shroud response. In that case, the bending-stiffness-to-weight ratio was high because of curvature of the shroud wall. In general, panel structures with high bending-stiffness-to-weight-ratios will have response levels significantly higher than the mass-law prediction.

This calculation concludes our study of the acoustic path. The particular calculations developed in this chapter are used in Chapter 5 to predict the spacecraft response to a sound field exterior to the shroud. First, however, we analyze the transmission of vibratory energy in the mechanical transmission path.

4. ANALYSIS OF THE MECHANICAL TRANSMISSION PATH

In this chapter, we find the response of the spacecraft panels to vibratory energy transmitted along the mechanical transmission path. The structural elements of this path are shown in Figs. 1 and 3. These elements are generally similar to those of the OGO spacecraft assembly. However, the structural parameters that describe them are left fairly general in the formulation, so that the results can be applied to other spacecraft assemblies. As an example, the spacecraft panel response is computed for a model of the OGO spacecraft assembly.

The discussion and calculations of this chapter closely follow those of Chapter 3. Thus, the background and validity of the prediction methods is not discussed in detail. The transmission of energy by resonant and nonresonant mounting truss motions is considered separately.

The first step in the analysis is to replace the elements of the actual spacecraft assembly with idealized models. These models are described in Section 4.1.

4.1 Detailed Description of the Mechanical Path Elements

The structural elements that make up the mechanical transmission path are shown in Figs. 1, 3, 17, 18, and 19. The exciting sound pressure field, element 1, and the shroud model, element 2, have been discussed in Section 3.1.

The spacecraft, element 4 in Fig. 3, is modeled in our theoretical analysis by four flat panels in an open-box configuration. The box is open at the top and bottom. The parameters required to describe the spacecraft panels are the total panel area A_4, the panel surface mass density $\rho_s^{(4)}$, the bending radius of gyration κ_4, and the longitudinal wavespeed $c_\ell^{(4)}$.

The modeling of the spacecraft by an open box of panels allows certain assumptions that would not be possible with a closed box. The open box is very responsive to torsional excitation around the axis of the connected edges. Thus we can neglect the mounting-truss motion that does not excite the box by torsion around this axis. The closed box, on the other hand, responds equally well to all excitations at the corners. Over all, however, it is significantly <u>less</u> responsive to excitation by the mounting trusses than is the open box. The method of analysis in this report would be valid for the closed box, but the resulting predictions of spacecraft panel vibration due to excitation by the mounting trusses would not be the same as the predictions obtained in this report.

Element 5, the ring frame, provides the principal support for both the spacecraft and the shroud. We have modeled this element by circular channel beam with radius a_5, lineal mass density $\rho_\ell^{(5)}$, wavespeed for flexure normal to the shroud $c_f^{(5)}$, and torsional wavespeed $c_t^{(5)}$. The beam is connected along its length to the base of the shroud and is, therefore, intimately coupled to its motion. Motion in the plane of the shroud wall is very small and can be neglected relative to the torsional and transverse flexural motions. The flexural wavespeed is given by

$$c_f^{(5)} = \left[\omega\kappa_f^{(5)} c_\ell^{(5)}\right]^{1/2} , \qquad (104)$$

where ω is the radian frequency, $c_\ell^{(5)}$ is the longitudinal wavespeed along the beam, and $\kappa_f^{(5)}$ is the radius of gyration for flexure normal to the shroud. This radius of gyration can be expressed in terms of the channel beam dimensions as

$$\kappa_f^{(5)} = \left[\frac{w(y-t/2)^2 + (x^3+y^3)/3}{a + w}\right]^{1/2} , \qquad (105)$$

where $x = a-y$ and $y = (a^2+wt)/2(a+w)$. The torsional wavespeed is given by

$$c_t^{(5)} = c_s \sqrt{K/J} , \qquad (106)$$

where c_s is the shear wavespeed along the beam, K is the stiffness constant for torsional motion, and J is the polar moment of inertia.[28]

The mounting trusses, element 6 in Fig. 3, are modeled by four straight channel beams with lengths ℓ_6, surface mass density $\rho_s^{(6)}$, torsional wavespeed $c_t^{(6)}$, and flexural wavespeed corresponding to flexure in the plane of the channel base, $c_f^{(5)}$ (see Fig. 19).

Because of the open-box construction of the spacecraft, flexure in the plane of the channel beam legs (the vertical plane) will induce negligible motion in the spacecraft panels--negligible, that is, compared to the motion induced by torsion and by flexure in the channel base plane. Therefore, in the analysis, we can neglect the vertical component of flexure.

The four mounting trusses are connected rigidly to the ring frame and to the corners of the spacecraft. In Figs. 17

and 19, the configuration of the spacecraft and ring frame relative to the mounting trusses is shown. Each mounting truss makes an angle of 0.44 radians, or approximately 25°, with the axis of the spacecraft.

The mounting trusses for an actual spacecraft assembly may be more complicated. For example, each mounting truss for the OGO spacecraft is a double beam (wishbone) connection between the corner of the spacecraft and the ring frame. We can model the double-beam truss by a single beam, provided that certain properties of the single beam truss--e.g., the torsional rigidity, the bending rigidity normal to the plane of the wishbone, and total mass--are chosen so as to be equal to that of the double beam truss.

The four structural elements of the mechanical transmission path form a connected set of multimodal systems. Thus, the next step in predicting the response of the elements by statistical energy analysis is the division of the modes in each element into groups of similar modes.

4.2 The Division of Modes of Each Element into Groups of Similar Modes

In our analysis of the acoustic path, it was necessary to divide the modes of the shroud into four groups. For the analysis in this chapter, however, this is no longer necessary, since all modes in the shroud are intimately coupled to both torsional and bending modes in the ring frame. Also, unlike the acoustic path analysis, nonresonant modes in the shroud can be neglected, since their energy is small and they are not more strongly coupled to the ring frame than are the resonant modes.

The modes of the ring frame and the mounting trusses must be divided into several groups. An appropriate grouping for a particular frequency band is shown in Fig. 20. The modes of the ring frame and mounting truss have been divided into resonant and nonresonant torsional modes and bending modes corresponding to bending in the vertical and horizontal planes. Also, the spacecraft panels have been divided into resonant and nonresonant modes.

We can now make a number of simplifications that allow power-flow interactions between certain sets of modes to be ignored or simplified. Motion of the ring frame in the vertical direction is inhibited by its connection to the shroud. Thus, we will not consider ring frame modes of flexure in the vertical plane, since these are restrained to have very small motion.

The spacecraft model that we have selected is very responsive to torsion around the vertical axes of the box. Such a torsion results from both torsional waves and flexural waves, with displacements parallel to x_1 in Fig. 21. Both of these motions are generated by flexure of the ring frame. Torsional waves in the ring frame generate flexural displacements in the x_2, x_3 plane, which will not produce axial torsion on the spacecraft. We therefore neglect torsional modes of the ring frame and bending modes in the x_1 direction of the mounting trusses, since the spacecraft panels are not excited by these modes.

In our consideration of the power flow, we allow the torsional- and bending-wave modes in each element to be coupled. This is a realistic allowance, since bending and torsional motions in beams with complicated cross sections are usually coupled by stiffness or inertial forces.

The paths of power flow that we consider in the statistical energy analysis are shown in Fig. 20. In Section 4.3, the power flow along these paths is formulated in terms of the modal group energies. In this way, expressions can be obtained for the acceleration spectrum of the elements in the mechanical path.

4.3 Formulation of the Power-Balance Equations

The modal groups outlined in Section 4.2 are all similarly coupled to the other groups of modes and are similarly damped. Thus, we can predict their time-average total energy in frequency bands, by using the fundamental power-balance equation, Eq. (17). In our formulation, we assume that the energy level in the shroud is known and is given by the results of Chapter 3. In making this assumption, we have assumed that the power-flow interactions between the shroud and the ring frame are small in comparison to those between the shroud and the acoustic fields and the energy dissipated by the shroud. This will be true in all cases in which the ring frame and mounting trusses are not highly damped.

The power-balance equations can be simplified by assuming that the torsional and flexural modes in the mounting trusses are strongly coupled. This assumption is appropriate in most cases, since boundary conditions and complex cross-sections strongly couple these two sets of modes. Under the condition that these modal groups are strongly coupled, their modal energies will equipart:

$$\frac{E_t^{(6)}}{n_t^{(6)}} = \frac{E_f^{(6)}}{n_f^{(6)}} \quad , \tag{107}$$

where $n_t^{(6)}$ and $n_f^{(6)}$ are the modal densities for flexural and torsional modes in the mounting truss. The case of equipartition of modal energy allows two groups of modes to be considered together, even though they are not similarly coupled to the other groups of modes. The loss factors for the over-all group will be the average loss factor of each mode in the group, e.g.

$$\eta_{6,4} = \frac{n_t^{(6)} \eta_{6t,4} + n_f^{(6)} \eta_{6f,4}}{n_t^{(6)} + n_f^{(6)}} \quad . \tag{108}$$

We now obtain a set of power balance equations similar to those obtained for the acoustic path, in Chapter 3. Power balance on the resonant flexural modal group in the ring frame gives

$$\eta_{5,6}\, n_5 \left[\frac{E_5}{n_5} - \frac{E_6}{n_6}\right] - \eta_{5,2} n_5 \left[\frac{E_2}{n_2} - \frac{E_5}{n_5}\right] + \eta_5 E_5 + \frac{\Pi_{5,6NR}}{\omega} = 0 \ , \tag{109a}$$

where "5" refers to the flexural resonant modal group in the ring frame, "6" refers to the composite flexural and torsional resonant group in the mounting trusses, and $\Pi_{5,6NR}$ is the flow to nonresonant mounting-truss modes. In this equation, n_6 is the sum of resonant modes in all four mounting trusses. Power balance for the mounting-truss resonant modal group gives

$$\eta_{5,6}\, n_5 \left[\frac{E_5}{n_5} - \frac{E_6}{n_6}\right] - \eta_{6,4}\, n_6 \left[\frac{E_6}{n_6} - \frac{E_4}{n_4}\right] - \eta_6 E_6 = 0 \ . \tag{109b}$$

Power balance for the spacecraft panels gives

$$\eta_{6,4} n_6 \left[\frac{E_6}{n_6} - \frac{E_4}{n_4}\right] + \frac{\Pi_{6NR,4}}{\omega} - \eta_4 E_4 = 0 \quad , \qquad (109c)$$

where $\Pi_{6NR,4}$ is the power flow from nonresonant mounting-truss modes. This set of equations is used in Sections 4.6 and 4.7 to predict the spectral acceleration of the elements in the mechanical transmission path. As for the acoustic path, flow of energy in resonant and nonresonant modes is considered separately. First, however, we calculate the necessary coupling loss factors, dissipation loss factors, modal densities, and nonresonant power flow needed to evaluate the power-balance Eqs. (109).

4.4 Calculation of the Modal Densities and Loss Factors

Our next task is to evaluate the modal densities and loss factors that appear in Eqs. (109). Fortunately, many of these parameters have already been found by other authors and appear in the literature. As in the case of the acoustic path elements, we do not find the exact parameters for any one system but, rather, we find expressions that are valid for an ensemble of similar structures which vary only in fine detail. In calculating coupling loss factors, we calculate the power flow between two infinite structures. We hypothesize that the average coupling loss factor between a mode in one element and a mode in the other element is given by this calculation.

4.4.1 Calculation of the Modal Densities

To evaluate the power-balance equations, we must know the torsional- and bending-wave modal densities in the ring frame and the mounting trusses. These modal densities for a straight beam are given in Ref. 15 and in our notation are

$$n_f(f) = \frac{\ell}{(\omega\kappa_f c_\ell)^{1/2}} \tag{110}$$

and

$$n_t(f) = \frac{2\ell}{c_t} \quad . \tag{111}$$

The above equations do not take into account the curvature of the ring frame. Only the lowest-order mode, however, corresponding to uniform radial motion is appreciably affected by curvature. Thus, the above equations are valid expressions for the modal densities of both the ring frame and the mounting trusses.

The modal densities of the shroud and spacecraft panels were calculated in Section 3.4.6.

4.4.2 Calculation of the Shroud to Ring-Frame Coupling Loss Factor

The ring frame is intimately attached along its full length to the shroud. Thus, we can presume that its coupling loss factor to the shroud will be large. More specifically, we presume that the ring frame to shroud coupling loss factor exceeds both the coupling loss factor to the mounting trusses and the dissipation loss factor

$$\eta_{5,2} \gg \eta_{5,6} + \eta_5 \tag{112}$$

4.4.3 Calculation of the Ring-Frame/Mounting-Truss Coupling Loss Factor

The required ring-frame/mounting-truss coupling loss factor, $\eta_{5,6}$, is the average coupling loss factor between flexural modes in the ring frame, with displacements normal to the shroud and flexural and torsional modes in the mounting trusses.

The vibrational field of the ring frame can be simulated by a number of traveling waves in an infinitely extended ring frame. The sum of the mean square amplitudes of the traveling waves in the infinite structure is related to the mean square displacement and time-average total energy of the ring frame by

$$|y_5|^2 = 4 \langle x_5^2 \rangle = \frac{4E_5}{\omega^2 M_5} \quad , \tag{113}$$

where $|y_5|^2$ is the sum of the mean-squared complex amplitude magnitudes of the traveling waves, $\langle x_5^2 \rangle$ is the space-time mean square displacement of the ring frame, M_5 is the total mass of the ring frame, and E_5 is its time-average total energy.
Our method of calculating $\eta_{5,6}$ is to find the power flow from a traveling wave in the infinitely extended ring frame of complex amplitude y_5 to a semi-infinite mounting truss. The coupling loss factor $\eta_{5,6}$ is then given by

$$\eta_{5,6} = \frac{4\Pi_{5,6}}{\omega\, E_5} \quad , \tag{114}$$

where $\Pi_{5,6}$ is the power flow from the traveling wave on the infinite ring frame to the semi-infinite mounting truss*, and E_5 is the time-average total energy in the ring frame corresponding to this traveling wave amplitude.

The infinite ring frame has an internal impedance as a source of excitation for one semi-infinite mounting truss. This impedance is the ratio of moment to angular velocity parallel to the spacecraft axis at the point of its attachment to the mounting truss. In terms of the ring frame parameters, assuming $e^{-i\omega t}$ time-dependence, this source impedance is[29]

$$Z_5 = 2(1 - i)\rho_{\ell 5}\, \kappa_{f5}^{\ 2}\, c_{\ell 5}^{\ 2}\, c_{f5}^{\ -1} \quad . \tag{115}$$

Ring-frame flexure will excite both torsional and flexural waves in the mounting truss. The ratio of the complex moment amplitude at the end of the truss to the resulting angular velocity amplitude is[30]

$$Z_6^{\ t} = \rho_{\ell 6}\, \kappa_{\phi 6}\, c_{t6} \tag{116}$$

where $\kappa_{\phi 6}$ is the polar radius of gyration of the mounting-truss cross section. The mounting-truss flexural impedance is taken to be the ratio of moment applied to a pinned end of the semi-infinite truss to the resulting angular velocity[31]:

$$Z_6^{\ f} = (1-i)\rho_{\ell 6}\, \kappa_{f6}^{\ 2}\, c_{\ell 6}^{\ 2}\, c_{f6}^{\ -1} \quad . \tag{117}$$

---

* The factor of four arises since there are four mounting trusses attached to the ring frame.

The total load impedance that the mounting truss presents to the ring frame at the attachment point is derived from $Z_6{}^t$ and $Z_6{}^f$. The junction between the ring frame and mounting truss is reconstructed in Fig. 21. The ring frame is constrained to have flexural displacements in the x_2 direction only.

Let Ω_t and Ω_f be the angular velocities due to mounting-truss torsion and flexure at the junction, as shown in Fig. 21. Since the ring frame will not allow angular velocity in the x_2 direction at the junction,

$$\Omega_f \cos\theta = \Omega_t \sin\theta \quad . \tag{118}$$

The axial (or x_3) component of angular velocity at the junction is

$$\Omega_3 = \Omega_f \sin\theta + \Omega_t \cos\theta \quad . \tag{119}$$

The torque producing this axial angular velocity at the junction is

$$\tau_3 = \tau_t \cos\theta + \tau_f \sin\theta \quad , \tag{120}$$

where τ_t and τ_f are related to the appropriate angular velocities by the impedances expressed in Eqs. (116) and (117). One has, therefore,

$$\tau_3 = \Omega_t Z_t \cos\theta + \Omega_f Z_f \sin\theta \quad . \tag{121}$$

We define the ratio of τ_3 to Ω_3 as the mounting-truss load impedance Z_6:

$$Z_6 = (Z_6^{\,t} + Z_6^{\,f} \tan^2\theta)(1 + \tan^2\theta)^{-1} \quad . \tag{122}$$

We see that this expression is correct, since the impedance obtained in the limits of $\theta = 0$ and $\theta = \pi/2$ is correct.

The power transferred from the ring frame to one infinite mounting truss can be expressed in terms of these impedances and Ω_5^o. Ω_5^o is the axial component of angular velocity of the ring frame at the junction with the mounting truss detached, and is expressed as

$$|\Omega_5^o|^2 = \omega^2 \, k_{f5}^{\,2} \, |y_5|^2 \quad , \tag{123}$$

where k_{f5} is the flexural wavenumber, and y_5 is the incident-wave amplitude. The power transferred is obtained by considering the equivalent circuit for the junction (Fig. 22):

$$\Pi_{5,6} = \frac{1}{2} \, |\Omega_5^o|^2 \left| \frac{Z_5}{Z_5 + Z_6} \right|^2 R_6 \quad , \tag{124}$$

where

$$R_6 \equiv \mathrm{Re}\,(Z_6) \quad ,$$

and $\Pi_{5,6}$ is the power transferred to the truss. Placing Eqs. (124) and (113) into Eq. (114), we get the desired coupling loss factor

$$\eta_{5,6} = \frac{8k_{f5}^2}{\omega M_5} \left| \frac{Z_5}{Z_5 + Z_6} \right|^2 R_6 \quad . \tag{125}$$

If Eqs. (115) and (122) are used, all the quantities contained in Eq. (125) can be calculated from basic structural parameters.

4.4.4 Calculation of the Mounting-Truss/Spacecraft-Panel Coupling Loss Factor

The coupling loss factor between the mounting trusses and the spacecraft panels is a composite loss factor for coupling between both torsional and flexural modes of the mounting trusses and the flexural modes of the spacecraft panels. Our method of calculating this coupling loss factor is similar to that used in Section 4.4.3. The mounting trusses and the spacecraft panels are replaced by semi-infinite structures and the power flow from traveling waves in the mounting trusses to the spacecraft panels is calculated. The traveling-wave complex amplitude magnitude corresponding to flexural modes in the trusses is given by

$$|y_6|^2 = \frac{4E_{f6}}{M_6\omega^2} \quad , \tag{126}$$

where E_{f6} is the time-average total energy of the flexural modes in the four trusses, and M_6 is the total mass of the four trusses. The traveling-wave complex amplitude magnitude corresponding to torsional modes is

$$|\Omega_{t6}|^2 = \frac{4E_{t6}}{M_6 \; \kappa_{\phi 6}^{\;2}} \quad , \tag{127}$$

where Ω_{t6} is the torsional wave angular velocity complex amplitude, E_{t6} is the time-average total energy of the torsional modes in the trusses, and κ_ϕ is the polar radius of gyration of the trusses. The coupling loss factor is given in terms of the power flow between the semi-infinite structures as

$$\eta_{6,4} = \frac{\Pi_{6,4}}{\omega \; E_6} \quad , \tag{128}$$

where $\Pi_{6,4}$ is the power flow from all four trusses to the panels, and E_6 is the torsional and flexural time-average total energy in the trusses.

Since we have allowed the torsional and flexural waves to be intimately coupled, the energy of each mode will be the same; i.e.,

$$\frac{E_{t6}}{n_{t6}} = \frac{E_{f6}}{n_{f6}} \quad , \tag{129}$$

where n_{t5} and n_{f5} are the modal densities of torsional and flexural modes. It follows that the total time-average energy is

$$E_6 = E_{t6} + E_{f6} = E_{f6}\left(1 + \frac{n_{t6}}{n_{f6}}\right) . \qquad (130)$$

At the junction between the mounting trusses and the spacecraft, the source impedance for torsion around the spacecraft axis is Z_6 and is given by Eq. (122). The load impedance Z_4 of the panels is taken to be that of a plate edge for a normal moment. This impedance, for the semi-infinite panel, has been computed by Eichler.[32] His expression is

$$Z_4 = \frac{\rho_s^{(4)} \kappa_4 c_{\ell 4}}{k_{f4}^{\,2}} \; \frac{(A-iB)}{A^2+B^2} \quad , \qquad (131)$$

where $A = 0.189$, $B = 0.275 \ln (k_{f4}\, w/2.5)$, k_{f4} is the flexural wavenumber, and w is the half-width of the mounting truss (see Fig. 19). The power transferred from one mounting truss to the panels is given by

$$\frac{\Pi_{6,4}}{4} = \frac{1}{2}\, |\Omega_6^o|^2 \left| \frac{Z_6}{Z_6 + Z_4} \right|^2 R_4 \quad , \qquad (132)$$

where $\Pi_{6,4}$ is the power flow from all four trusses to the panels, Ω_6^o is the total axial component of the truss angular velocity when it is pinned at the junction but the spacecraft is disconnected, and R_4 is the real part of Z_4. The total mean square axial component of angular velocity is the sum of components due to flexure and torsion in the mounting trusses:

$$\frac{1}{2} \left|\Omega_6^o\right|^2 = \frac{1}{2} k_{f6}^2 \omega^2 \left|y_6\right|^2 \sin^2\theta + \frac{1}{2} \left|\Omega_{t6}\right|^2 \cos^2\theta \quad . \tag{133}$$

Placing Eq. (133) in Eq. (132) and using Eqs. (126), (127), (130), and (128) to define $\eta_{6,4}$, we arrive at

$$\eta_{6,4} = 8 \frac{k_{f6}^2 R_4}{\omega M_6} \left| \frac{Z_6}{Z_6 + Z_4} \right|^2 \frac{\sin^2\theta + \frac{n_{t6}}{n_{f6}} \frac{\cos^2\theta}{k_{f6}^2 \kappa_{\phi,6}^2}}{1 + n_{t6}/n_{f6}} \quad . \tag{134}$$

The calculations of this coupling loss factor are clearly tedious and require the use of a digital computer.

4.4.5 Estimation of the Dissipation Loss Factors

At the present time, we must experimentally determine the internal loss factors η_4, η_5, and η_6 that describe the dissipation in the spacecraft, the ring frame, and the mounting truss. Some recent gains have been made in the estimation of internal damping of structures,[35] but they are not sufficiently advanced so that we can confidently use these estimates for engineering predictions. No experimental data on the OGO structure was available for our analysis; therefore, we estimated the dissipation loss factors on the basis of past experimental data from similar structures. The estimate that we obtained is

$$\eta_4 = \eta_5 = \eta_6 = 10^{-2} \quad . \tag{135}$$

4.5 Calculation of Nonresonant Vibration Transmission

In Section 4.3, we formulated the vibration transmitted from the ring frame to the spacecraft by resonant motion of the four mounting trusses. In this section, the vibration transmitted by nonresonant motion of the mounting trusses is formulated. In this formulation, the mounting trusses are represented as "pure stiffness elements." Thus, the three-element system (ring frame, mounting truss, and spacecraft) can be analyzed as a two-element resonant modal system (ring frame and spacecraft) with stiffness coupling, so that the fundamental result for power flow between two groups of resonant modes, Eq. (12), can be used.

In representing the mounting trusses as "pure stiffness elements," we are neglecting the mass-controlled, nonresonant motion of the mounting trusses. This idealized situation is in direct contrast to the case of acoustic noise transmission through the shroud, where only the mass-controlled motion was considered. It seems intuitively clear, however, that the bending and torsional modes of the mounting trusses will not respond significantly when excited at frequencies well above resonance.

The modal stiffness of a beam in bending or in torsion is, in general, different for each mode; therefore, it is not clear what value of coupling stiffness should be used in our formulation. We have chosen to use the static stiffness of the mounting trusses in bending and torsion. This choice is equivalent to considering the mounting trusses as massless.

The power flow from the ring frame to the spacecraft panels through nonresonant modes of the mounting trusses is given by

$$\Pi_{6NR,4} = \omega\eta_{5,6NR,4}\, n_5 \left[\frac{E_5}{n_5} - \frac{E_4}{n_4} \right] . \tag{136}$$

To calculate the ring-frame/spacecraft coupling loss factor $\eta_{5,4}$, we follow the procedure used in Sections 3.4.3 and 3.4.4. First, we calculate the time-average power transferred from an infinitely long ring frame to semi-infinite spacecraft panels when a bending wave traveling along the ring frame impinges on the ring-frame/mounting-truss junction. The desired coupling loss factor is then calculated from the relationship

$$\eta_{5,6NR,4} = \Pi_{6NR,4}/\omega\, E_5 \quad , \tag{137}$$

where $\Pi_{6NR,4}$ is the power transferred by all four mounting trusses, and E_5 is the time-average total energy associated with the incident bending wave in a section of the infinite ring frame that has the same length as the finite ring frame.

$$E_5 = \frac{M_5}{4k_{f5}^{\,2}} \left|\Omega_5^o\right|^2 \quad , \tag{138}$$

where k_{f5} is the flexural wavenumber; Ω_5^o is the complex angular-velocity amplitude at the ring-frame/mounting-truss junction when the mounting truss is detached, and M_5 is the total mass of the ring frame.

We now calculate the time-average power flow from the ring frame to the spacecraft when a traveling flexural wave with complex angular-velocity amplitude Ω_5^o impinges on the ring-frame/mounting-truss junction.

With the moment and angular-velocity vectors defined as in Fig. 23, the constitutive relations for the ring frame, mounting truss, and spacecraft are given by Eqs. (139a), (139b) and (139c), respectively:

$$\tau = Z_5 \Omega_5{}^i \quad , \tag{139a}$$

$$\tau = \frac{K}{i\omega}(\Omega_5 - \Omega_6) \quad , \tag{139b}$$

$$\tau = Z_4 \Omega_4 \quad , \tag{139c}$$

where $\Omega_5{}^i$ is the angular velocity induced in the ring frame by the reaction moment τ, Ω_5 and Ω_6 are the angular velocity components along the spacecraft axis at the ring-frame end and the spacecraft end of the mounting truss, K is the static stiffness of the mounting truss, and Ω_4 is the angular velocity at the spacecraft corner. The moment impedance Z_5 of the ring frame is given by Eq. (115) and the moment impedance Z_4 of the spacecraft is given by Eq. (131). The static stiffness K of the mounting truss is calculated later in this section.

Geometric compatibility for the ring-frame/mounting-truss junction and the mounting-truss/spacecraft junction requires that

$$\Omega_5 = \Omega_5^o - \Omega_5^{\,i} \ , \tag{140a}$$

and

$$\Omega_6 = \Omega_4 \quad . \tag{140b}$$

Combining Eqs. (138) and (140) yields the spacecraft angular-velocity amplitude Ω_4, in terms of the incident traveling-wave angular-velocity amplitude Ω_5^o :

$$\Omega_4 = \frac{KZ_5}{KZ_5 + KZ_4 + i\omega\, Z_4 Z_5}\ \Omega_5^o \quad . \tag{141}$$

The time-average power flow into the spacecraft from one mounting truss is

$$\frac{\Pi_{6NR,4}}{4} = \langle \mathrm{Re}[\tau e^{-i\omega t}]\ \mathrm{Re}[\Omega_4 e^{-i\omega t}] \rangle_t = \mathrm{Re}[\tau \Omega_4^{\,*}]/2 \ , \tag{142}$$

where $\Pi_{6NR,4}$ is the power flow from nonresonant motion of all four mounting trusses and Ω_4^* is the complex conjugate of Ω_4. Using Eqs. (139c) and (141) in Eq. (142) yields the desired expression for the time-average power flow:

$$\frac{\Pi_{6NR,4}}{4} = \frac{1}{2} \left| \frac{KZ_5}{K(Z_4 + Z_5) + i\omega Z_4 Z_5} \right|^2 \mathrm{Re}[Z_4]\ |\Omega_5^o|^2 \quad . \tag{143}$$

Equation (143) can be obtained also from the "equivalent circuit" shown in Fig. 24. The coupling loss factor $\eta_{5,6NR,4}$ follows from Eqs. (137), (138), and (143):

$$\eta_{5,6NR,4} = \frac{8k_5^2}{\omega M_5} \left| \frac{KZ_5}{K(Z_4 + Z_5) + i\omega Z_4 Z_5} \right|^2 \mathrm{Re}[Z_4] \quad . \qquad (144)$$

To conclude our formulation, we now calculate the static stiffness K. The angular-velocity amplitude at each end of the mounting truss can be resolved into a flexural and a torsional component, as shown in Fig. 21. The moment at each end of the truss can be resolved similarly. The bending moment τ_f and flexural components of the angular velocities at the ring-frame end, $\Omega_f^{(5)}$, and at the spacecraft end, $\Omega_f^{(6)}$, are related by

$$\tau_f = \frac{K_f}{i\omega} (\Omega_f^{(5)} - \Omega_f^{(6)}) \ , \qquad (145)$$

where K_f is the static stiffness of the truss in pure bending and is given by[33]

$$K_f = \frac{EA_6 \kappa_{f6}^2}{\ell_6} \quad , \qquad (146)$$

where E is the modulus of elasticity of the mounting truss material, A_6 is the mounting truss cross-section area, κ_{f6} is the radius of gyration of the mounting truss, and ℓ_6 is the length of one mounting truss.

The torsional moment τ_t and the torsional components of the angular velocities at the ring-frame end, $\Omega_t^{(5)}$, and at the spacecraft end, $\Omega_t^{(6)}$, are related by

$$\tau_t = \frac{K_t}{i\omega} (\Omega_t^{(5)} - \Omega_t^{(6)}) \quad , \tag{147}$$

where K_t is the static stiffness of the truss in pure torsion given by[33]

$$K_t = \frac{Gbt^3}{3\ell_6} \tag{148}$$

where G is the shear modulus of the truss material, b is the length of the truss cross section, (see Fig. 19), and t is the thickness of the truss cross section.

Equation (148) is actually the torsional stiffness of the rectangular section obtained by straightening out the truss cross section shown in Fig. 19. This calculation is justified by Prandtl's membrane analogy,[34] which shows that the torsional stiffness for thin, unclosed cross sections depends only on the length and thickness of the cross section.

The mounting-truss stiffness K in combined bending and torsion can be calculated in the same manner as the mounting-truss impedance, which is calculated in Section 4.4.3. The expression

$$K = (K_t + K_f \tan^2\theta)(1 + \tan^2\theta)^{-1} \tag{149}$$

is identical in form to Eq. (122).

The truss stiffness given by Eq. (149) can be used in Eq. (144), for the coupling loss factor $\eta_{5,4}$, and, finally, the power flow due to nonresonant mounting truss motion is given by Eq. (136).

4.6 Formulation of the Ring Frame to Shroud Response Ratio

In this section, we use the power-balance Eqs. (109) to predict the ratio of the ring-frame/shroud mean square acceleration spectra.

We note from power-balance Eq. (109a) that, if the ring-frame/shroud coupling loss factor $\eta_{5,2}$ is sufficiently large, modal energy equilibrium will exist between the shroud and the ring frame:

$$\frac{E_2}{n_2} = \frac{E_5}{n_5} \quad . \tag{150}$$

As discussed in Section 4.1, the ring frame is intimately attached along its full length to the shroud. Thus, we can presume that its energy coupling to the shroud will be large enough that Eq. (150) is a valid estimate of the ring-frame flexural modal group energy.

The modal densities n_2 and n_5 are given by Eqs. (35) and (110), respectively, while the total modal group energy in the structural elements is related to their mean square acceleration spectra by

$$S_a^{(i)}(f) = \frac{2\omega^2 E_i}{M_i \Delta} \quad , \tag{151}$$

where E_i is the time-average total energy of the structure, M_i is its total mass, and Δ is the bandwidth of excitation. Thus, we can express the ratio of the ring-frame mean square acceleration spectrum to the shroud mean square acceleration spectrum as

$$\frac{S_a^{(5)}}{S_a^{(2)}} = \frac{M_2}{M_5} \frac{n_5(f)}{n_2(f)} \quad . \tag{152}$$

As an example, we calculate the acceleration spectrum ratio between models of the OGO ring frame and shroud. These models are described in Section 3.1 and 4.1, and parameter values representing them are given in Table I. The modal densities of these models have been calculated from Eqs. (35) and (110) and were used to evaluate Eq. (152). The predicted response ratio for the OGO ring frame and shroud is plotted in Fig. 26. This prediction, of course, is limited to the multimodal frequency region in which many modes resonate. We have somewhat arbitrarily required at least two modes per octave band. Because the modal density of the shroud is much larger than the modal density of the ring frame, its acceleration spectrum is also much greater than that of the ring frame. In addition, the response ratio decreases with frequency as a direct consequence of the difference in modal density between the one-dimensional ring frame and the two-dimensional shroud.

In the general formulation of the ring-frame response, we disregarded the nonresonant modal response. Based on a mass-law behavior, the forced nonresonant response of the OGO ring frame is approximately 3 dB below its resonant response for all frequencies, so that neglect of the nonresonant response is warranted. In calculations for other spacecraft assemblies, the forced response of the ring frame should be calculated to make sure that it can be neglected.

4.7 Formulation of the Spacecraft-Panel/Ring-Frame Response Ratio

In this section, we calculate the ratio of the spacecraft-panel acceleration spectrum to the ring-frame acceleration spectrum. This calculation is combined with the calculation of the ring-frame/shroud response ratio in Chapter 5, in order to predict the response of the spacecraft panels to energy transmitted by the mechanical transmission path. In calculating the spacecraft-panel/ring-frame response ratio, we use the power-balance Eqs. (109). Power flow due to resonant and nonresonant motion of the mounting trusses is considered separately.

The ratio of spacecraft-panel time-average total energy to ring-frame energy due to power transmitted by resonant truss motion is calculated from the power-balance equations, with $\Pi_{6NR,4}$ equal to zero:

$$\left(\frac{E_4}{E_5}\right)^{res} = \eta_{5,6}\,\eta_{6,4}\,[(\eta_6+\eta_{6,5}+\eta_{6,4})(\eta_4+\eta_{4,6})-\eta_{6,5}\eta_{4,6}]^{-1} \;, \tag{153}$$

where the loss factors $\eta_{5,6}$ and $\eta_{6,4}$ are related by the symmetry relation

$$n_6\,\eta_{6,5} = n_5\,\eta_{5,6} \quad . \tag{154}$$

The modal densities and loss factors required to evaluate this equation were found in Section 4.4. The mean square acceleration spectra of the panels and the ring frame are related to the total energy in the elements by Eq. (151) so that the response ratio due to resonant-mode energy transmission is given by

$$\frac{S_a^{(4)}(f)}{S_a^{(5)}(f)} = \frac{M_5}{M_4}\,\frac{E_4}{E_5} \quad , \tag{155}$$

where E_4/E_5 is given by Eq. (153) and M_4 and M_5 are the total masses of the spacecraft panels and ring frame, respectively.

If the mounting truss has very light damping and is well-coupled to the ring frame and the spacecraft, then we can assume

$$\eta_6 << \eta_{6,5} + \eta_{6,4} \quad . \tag{156}$$

In this event, Eq. (153) simplified to

$$\left(\frac{E_4}{E_5}\right)^{\text{res.}} = \frac{\eta_{5,6}\,\eta_{6,4}}{\eta_4\,\eta_{6,5} + \eta_4\,\eta_{6,4} + \eta_{6,5}\,\eta_{4,6}} \quad . \qquad (157)$$

To calculate the response ratio due to energy transmitted by nonresonant truss modes alone, we set equal to zero the input power from the ring frame to the resonant mounting truss modes; to do this we set E_5 equal to zero in the power-balance equations. Then, we solve for E_4 in terms of the nonresonant mode power flow $\Pi_{6NR,4}$.

$$E_4 = \frac{\Pi_{6NR,4}}{\omega\left[\eta_4+\eta_{4,6} - \dfrac{\eta_{6,4}\eta_{4,6}}{\eta_{6,5}+\eta_{6,4}+\eta_6}\right]} \quad . \qquad (158)$$

Equation (158) expresses a power balance between power into the panels from the nonresonant truss modes, power dissipated in the panels, and power lost to the resonant modes of the trusses. In most cases, the second and third bracketed terms in Eq. (158), which account for power lost to the resonant mounting truss modes, can be neglected. Then, Eq. (158) becomes

$$E_4 = \frac{\Pi_{6NR,4}}{\omega\eta_4} \quad . \qquad (159)$$

In Section 4.5 the power from nonresonant modes was found as

$$\Pi_{6NR,4} = \omega\eta_{5,6NR,4}\, n_5 \left[\frac{E_5}{n_5} - \frac{E_4}{n_4}\right] . \qquad (136)$$

Using this equation in Eq. (158) and solving for the ratio E_4 to E_5 gives

$$\left(\frac{E_4}{E_5}\right)^{\text{nonres.}} = \frac{\eta_{5,6NR,4}}{\eta_{4,6NR,5} + \eta_4} , \qquad (160)$$

where $\eta_{5,6NR,4}$ and $\eta_{4,6NR,5}$ are related by the symmetry relation, Eq. (154), and $\eta_{5,4}$ is given by Eq. (144). The desired spectral response ratio is found by using Eq. (152) to relate these energies to the mean square acceleration spectra.

4.7.1 Calculation of the Spacecraft-Panel/Ring-Frame Response Ratio for a Model of the OGO Assembly

As an example, we calculate the response ratio of the spacecraft panels to the ring frame for a model of the OGO assembly. The required modal densities and loss factors for this assembly have been calculated from the results of Section 4.4. The loss factors are plotted in Fig. 25. These parameters can be used to evaluate Eqs. (153) and (159) for the ratios of the panel response to the ring-frame response due to resonant and nonresonant motions of the mounting trusses. These ratios are plotted in Fig. 26. Note that the responses due to resonant motion and nonresonant motion are comparable. At high frequencies, the response due to resonant motion dominates, while at low frequencies the response due to nonresonant motion dominates.

This concludes our study of the mechanical transmission path. In the next chapter we compare the spacecraft-panel response due to transmission of energy by the acoustic path and the mechanical path, for a model of the OGO spacecraft assembly.

5. COMPARISON OF THE RESPONSE OF A MODEL OF THE OGO SPACECRAFT TO ACOUSTIC EXCITATION AND MECHANICAL EXCITATION

In the first four chapters of this report, we developed a general method for predicting the response of spacecraft assembly elements to excitation by an external sound field. To illustrate the method, response ratios of individual elements in a model spacecraft assembly were calculated. In this chapter, we combine these individual calculations in order to predict the response of the model spacecraft panels to the external sound field. The response due to energy transmitted by the acoustic and mechanical transmission paths is considered separately.

We consider a model of the OGO spacecraft assembly. Its elements are discussed in Sections 3.1 and 4.1 and are illustrated in Figs. 1 and 17-19. Parameters of this model appropriate for the actual OGO assembly are listed in Table I.

5.1 Response of the Panels to Acoustic-Path Excitation

The response of the model spacecraft panels to energy transmitted by the acoustic path can be found through the noise reduction, plotted in Fig. 14, and the spacecraft response to an exciting diffuse noise field, plotted in Fig. 16. The mean square acceleration spectrum of the panels is given by

$$\left[\frac{S_a^{(4)}(f)}{S_p^{(1)}(f)}\right]^{\text{acoustic}} = \frac{S_p^{(3)}(f)}{S_p^{(1)}(f)} \, \frac{S_a^{(4)}(f)}{S_p^{(3)}(f)} , \qquad (161a)$$

or, equivalently,

$$10 \log_{10} \frac{S_a^{4}}{S_p^{1}} = 10 \log \frac{S_a^{4}}{S_p^{3}} - NR \quad . \qquad (161b)$$

To evaluate Eqs. (161), the noise reduction is taken from Fig. 14, with $\eta_2=10^{-2}$ and $\bar{\alpha}_3=0.1$. The spacecraft response to the internal acoustic field is taken from Fig. 16 with $\eta_4=10^{-2}$. The predicted spacecraft response due to energy transmitted by the acoustic path is plotted in Fig. 27. It is compared to the response due to mechanical-path energy transmission.

The loss factors η_2 and η_4 are not based on experimental or theoretical calculations, but are estimated on the basis of past experience. Thus, the predicted response levels should be viewed with some uncertainty.

5.2 Response of the Panels to Mechanical-Path Excitation

The response of the model spacecraft panels to energy transmitted by the mechanical path is given by

$$\left[\frac{S_a^{(4)}(f)}{S_p^{(1)}(f)}\right]^{\text{mechanical}} = \frac{S_a^{(2)}(f)}{S_p^{(1)}(f)} \; \frac{S_a^{(4)}(f)}{S_a^{(2)}(f)} \quad , \qquad (162a)$$

or, equivalently,

$$10 \log \frac{S_a^{(4)}}{S_p^{(1)}} = 10 \log \frac{S_a^{(2)}}{S_p^{(1)}} + 10 \log \frac{S_a^{(4)}}{S_a^{(2)}} \quad , \qquad (162b)$$

where the shroud response to the acoustic excitation, $S_a^{(2)}/S_p^{(1)}$, is plotted in Fig. 16, and the spacecraft response to mechanical excitation, $S_a^{(4)}/S_a^{(2)}$, is plotted in Fig. 26. The predicted spacecraft-panel response due to energy transmitted by the mechanical path is plotted in Fig. 27 and can be compared with the response due to acoustic-path energy transmission. The acoustic-path response dominates the over-all response of the model spacecraft panels.

5.3 Discussion of the Predictions

The response predictions in Fig. 27 clearly show that the acoustic path energy transmission dominates the over-all response of the OGO spacecraft panels. The validity of this prediction depends, of course, on the validity of the model analyzed and on the validity of the prediction method.

In modeling the actual OGO assembly, we have made a number of idealizations, which are discussed in Section 3.1 and 4.1. We are reasonably confident that these idealizations do not significantly affect the validity of the model--i.e., they do not change the response predictions in any octave frequency band by more than a factor of 3 (5 dB). The structural properties of the model are listed in Table I. These properties were taken from drawings of the OGO assembly supplied by NASA and are viewed as sufficiently accurate.

The dissipation loss factors are, by far the largest source of uncertainty in the predictions. These loss factors were necessarily based on empirical estimates, which may not be accurate for the OGO assembly. Before a great deal of confidence can be placed in the predictions, the dissipation loss factors for the actual OGO assembly should be found experimentally. Appropriate experimental methods for determining this parameter are discussed in Appendix A of this report.

Many of the concepts used in statistical energy analysis have been supported by experiment. This is particularly true with regard to the prediction of energy interactions between two acoustic or structural elements. Experimental support of transmission problems in which many acoustic and structural elements interact is not as extensive. A set of experiments for a multi-element spacecraft assembly is outlined in Appendix A. These experiments would lead to a greater understanding of such problems and could be used to support the theoretical predictions of this report.

Finally, it should be pointed out again that statistical energy analysis leads to predictions of the average response levels of an ensemble of structures. Variations from this average are to be expected and can be appreciable when the number of modes in a given frequency band is low.

6. CONCLUSIONS

The study presented in this report provides the necessary guidelines for analyzing the vibration environment of spacecraft assemblies. Perhaps the most difficult step in the analysis is the selection of a model of the assembly in question. If statistical energy analysis is to be used, modelling of the assembly is simplified. Only gross geometric and structural properties are required. Small details such as panel boundary conditions, the exact geometry of the acoustic space, and the exact configuration of the shroud/ring-frame/mounting-truss connection are not required.

In this report, we have illustrated our analysis technique by obtaining the vibratory response of a model of the OGO assembly. The extent to which the results are an accurate prediction of the vibratory environment of the actual OGO assembly depends on the accuracy of the model. Because the primary goal of our study has been to develop a method of analysis rather than to obtain specific results, the model selected is oversimplified. We have neglected the contribution of the conical section of the shroud to the sound transmission. We have not considered the vibratory response of antennas, solar panels, or particular items of equipment in the spacecraft. We have considered the spacecraft to be an open array of panels, whereas on at least one OGO spacecraft it is a closed array of panels. Finally, we have not considered the mass-loading effect of instruments connected directly to the spacecraft panels. Two of the OGO spacecraft panels are heavily loaded with equipment. In spite of having neglected the above effects, we believe that the predicted spacecraft panel response is within 5 dB of the response of the actual OGO spacecraft panels. Our results (see Fig. 27) show that the acoustically induced response of the spacecraft panels is 10 to 25 dB greater than the response caused by mounting-truss vibrations. Thus, we conclude that the acoustically induced response of the actual OGO panels will dominate the total response of the panels. In addition, we conclude that the acoustic path is of greater importance for all spacecraft assemblies in which the spacecraft consists of an array of panels that are supported by mounting trusses. Spacecraft assemblies that are arrays of beams supported by a truncated conical structure (e.g., the Mariner) do not fit into this general class.

Once we have found a model that accurately describes the spacecraft assembly, the statistical energy analysis procedures described in this report can be followed. The results obtained, however, must not be accepted blindly. First, statistical energy analysis requires an accurate measure of the internal damping of the structural elements involved. Second, statistical energy analysis requires that there be many resonant modes, at least two or three, within each octave band of frequencies. The accuracy of the results provided by the analysis depends on the extent to which these two requirements are fulfilled.

NOTES AND REFERENCES

1. Lyon, R. H.; Maidanik, G.; Eichler, E.; and Coles, J. J.: "Studies of Random Vibration of Coupled Structures." BBN Rept. No. 967, vol. I (November 1962), prepared under Contract No. AF 33(657)-9118, Tech. Document Rept. No. ASD-TDR-62-205, ASTIA No. AD 405919.

2. Lyon, R. H.: "Boundary Layer Noise Response Simulation With a Sound Field," paper presented at the Second International Conference on Acoustical Fatigue, Dayton, Ohio, 29 April-1 May 1964.

3. Waterhouse, R. V.: "Interference Patterns in Reverberant Sound Fields." J. Acoust. Soc. Am., vol 27, pp. 247-258 (1955).

4. Ungar, E. E.: "Fundamentals of Statistical Energy Analysis of Vibrating Systems." Air Force Flight Dynamics Lab. Tech. Rept. No. AFFDL-TR-66-52, April 1966.

5. Power flow is also proportional to the difference in time-average kinetic energies.

6. Lyon, R. H.; and Maidanik G.: "Power Flow Between Linearly Coupled Oscillators." J. Acoust. Soc. Am., vol. 34, pp. 623-639 Eq. (9.35) (1962).

7. Scharton, T. D.: Sc.D. Thesis, Mass. Inst. Technol. (1965).

8. Beranek, L. L.: Noise Reduction. (McGraw-Hill Book Co., New York, 1960), Ch. 13.

9. See Ref. 6 above.

10. Lyon, R. H.; and Eichler, E.: "Random Vibration of Connected Structures." J. Acoust. Soc. Am., vol. 36, pp. 1344-1354 (1964).

11. Lyon, R. H.; and Scharton, T. D.: "Vibrational Energy Transmission in a Three Element Structure." J. Acoust. Soc. Am., vol. 38, pp. 253-261 (1965).

NOTES AND REFERENCES (cont'd)

12. Hilbert, D.; and Courant, R.: Methoden der Mathematischen Physik. (Springer-Verlag, Berlin, 1931), First ed., p. 400.

13. In this report, we define the spectrum such that

$$\int_{f_1}^{f_1+\Delta} S_p(f)\, df$$

gives the mean square pressure in $\mathrm{dyn}^2/\mathrm{cm}^4$ in the frequency band Δ, where Δ is measured in Hz (cycles per second).

14. Franken, P. A.; and Lyon, R. H.: "Estimation of Sound-Induced Vibrations by Energy Methods, With Application to the Titan Missile." Shock, Vibration and Associated Environments, Bulletin No. 31, Pt. III, pp. 12-26 (1963).

15. See, for example, Smith, P. W., Jr.; and Lyon, R. H.: "Sound and Structural Vibration." NASA CR-160, Sec. V.7.A, 1965.

16. Morse, P. M.: "Vibration and Sound." (McGraw-Hill Book Co., Inc., New York, 1948), Ch. VIII.

17. See, for example, Ref. 15, Eq. III. 7.

18. Heckl, M.: "Vibrations of Point-Driven Cylindrical Shells." J. Acoust. Soc. Am., vol. 34, pp. 1553-1557 (1962).

19. Bolotin, V. V.: "On the Density of the Distribution of Natural Frequencies of Thin Elastic Shells." J. Appl. Math. Mech., vol. 27, No. 2, 538-543 (Transl. from Soviet J.: Prikl. Mat. Mekh., vol. 27, No. 2, pp. 362-364 (1963).

20. Both Heckl and Bolotin have obtained densities of resonance frequencies. This density is one-half the density of modes.

21. Franken, P. A.: "Sound-Induced Vibrations of Cylindrical Vehicles." J. Acoust. Soc. Am., vol. 34, pp. 453-454 (1962).

NOTES AND REFERENCES (cont'd)

22. Manning, J. E.; and Maidanik, G.: "Radiation Properties of Cylindrical Shells." J. Acoust. Soc. Am., vol. 36, pp. 1691-1698 (1964).

23. Maidanik, G.: "Response of Ribbed Panels to Reverberant Acoustic Fields." J. Acoust. Soc. Am., vol. 34, pp. 809-826 (1962).

24. See, for example, Ref. 15, p. 175.

25. Smith, P. W., Jr.: "Sound Transmission through Thin Cylindrical Shells." J. Acoust. Soc. Am., vol. 29, pp. 721-729 (1957).

26. Properties of many acoustically absorptive materials are given in Ch. 12 of Ref. 8.

27. Lyon, R.H.: "Noise Reduction of Rectangular Enclosures With One Flexible Wall." J. Acoust. Soc. Am., vol. 35, pp. 1791-97 (1963).

28. Values of J and K for several structural cross sections are listed in Roark, *Formulas for Stress and Strain*. (McGraw-Hill Book Co., Inc., New York, 1954), third ed.

29. Heckl, M.: "A Compedium of Impedance Formulas." BBN Report. No. 774, Contract Nonr 2322(00), 26 May 1961, Eq. (VI-I).

30. Ungar, E. E.: "Mechanical Vibrations," Ch. 6 in *Mechanical Design and Systems Handbook*. (McGraw-Hill Book Co., Inc., New York, 1964) Ch. 6, pp. 6-44.

31. Ref. 29 Eq. VI-2.

32. Eichler, E.: "Plate Edge Admittances." J. Acoust. Soc. Am., vol. 36, pp. 344-348 (1964).

33. Crandall, S. H.; and Dahl, N. C.: *An Introduction to the Mechanics of Solids*. (McGraw-Hill Book Co., Inc., New York, 1957), Table 8.1.

34. Den Hartog, J. P.: *Advanced Strength of Materials*. (McGraw-Hill Book Co., Inc., New York, 1952), p. 10.

NOTES AND REFERENCES (cont'd)

35. Ungar, E. E.; and Carbonell, J. R.: "On Panel Vibration Damping Due to Structural Joints." Submitted for publication in the AIAA J.

APPENDIX A. EXPERIMENTAL ANALYSIS OF RANDOM LOAD TRANSMISSION TO A SHROUD-ENCLOSED SPACECRAFT

In this Appendix, we discuss a number of experiments that could be performed on a model of the OGO spacecraft-shroud assembly. These experiments would lead to a greater understanding of vibratory energy transmission in such systems. It is hoped, of course, that their results would support the theoretical analysis contained in this report. Such experimental support is desirable because many of the concepts used in the statistical energy analysis of transmission problems are in their early stages of development. We feel that the theoretical analysis gives a good picture of the transmission processes, but there always remain points that are difficult to resolve by theoretical analysis alone. The experience and techniques that would be developed by a set of experiments like those described in this Appendix would be invaluable for further applications of statistical energy analysis to the transmission of random loads in spacecraft assemblies.

In the following sections, we present some general guidelines and considerations for the design of the experiments. We also discuss scaling laws for acoustic and structural vibration experiments. Then, we outline specific experiments that are appropriate for studying a model of the OGO spacecraft assembly.

A1.1 General Considerations in the Design of Experiments

Experiments on structural configurations that are exposed to random acoustic environments are carried on for a wide variety of purposes. For example, environmental testing includes experiments that are designed to "proof test" a structure. In such tests, the structure is subjected to an anticipated environment and one determines whether or not its structural integrity and/or its operational behavior are affected by the environment. Tests may also be run at lower levels of excitation, to determine anticipated response at locations where sensitive equipment may be mounted. Vibration and acoustic specifications may be generated for particular equipments by such tests.

A second major class of experiments is designed merely to gather data on structural and acoustic parameters. These parameters are usually obtained experimentally, either because they cannot be conveniently calculated or because there is some wish to correlate a calculation with an experimental study. The experiments may be designed to gather only a few bits of structural information or they may be designed to define almost all of the major parameters of the system. In either case, the result of the experiment is a list of data that is to be used in theoretical analyses for the prediction of some other more complex bit of information about structural behavior. Many of the experiments that we describe here fall within this category. In fact, we propose measurements of many structural parameters that can be calculated from theoretical notions. In this way, vibration-transmission predictions that use the concepts of statistical energy analysis can be based upon as much experimentally derived information as possible.

There are also experiments that one might call "research tests." Such experiments are used to test theoretical calculations of modal density, response ratios, damping, or other parameters. They may also be used to test theoretical assumptions about the way that the structure is behaving in various segments, frequency ranges, or modes of motion. Most of the proposed experiments fall in this category.

The spacecraft assembly model that we analyze is shown in Fig. 1. The detailed structure of this model is shown in Figs. 4, 5, and 6, and is discussed in Chapters 3 and 4 of the text. The experimental model should be designed to be as flexible in use as possible. It should be easy to dismantle, and the addition of structural damping and acoustic absorption should be relatively simple. We do not feel that there are any conflicts between these requirements and the fundamental necessity for the model to be representable by the dynamical considerations outlined in Chapters 3 and 4.

To gain flexibility and to reduce the expense of an experiment, it is often desirable to construct a scale model of the spacecraft assembly. Appropriate scaling laws and the problems involved in scaling are discussed in the Section A1.2 of this Appendix.

A1.2 Scaling of Acoustic- and Structural-Vibration Experiments

A logical approach in designing scale models is through dimensional analysis. Using this approach, we must first determine those parameters that describe the actual spacecraft assembly and control the response spectra of the individual elements. Then, a set of independent dimensionless groups can be formed by dimensional analysis. In scaling, it is necessary only to keep each dimensionless group constant.

Earlier in this report, we proposed that the multimodal response spectrum of each element in the acoustic and mechanical transmission path can be formulated in terms of the diffuse-field excitation spectrum and bandwidth and the gross properties of the elements. More specifically, we proposed that

1. Acoustic spaces in the assembly are described sufficiently by their volumes, by the density and speed of sound of the contained acoustic media, and by their dissipation loss factors.

2. Panel structures, the shroud and spacecraft, are sufficiently described by their geometry, including curvature, and the location of ribs and baffles, their surface density, bending- and longitudinal-wave speed, and dissipation loss factors.

3. Beamlike structures, the ring frame, and the mounting trusses, are sufficiently described by geometry, including length, curvature, and the geometry of their connection to other elements, their lineal density, bending-, longitudinal-, and torsional-wave speeds, and dissipation loss factors.

The mean square response velocity in a frequency band Δ of each element in the assembly can be expressed as a general function of these parameters,

$$S_v^{(i)} \Delta = F\left[S_p \Delta , \Delta, f, V_i, \ell_i, \rho_o, \rho_s^{(i)}, \rho_\ell^{(i)}, c_o, c_\ell^{(i)}, c_b^{(i)}, c_t^{(i)}, \eta_i\right] \tag{A1.1}$$

where $S_v^{(i)}$ is the velocity spectrum of the ith element, S_p is the excitation sound-pressure spectrum; f and Δ are the band center frequency and bandwidth of the excitation; F[ ] represents a functional relationship; the V_i's are the acoustic space volumes; the ℓ_i's describe the over all geometry of the structural elements; ρ_o is the density of the media within the acoustic spaces; the $\rho_s^{(i)}$'s are surface densities; the $\rho_\ell^{(i)}$'s are lineal densities; c_o is the acoustic speed of sound; the $c_\ell^{(i)}$ are longitudinal-wave speeds; the $c_b^{(i)}$'s are bending-wave speeds; the $c_t^{(i)}$'s are torsional-wave speeds; and, finally, the η_i's are internal dissipation loss factors.

This general functional relationship can be simplified through the introduction of dimensionless groups. These groups are found through dimensional analysis:

$$\left(\frac{S_v^{(i)}\Delta}{c_o^2}\right) = F\left[\left(\frac{S_p\Delta}{\rho_o^2 c_o^4}\right), \left(\frac{\Delta}{f}\right), \left(\frac{V_i f^3}{c_o^3}\right), \left(\frac{\ell_i f}{c_o}\right), \left(\frac{c_\ell^{(i)}}{c_o}\right), \left(\frac{c_b^{(i)}}{c_o}\right), \left(\frac{\rho_s^{(i)} f}{\rho_o c_o}\right), \left(\frac{\rho_\ell^{(i)} f^2}{\rho_o c_o^2}\right), \left(\eta_i\right)\right] \qquad \text{(A1.2)}$$

Using the above result, it is possible to design scale models that simulate the behavior of the full scale assembly. It is necessary only to keep each dimensionless group constant in the scaling. For example, if we wish to construct a one-half scale model, then it is necessary to increase the test frequencies by a factor of 2, since the acoustic speed of sound cannot be easily changed. The remaining parameters must be scaled according to the dimensionless groups. If the acoustic speed of sound c_o is held constant, the longitudinal-, bending-, and torsional-wave speeds must also be kept constant. In the important case in which the structures are homogeneous, these wavespeeds can be held constant by reducing the bending radius of gyration by the same factor that the over all structure is scaled. No change of material is necessary.

The scaling of nonhomogeneous panels or beams by geometrically similar nonhomogeneous structures does not require a change in material. Modeling of nonhomogeneous panels by homogeneous panels, however, usually requires a change in material, to keep all dimensionless groups constant.

The problems involved in scaling are not the result of material requirements, since these usually need not be changed. Problems do arise, however, because of the increased test frequencies. Measurement problems occur because of increased accelerometer loading. In many cases, this particular problem can be solved by use of available lightweight accelerometers and theoretical corrections to the measurements. A more serious problem occurs because of air absorption. Our dimensionless groups require that the internal acoustic-space dissipation loss factor remain constant as the required test frequencies are increased. At very high frequencies, absorption in the acoustic space makes this impossible. Fortunately, however, the internal acoustic-space dissipation loss factor in spacecraft assemblies is high because of the presence of a shroud liner. This allows us to reduce the dissipation loss factor in the acoustic space of the scale model by removing part of the liner.

The structural dissipation loss factors also must be held constant as the required test frequencies are increased. This requirement imposes few problems, however, since these loss factors are not strongly dependent on frequency. The loss factors of the scale models can be increased or decreased to correspond to those in the actual structures.

In our theoretical predictions and in the dimensional analysis, we have assumed that the exact details of the structural and acoustic elements of the spacecraft assembly are unimportant in determining the response. This assumption can be supported by study of a scale model that satisfies the above requirements. The study would involve varying the small details of the model and finding the effect on the response. If no effect were found, the assumption would be supported. If an effect were found, however, correspondence between the scale model and the actual spacecraft assembly results may not exist. In such a case, it would be necessary to include these small details of the assembly in the dimensional analysis.

As a practical limit, scale-model test frequencies should not exceed 12 kcps. The frequency range of interest in the actual OGO assembly lies below 5 kcps. Thus, a one-half scale model can be used without encountering serious scaling difficulties. A one-third scale model could be used over most of the frequency range of interest. Serious scaling problems would exist only at the highest frequencies.

A1.3 Outline of Experiments on a Model of the OGO Assembly

In the more-detailed discussions to follow, the mechanical and acoustic transmission paths are treated separately as they were in the theoretical analyses. For each of the major acoustic and structural path elements, we describe experiments to determine those parameters that are most important in establishing the energy transfer and storage. For each element, we wish to study modal density, damping, and coupling loss factors. We also describe energy transmission experiments that are performed on various segments of the acoustic and vibrational path. Experiments on transmission of energy in the vibrational and acoustical paths, separately and together, are described. In order to study the individual elements and segments of the transmission path, a high degree of flexibility in the spacecraft model construction is necessary. This flexibility would not be available to us if we were studying an actual spacecraft assembly. The essential difference is not in the complexity of the system, but in the degree of ease with which one can dismantle the various segments of the model and then reconnect them and have the structure remain in its initial state. Let us begin our discussion by enumerating the experimental studies of the acoustic transmission path.

A1.3.1 Experimental Studies of the Acoustic Transmission Path

Element No. 1 in the acoustic transmission path is the exterior acoustic space and the sound field within it that excites the spacecraft shroud. Two major forms of the exterior sound field should be investigated. The simplest to generate experimentally and to correlate with analysis is the diffuse reverberant field. A diffuse sound field can be generated by exciting a large, reasonably "hard" room with a band of noise. Almost any large room is suitable for this purpose, provided that unusually large acoustic absorption (absorption coefficients greater than 30%, say, over major parts of the wall area) is not present.

> Experiment 1. A check on the diffusion of the sound field can be made by making microphone scans through the space to see whether the sound-pressure levels remain uniform on the average (variations less than ± 1 dB) as one moves about the space. Strong nonuniformities could result from excessive acoustic absorption in one part of the contained volume or perhaps a peculiar modal distribution. The existence of such effects indicates that the field is nondiffuse. The diffuseness of the field can be increased to some extent by the proper addition of reflectors and/or absorption material.

There are cases where a nondiffuse directive field may be more representative of the service environment of the vehicle than is a purely diffuse sound field. One goal of our experiments is to test possible differences in the shroud response and in its sound transmission under these two types of incident sound field.

A directive field can be created in a room by increasing the absorption in the room so that the "direct field" of the sound source extends out, perhaps, a distance of 10 to 15 ft from the sound projector (s). If the shroud is placed in this field, it will experience relatively more acoustic energy incident from the direction of the source.

> Experiment 2. The region around the source (s) in which a directive field exists can be found by a microphone scan throughout the room. The average levels will be highest near the source and will fall off until they reach the level of the reverberant field. If the direct field is not sufficiently strong, then the absorption of the room must be increased.

Item No. 2 in the acoustic path is the shroud model. The important parameters in the analytical prediction of the acoustic energy interactions for this model are the modal density, the acoustic coupling loss factor, and the dissipation loss factor. These parameters can be evaluated by mechanical and acoustic tests on the shroud model.

> Experiment 3. The modal density of the shroud model can be found at low frequencies by counting peaks in the response as the sinusoidal exciting frequency is altered. This technique is useful until the bandwidth of the individual resonant modes becomes comparable to the average frequency spacing between modes. For a model of the OGO shroud, the modal density is sufficiently high that this technique will be useful only up to approximately 40 Hz. A mode count cannot be carried out above this frequency; however, the technique of slowly varying the sinusoidal exciting frequency and studying the response can be used to discover any unusual modal distribution at low frequencies in which modes would bunch together in certain frequency ranges and be absent in other ranges. If an unusual distribution were found, it would be worthwhile to change rib positions and boundary conditions to find their effect on the distribution.

The shroud-to-acoustic-space coupling loss factor should be found for both the AF and AS modal group. Since the acoustically slow modes radiate from the ribs and ends of the cylinder, their contribution to the total radiation can be eliminated by removing the ribs and baffles from the ends of the shroud model.

Experiment 4. The AF mode coupling loss factor is found by removing the ribs and baffles and using a mechanical shaker to excite the shroud in a frequency band. The net power radiated to the acoustic field from the unbaffled shroud is

$$\Pi_{rad} = 2\omega\eta_{2AF,1}\, n_{2AF}\left(\frac{E_2}{n_{2tot}} - \frac{E_1}{n_1}\right),$$

where E_1 and E_2, the total time-average energy of the acoustic space and the shroud, can be measured by a multiplying the total mass by the space-time mean square velocity; n_{2tot} and n_1 can be predicted theoretically. The net power radiated to the acoustic field equals that dissipated:

$$\Pi_{rad} = \omega\eta_1 E_1 ,$$

where E_1 and η_1 are known by measurement and previous experiment. The coupling loss factor $\eta_{2AF,1}$ can be found through the above equations.

Experiment 5. The AS mode coupling loss factor can now be found by executing a similar procedure with the ribs and baffles in place. In this case, the net power radiated from the baffled shroud is

$$\Pi_{rad} = \omega\eta_{2AF,1}\, n_{2AF}\left(\frac{E_2}{n_{2tot}} - \frac{E_1}{n_1}\right)$$

$$+\eta\omega_{\ 2AS,1}\, n_{2AS}\left(\frac{E_2}{n_{2tot}} - \frac{E_1}{n_1}\right) ,$$

where only $\eta_{AS,1}$ and Π_{rad} are unknown. Π_{rad} is found through η_1 and E_1 so that $\eta_{2AS,1}$ can be found. The dissipation loss factors are measured by studies of the vibration decay rate when the excitation is removed.

Experiment 6. To measure the AF mode and AS mode coupling loss factor, a mechanical shaker is used to excite the ribbed, baffled shroud in frequency bands. If the power input from the shaker is stopped, the decay rate of shroud energy will be equal to the power radiated and dissipated.

$$-\frac{dE_2}{dt} = \omega\left(\eta_{2AF}n_{2AF} + \eta_{2AS,1}n_{2AS}\right)\left(\frac{E_2}{n_{tot}} - \frac{E_1}{n_1}\right)$$

$$+\ \omega\left(\eta_{2AF}n_{2AF} + \eta_{2AS}n_{2AS}\right)\frac{E_2}{n_{tot}} \quad ,$$

All parameters in this equation can be measured or have been found in previous experiments, except $(\eta_{2AF}n_{2AF} + \eta_{2AS}n_{2AS})$. If we assume that the loss factors are equal (this assumption cannot be easily checked), then η_{2AF} and η_{2AS} are given by the above equation.

These experiments complete the study of the parameters controlling the acoustic acceptance and radiation properties of the shroud. A similar set of experiments should be conducted on the spacecraft panel model.

The important properties of the interior volume (Element 3), for our study, are its acoustical absorption and its geometry. The absorption is measured by making decay rate measurements of the sound pressure in frequency bands, taking into account the loss calculations for the sound that is transmitted outward through the shroud into the surrounding space.

Experiment 7. To measure the interior acoustic space absorption, excite the interior space to its steady-state sound-pressure level. Then, stop the excitation. The decay rate will be equal to the power dissipated in the interior and exterior acoustic spaces plus the power dissipated in the shroud.

$$\frac{dE_3}{dt} = \omega\eta_1 E_1 + \omega(\eta_{2AF} n_{2AF} + \eta_{2AS} n_{2AS}) \left(\frac{E_2}{n_{tot}} \right) + \omega\eta_3 E_3 \quad .$$

In this equation, only η_3 is unknown. The remaining parameters have been evaluated in other experiments or can be measured.

The geometry of the acoustic space will determine the "diffusion" of the sound field within. Diffusion can be measured by conducting Experiment 1 for the interior acoustic space.

The second class of experiments is to be performed on various portions of the acoustic transmission path. First, the acoustic acceptance of the shroud should be studied. This is done by making the absorption of the interior space as low as possible and exciting the shroud with an external sound field.

> Experiment 8. Remove all acoustically absorptive material from the interior acoustic space. Excite the shroud model with a diffuse external sound field, and measure the space-time mean square vibratory response of the shroud by sampling the vibration levels at many locations. Then, increase the damping and again measure the vibration levels. Repeat the above procedure with a directive field.

Next, the noise reduction by the shroud should be studied. From the discussion in Chapter 3, it is clear that we should find the relative amount of sound transmitted through the shroud by forced-wave (nonresonant) and resonant response. Forced-wave transmission is independent of structural damping; therefore, a way to find the relative importance of forced-wave transmission is to increase the shroud damping. Any increase in noise reduction must be due to the decrease in resonant transmission.

> Experiment 9. Add an absorptive liner to the interior acoustic space and measure the resulting dissipation loss factor η_3. Then establish an external diffuse sound field

and measure the noise reduction. Repeat the experiment for a directive sound field. Add a large amount of damping to the shroud, and repeat the above two measurements. Change the interior acoustic-space absorption and repeat all of the above measurements.

Finally, the complete acoustic transmission path should be studied. Energy transmitted by the mechanical path can be eliminated by using an extremely soft mechanical suspension for the spacecraft.

Experiment 10. With the spacecraft model and shroud liner in place, excite the shroud with a diffuse sound field and measure the shroud response, the NR, and the spacecraft response. Repeat these measurements for a directive sound field. Change various parameters and study the changes in response.

This completes the study of the acoustic path. Next, we discuss a study of the mechanical path.

A1.3.2 Experimental Study of the Mechanical Path

In this section, we outline a number of experiments that should be performed on the mechanical-transmission path elements. These experiments have been divided into two classes. First, experiments to determine the modal densities and loss factors of the individual elements are described. Second, experiments on various portions of the mechanical-transmission path are studied.

First the modal densities of the ring frame and mounting trusses should be studied. Densities of both torsional and bending waves should be found by exciting the elements with a moment and a force.

Experiment 11. With the shroud and mounting trusses disconnected, excite the ring frame with a sinusoidal force of slowly varying frequency. Where possible, count the number of resonances in the response. Connect the shroud and trusses, but damp them heavily, and repeat the mode count.

Experiment 12. Repeat Experiment 11 for the mounting trusses applying a force in the two principle directions of flexure.

Experiment 13. Repeat Experiment 11 for the mounting trusses, with a moment excitation.

The above experiments are complicated by the interaction of torsional and bending modes and by the interaction of modes of one structure with another.

The resonant vibration of the spacecraft shroud forms the random environment of the ring frame. In the theoretical analysis, we assumed that the coupling loss factor from the ring frame to the shroud would be much larger than the ring-frame dissipation loss factor or its coupling loss factor to the mounting truss. This hypothesis can be tested by exciting the ring frame with bands of noise and observing its decay rate.

Experiment 14. Excite the ring frame with a band of noise and measure the resulting vibration levels in the shroud, ring frame, and mounting trusses. The coupling loss factors between these elements and the ring frame can be expressed in terms of these levels and the dissipation loss factors of the shroud and mounting trusses:

$$\eta_{5,2} n_5 \left(\frac{E_5}{n_5} - \frac{E_2}{n_2} \right) = \eta_2 E_2$$

and

$$\eta_{5,6} n_5 \left(\frac{E_5}{n_5} - \frac{E_6}{n_6} \right) = \eta_6 E_6$$

Experiment 15. Excite the ring frame with a band of noise and stop the excitation. The decay rate of the ring frame energy is given by

$$-\frac{dE_5}{dt} = \eta_{5,2}\left(\frac{E_5}{n_5} - \frac{E_2}{n_2}\right) + \eta_{5,6}n_5\left(\frac{E_5}{n_5} - \frac{E_6}{n_6}\right) + \eta_5 E_5$$

All parameters in this equation, except η_5, are known or can be measured.

The above experiments should be repeated for the mounting trusses, to find the coupling loss factor between the trusses and the ring frame and between the trusses and the spacecraft panel. In addition, the flexural- and torsional-vibration levels of the trusses should be measured when the ring frame is excited by noise. This measurement can be correlated with the equal modal-energy hypothesis made in Chapter 4.

Finally, we outline a set of experiments to study portions of the mechanical path. To eliminate the flow of energy in the acoustic path, the shroud can be removed and the ring frame excited directly by a mechanical shaker. The experimental results can then be determined in terms of the ring-frame energy.

Experiment 16. With the spacecraft and mounting trusses in place, excite the ring frame to a steady-state level. Then measure the resulting energy levels in the trusses and the spacecraft panels.

Since energy is transmitted by both resonant and nonresonant motion of the mounting trusses, Experiment 16 should be repeated with the trusses heavily damped. It would also be interesting to alter the structural configuration and find the effect on the response levels.

These brief discussions indicate the number and type of experiments that can be undertaken on the OGO model. The experiments take full advantage of the model's flexibility and its usefulness in allowing fairly complete calculations on the system. We strongly recommend that as many as possible of these measurements be carried out in order to develop the most complete picture for the system.

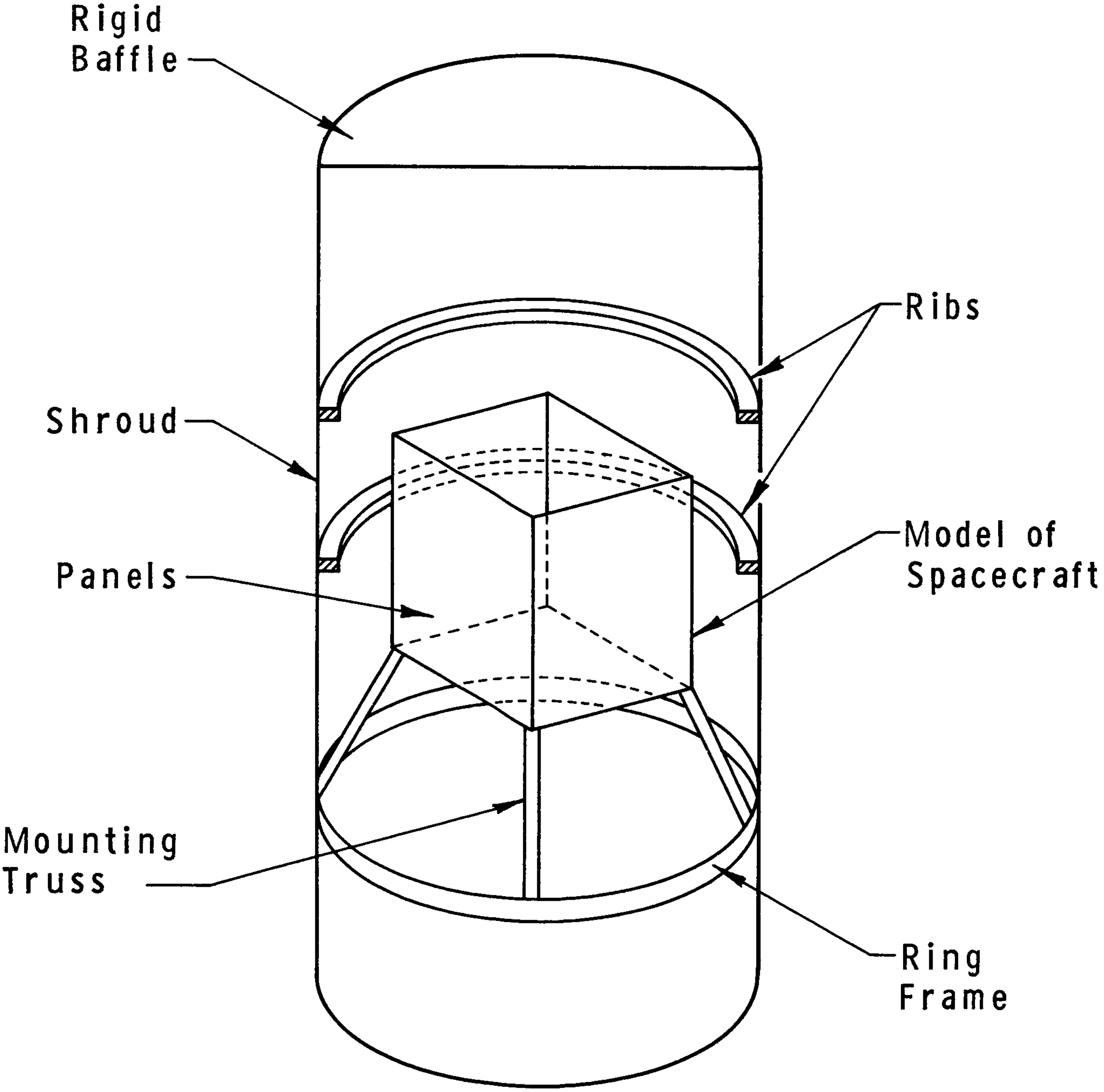

FIG. 1 DIAGRAM OF AN IDEALIZED MODEL OF THE OGO SPACECRAFT-SHROUD ASSEMBLY

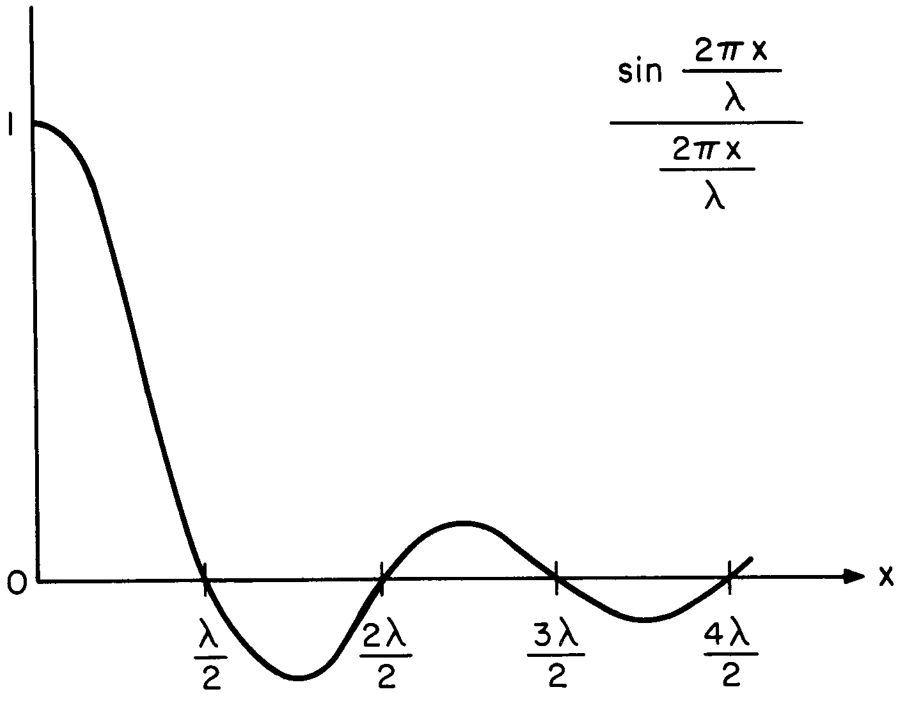

FIG. 2 SPATIAL CORRELATION OF NARROW BAND DIFFUSE SOUND FIELD

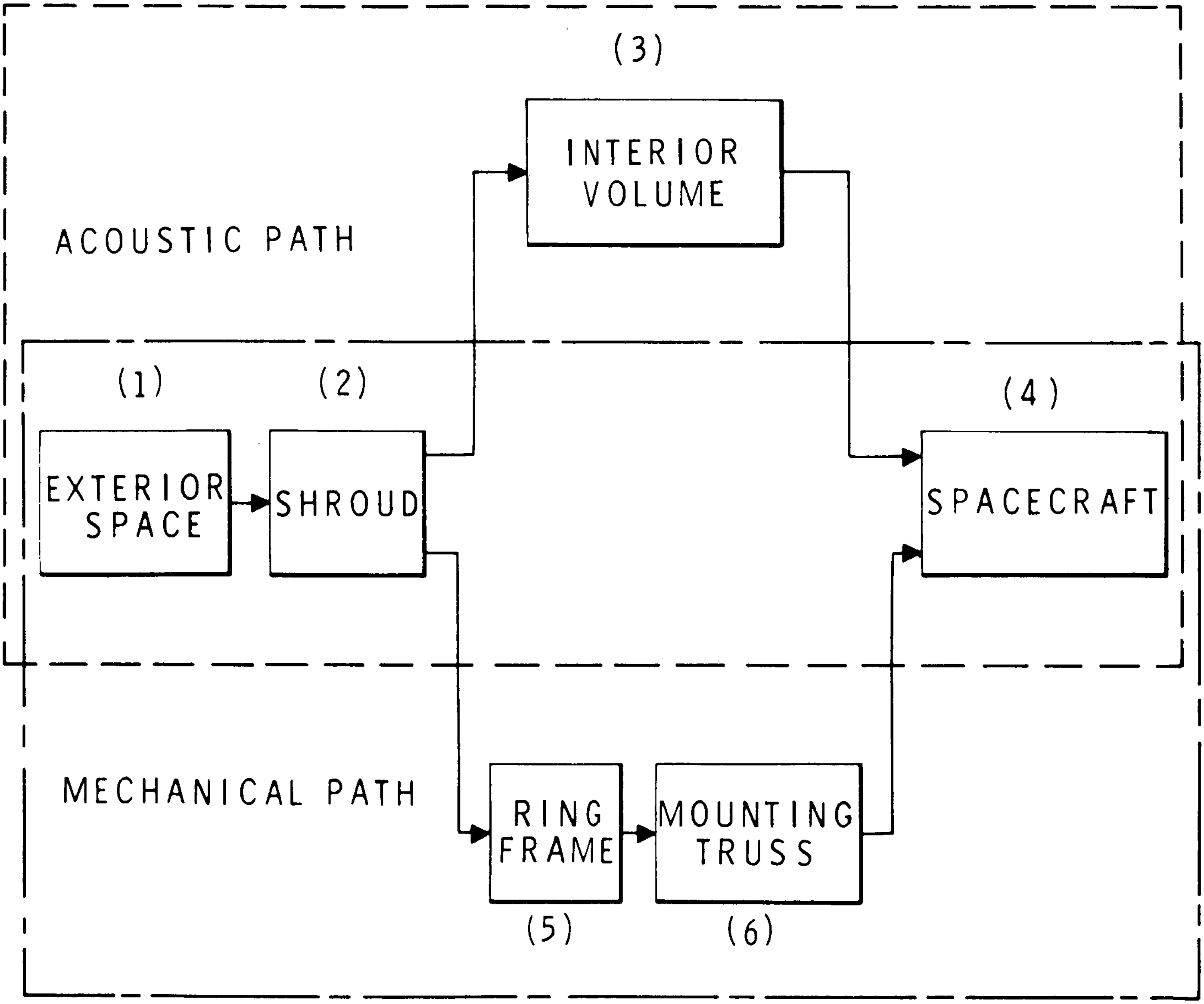

FIG. 3 ENERGY FLOW DIAGRAM FOR A SPACECRAFT-SHROUD ASSEMBLY

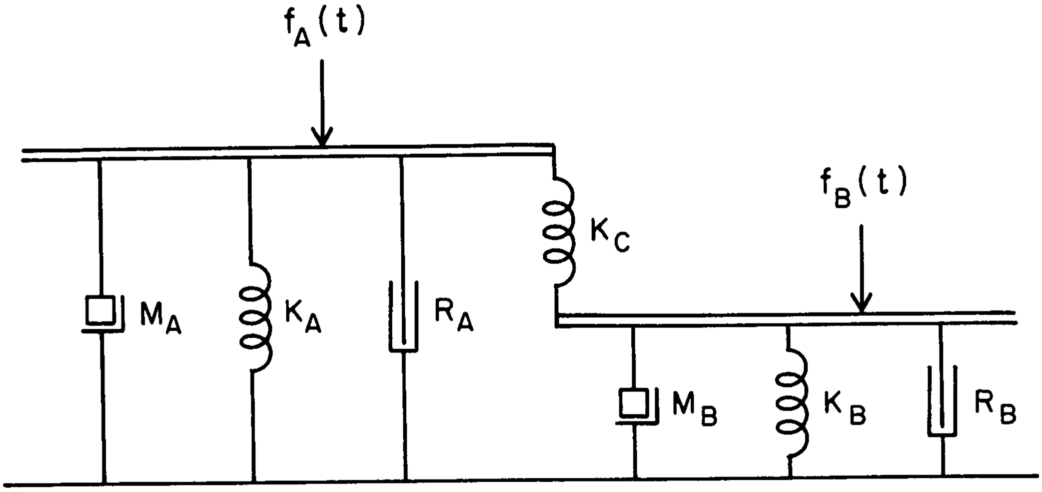

FIG. 4 STIFFNESS COUPLED OSCILLATORS EXCITED BY NOISE

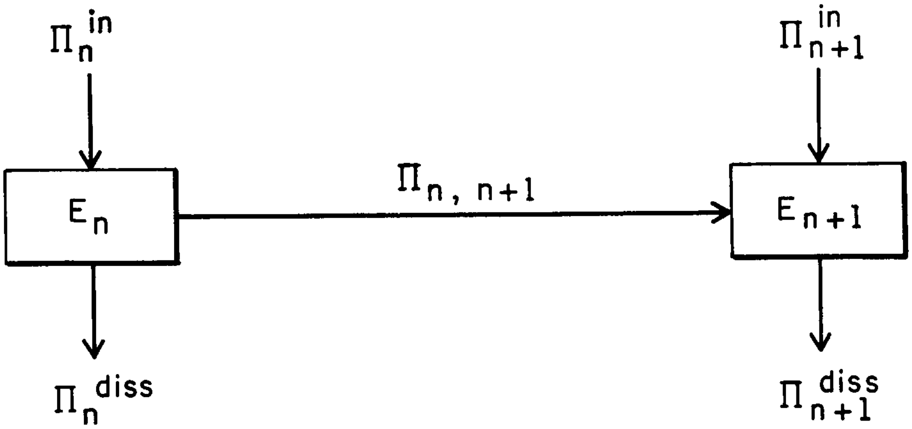

FIG. 5 ENERGY FLOW BETWEEN TWO MULTIMODAL SUBSYSTEMS

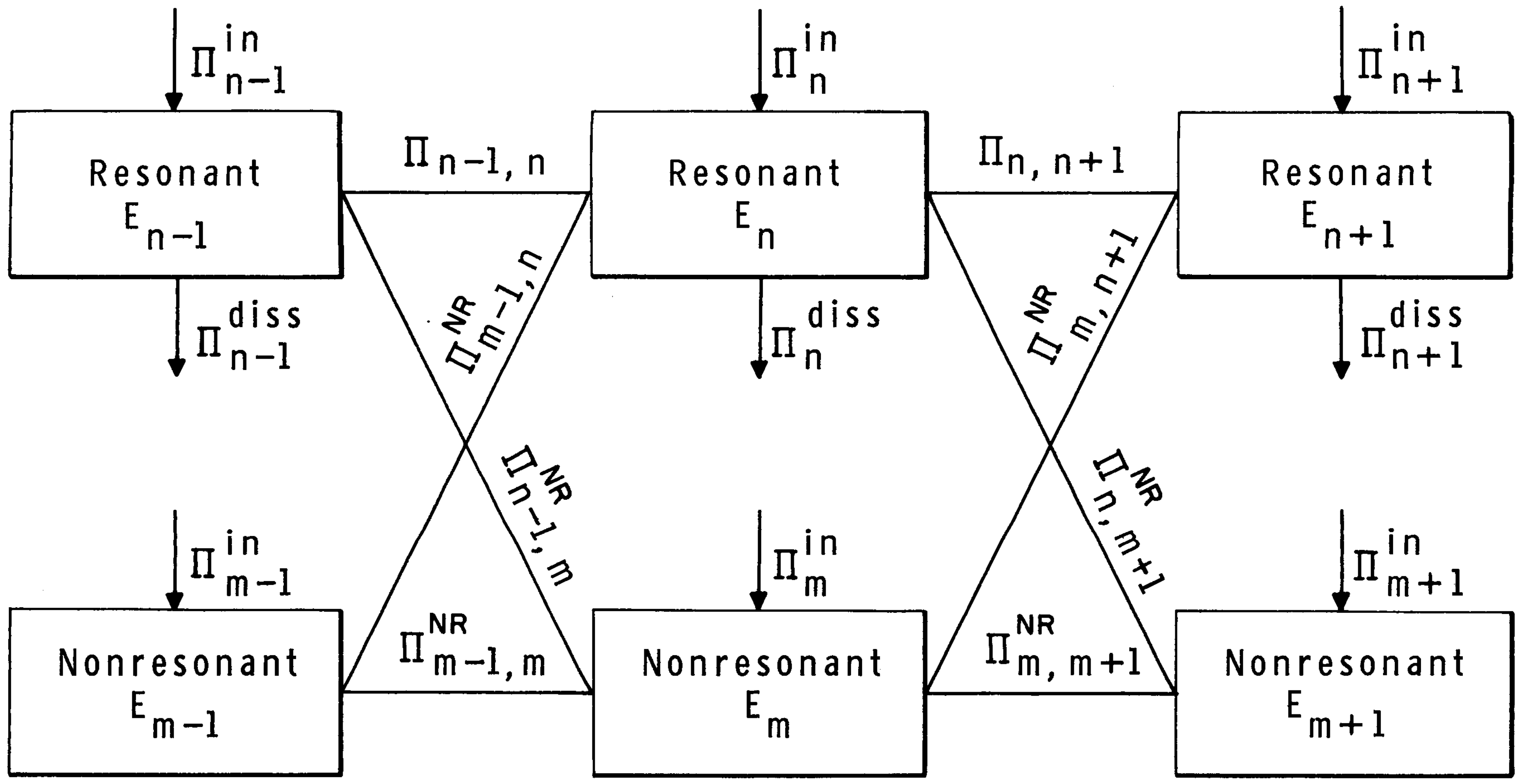

FIG. 6 ENERGY FLOW BETWEEN GROUPS OF MODES EXCITED BY A BAND OF NOISE

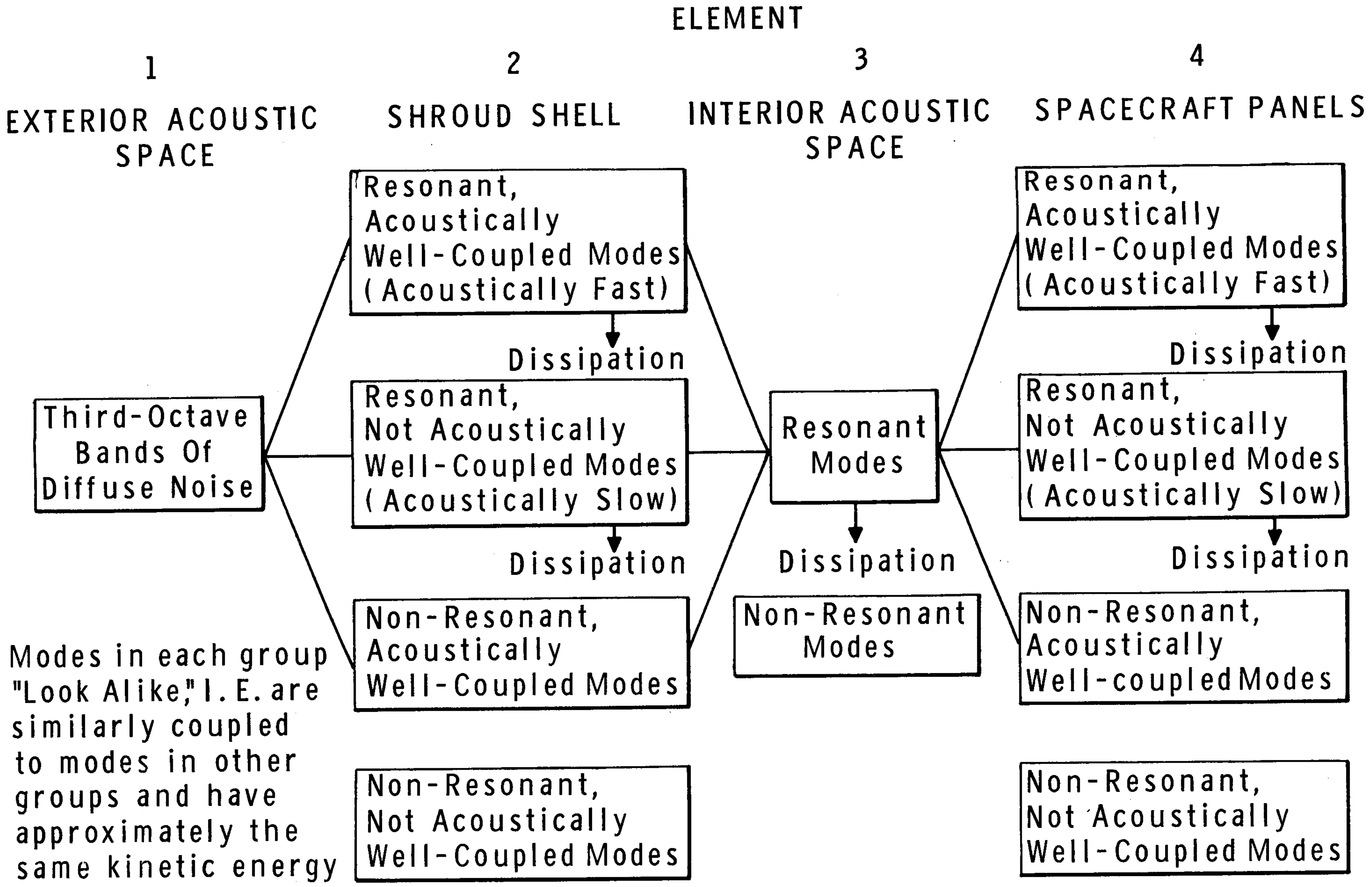

FIG. 7 MODAL GROUPINGS FOR THEORETICAL TREATMENT OF THE ACOUSTIC PATH

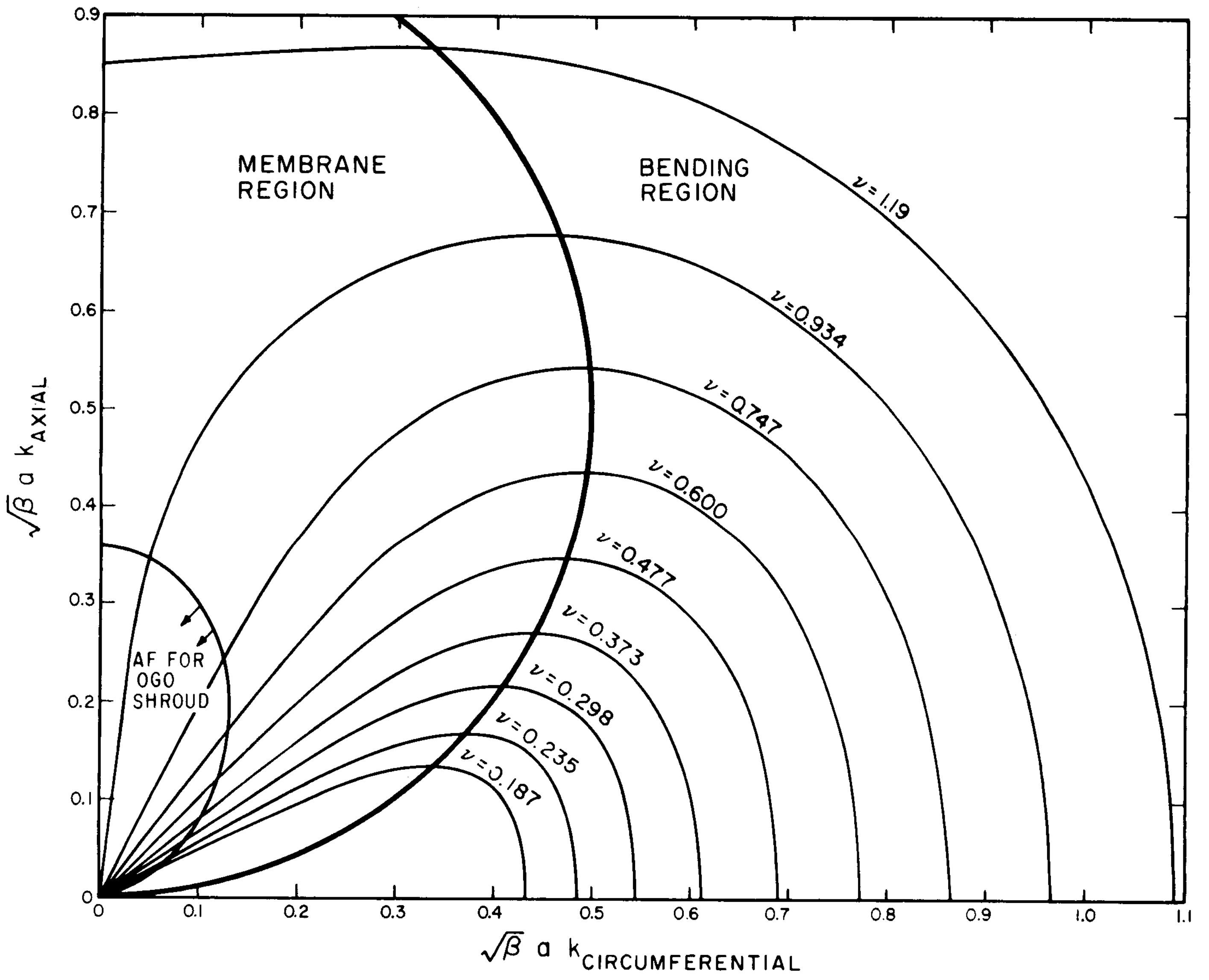

FIG. 8 LINES OF CONSTANT RESONANCE FREQUENCY, ν, AS A FUNCTION OF $\sqrt{\beta}$ a $k_{CIRCUMFERENTIAL}$ AND $\sqrt{\beta}$ a k_{AXIAL} FOR A CYLINDRICAL SHELL

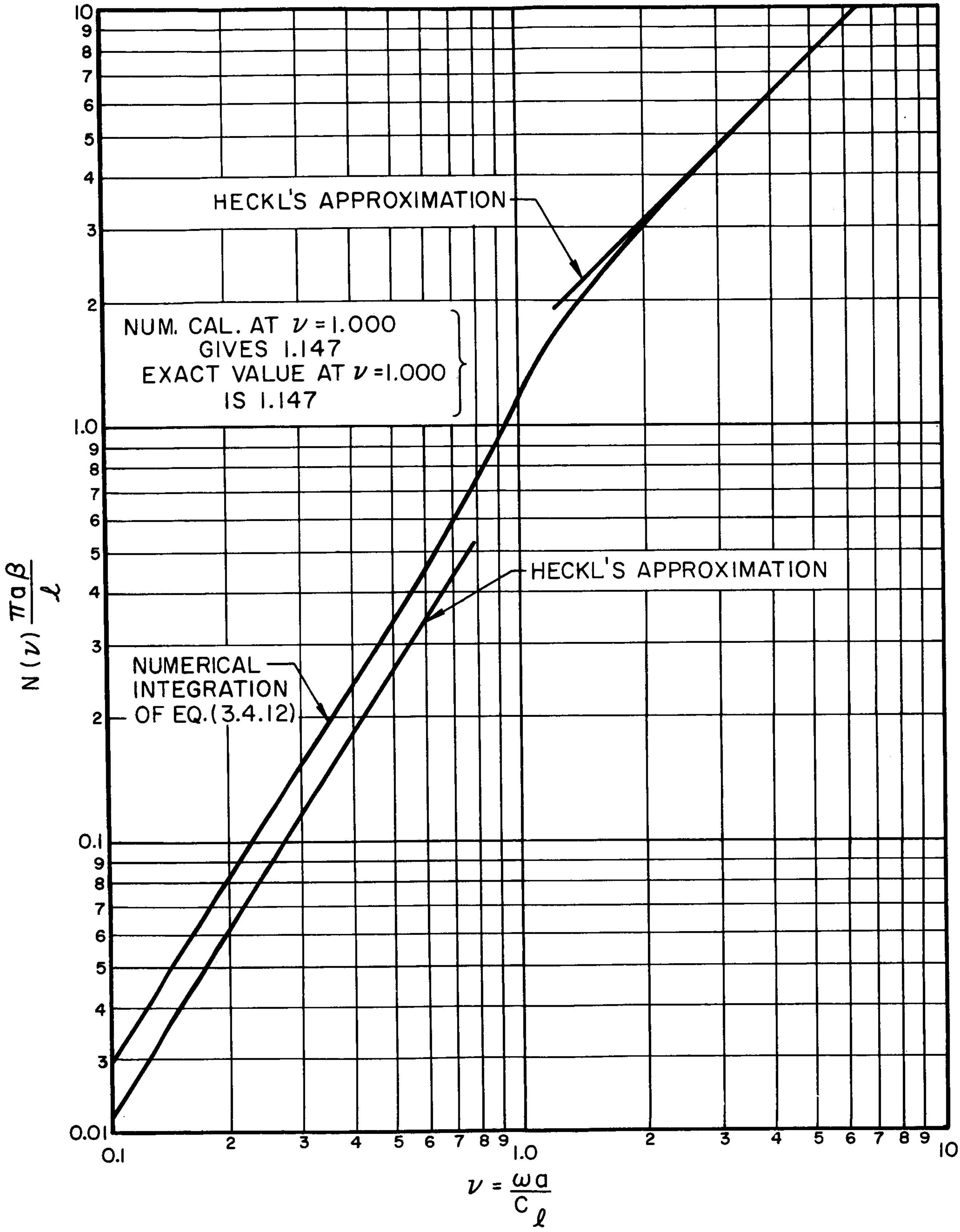

FIG. 9 MODE COUNT FOR A CYLINDRICAL SHELL AS A FUNCTION OF FREQUENCY

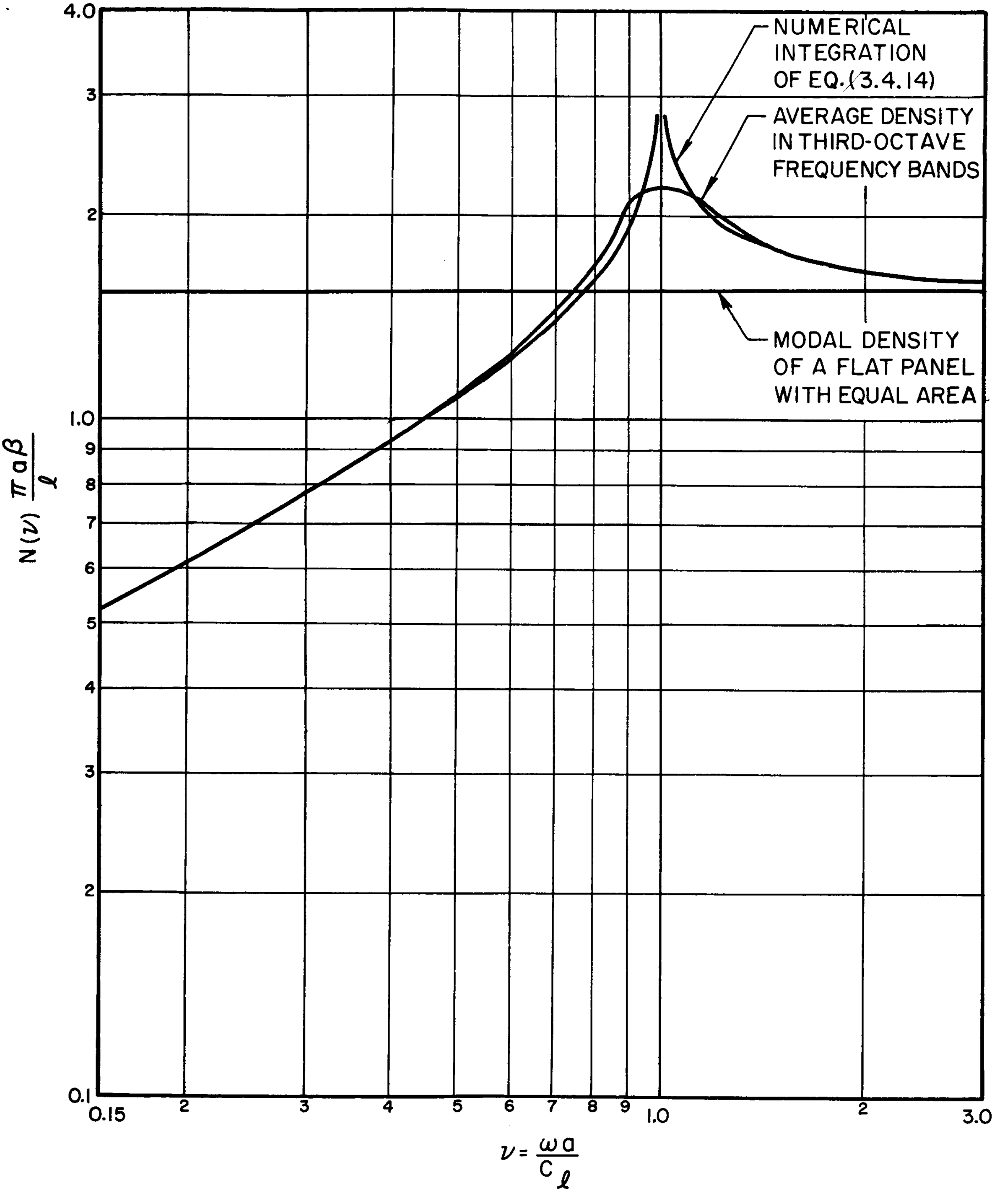

FIG. 10 MODAL DENSITY OF A CYLINDRICAL SHELL AS A FUNCTION OF DIMENSIONLESS FREQUENCY

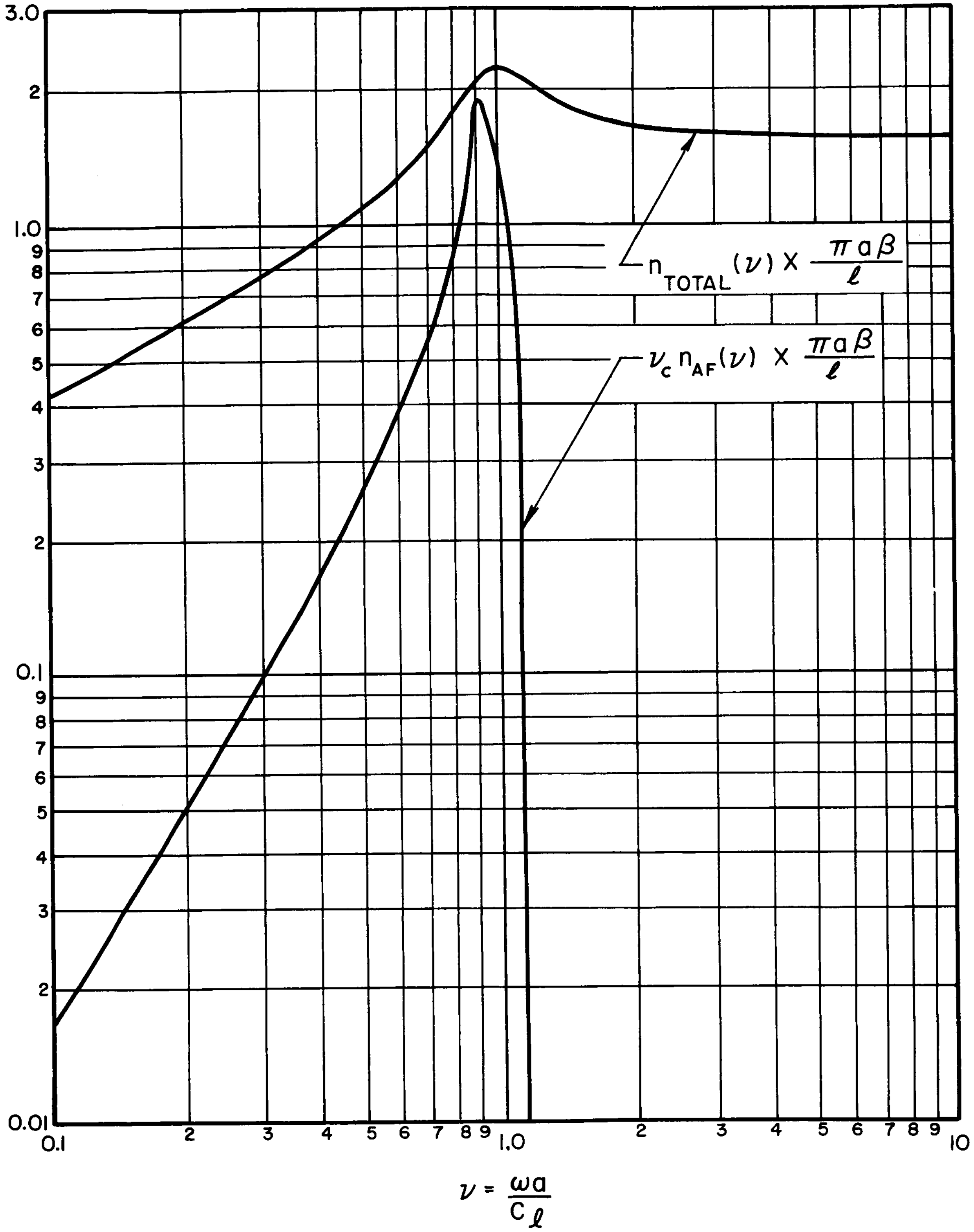

FIG. 11 $n_{TOTAL}(\nu)$ AND $n_{AF}(\nu)$ FOR A CYLINDRICAL SHELL AVERAGED OVER THIRD OCTAVE BANDS AS A FUNCTION OF CENTER FREQUENCY

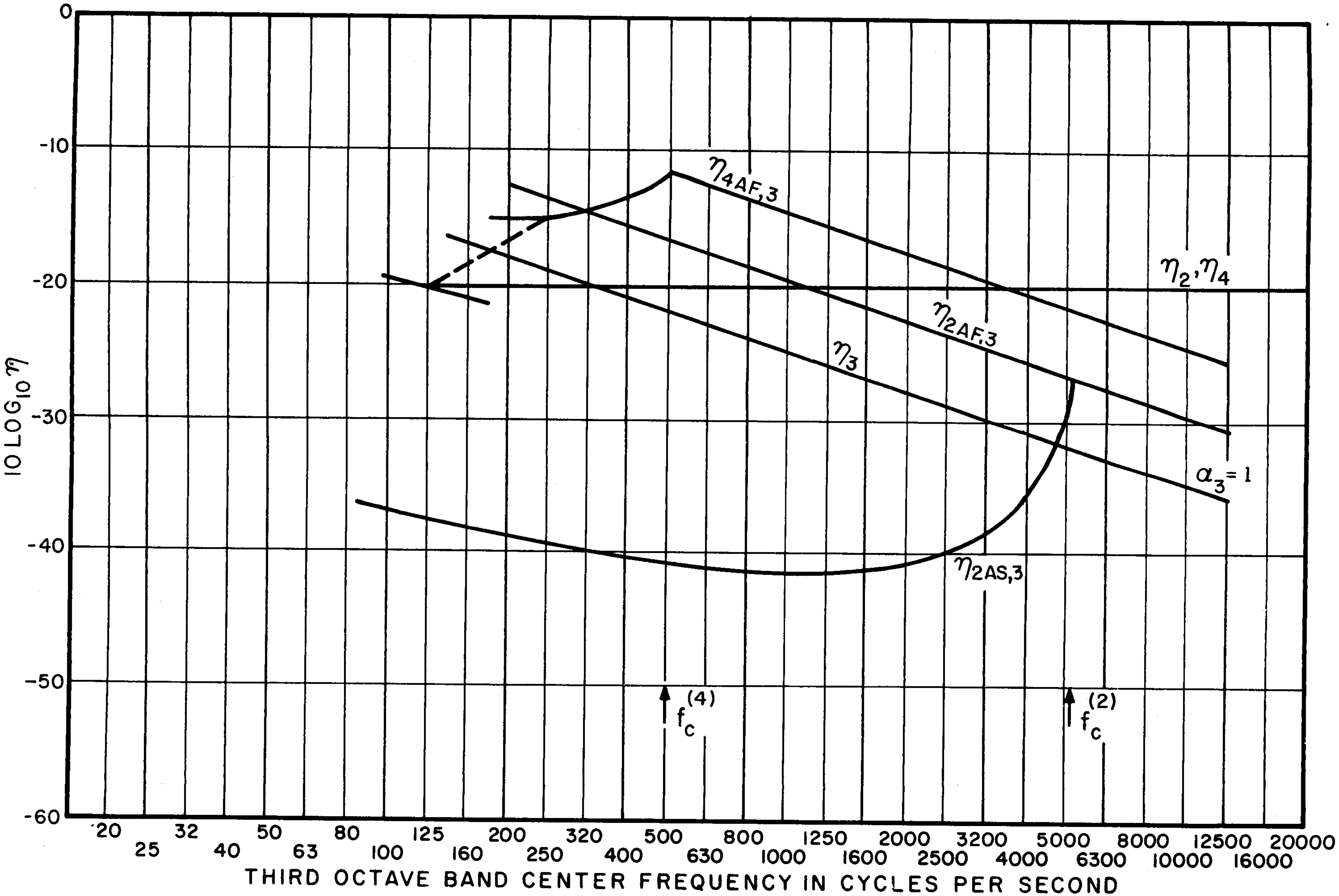

FIG. 12 COUPLING LOSS FACTORS FOR A MODEL OF THE OGO SPACECRAFT ASSEMBLY

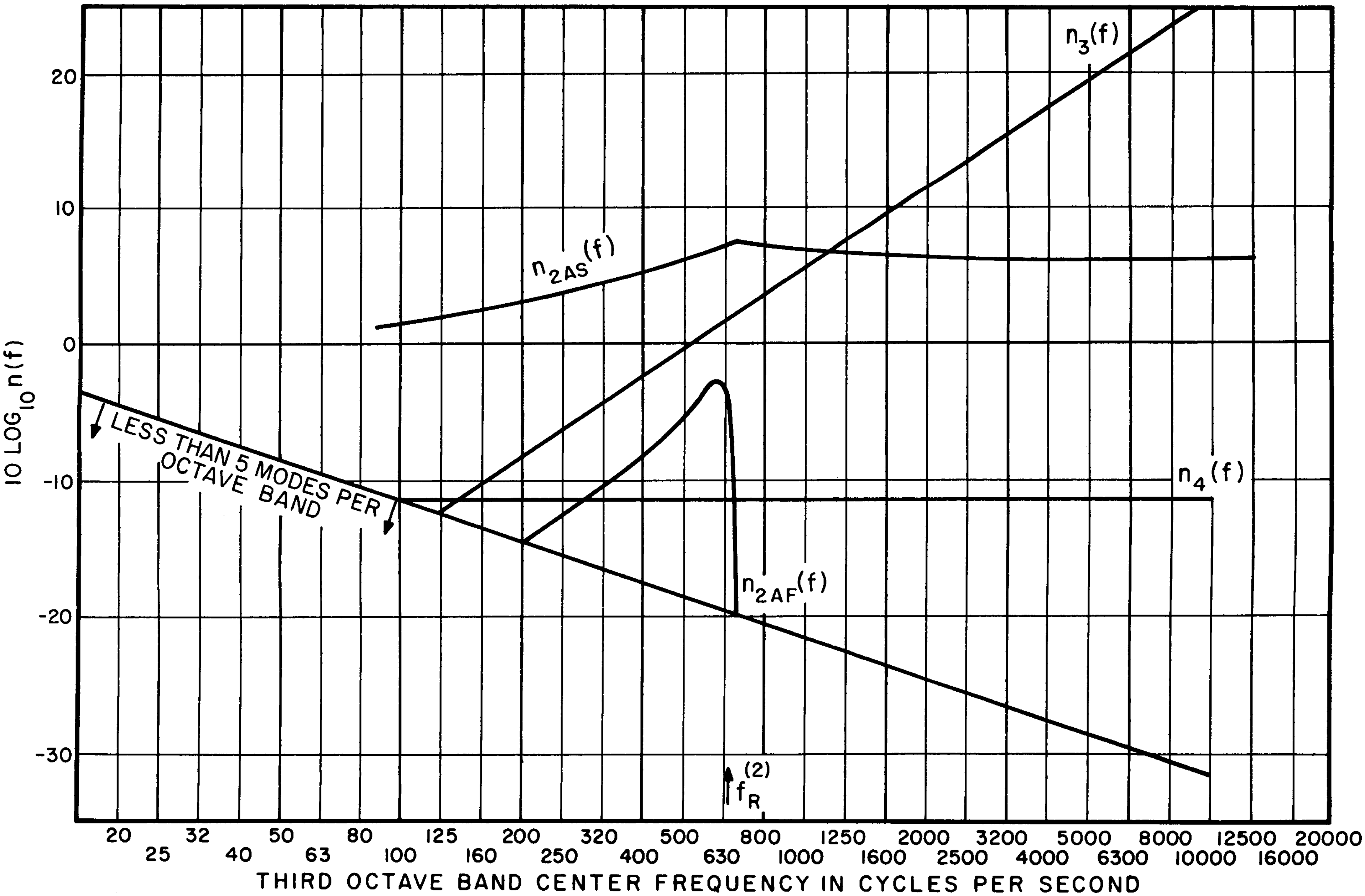

FIG. 13 MODAL DENSITIES FOR A MODEL OF THE OGO SPACECRAFT ASSEMBLY

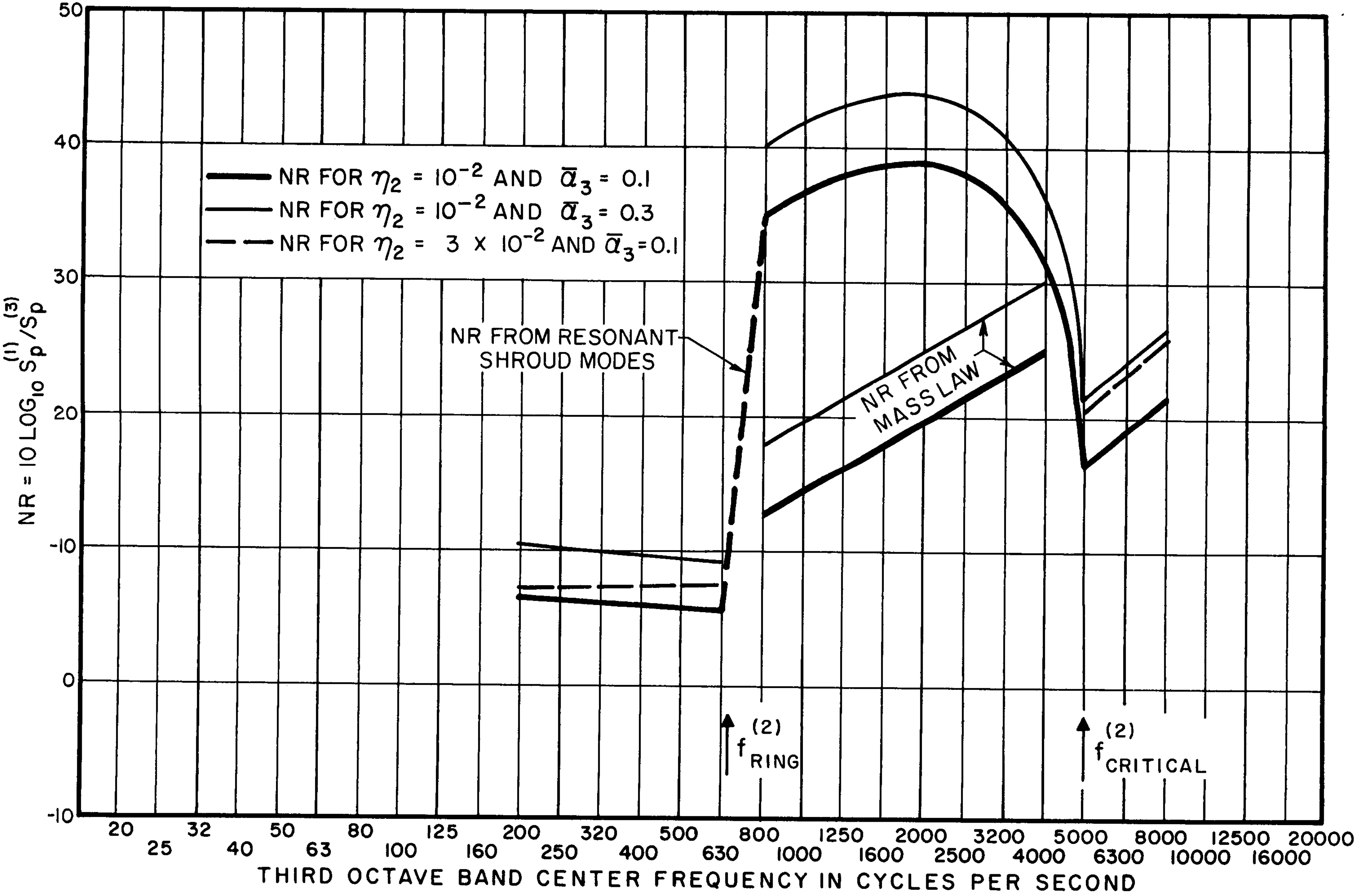

FIG. 14 NOISE REDUCTION BY A MODEL OF THE OGO SHROUD

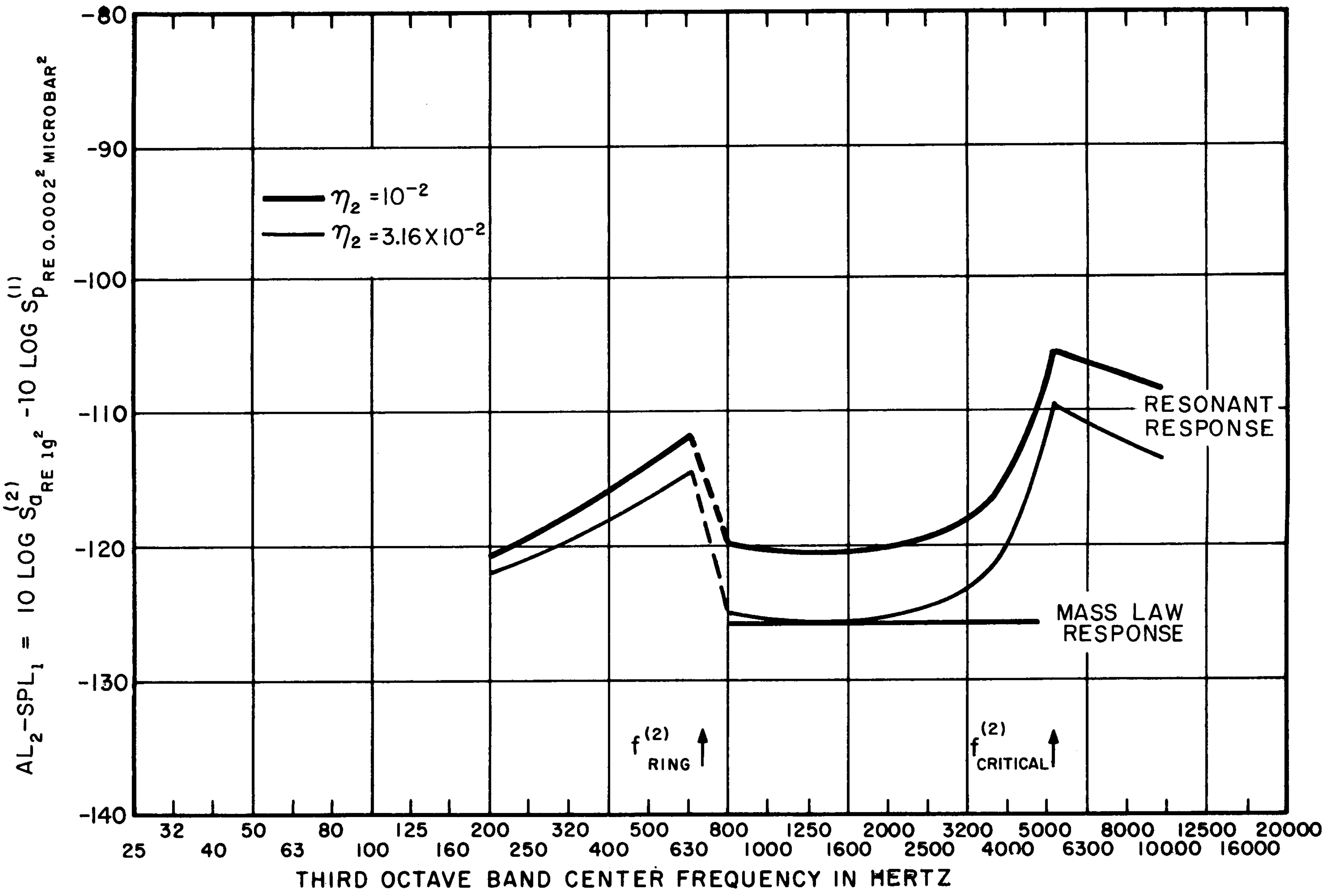

FIG. 15 RESPONSE OF OGO SHROUD MODEL TO THE EXTERIOR ACOUSTIC FIELD

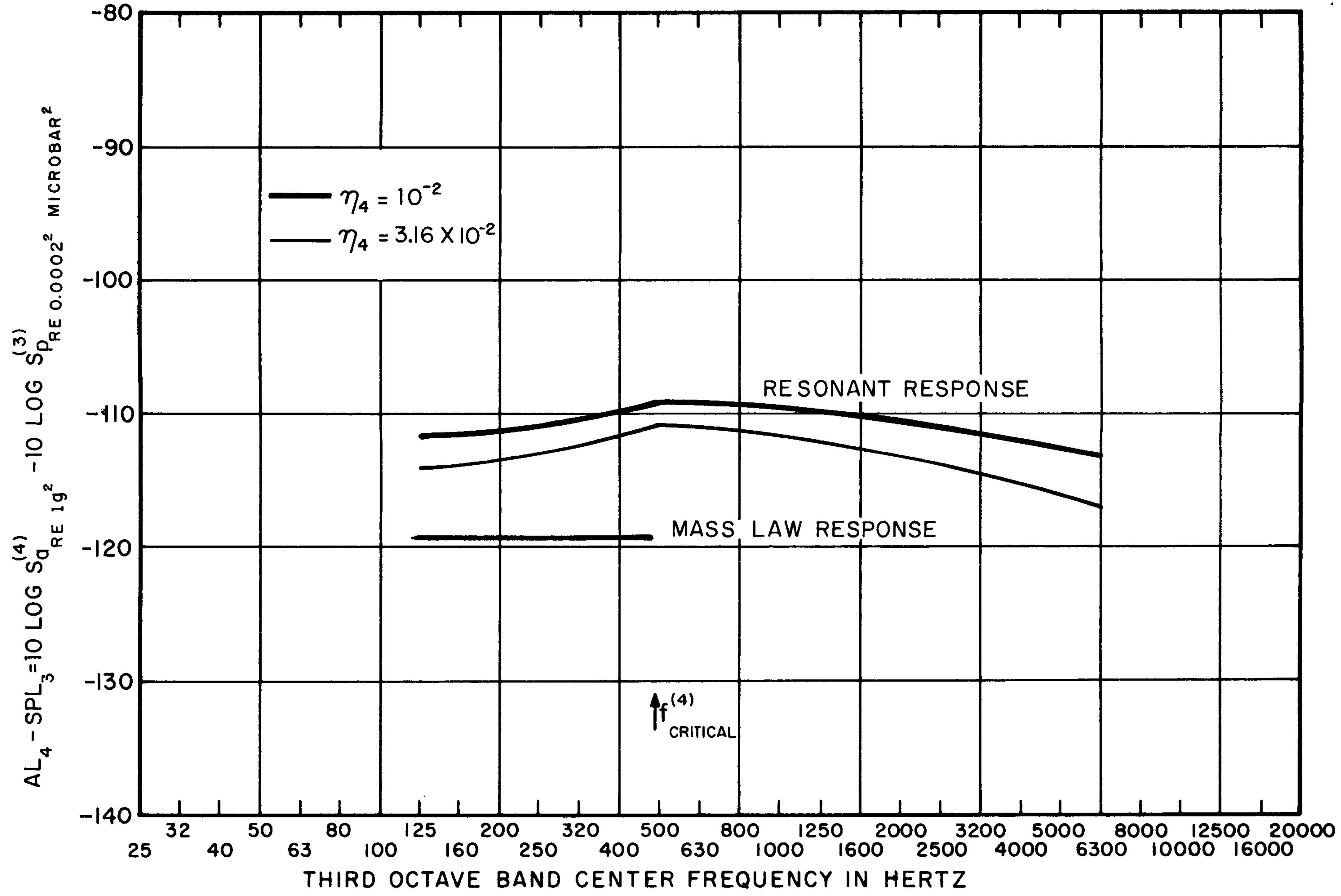

FIG. 16 RESPONSE OF THE OGO SPACECRAFT PANELS TO THE INTERIOR ACOUSTIC FIELD

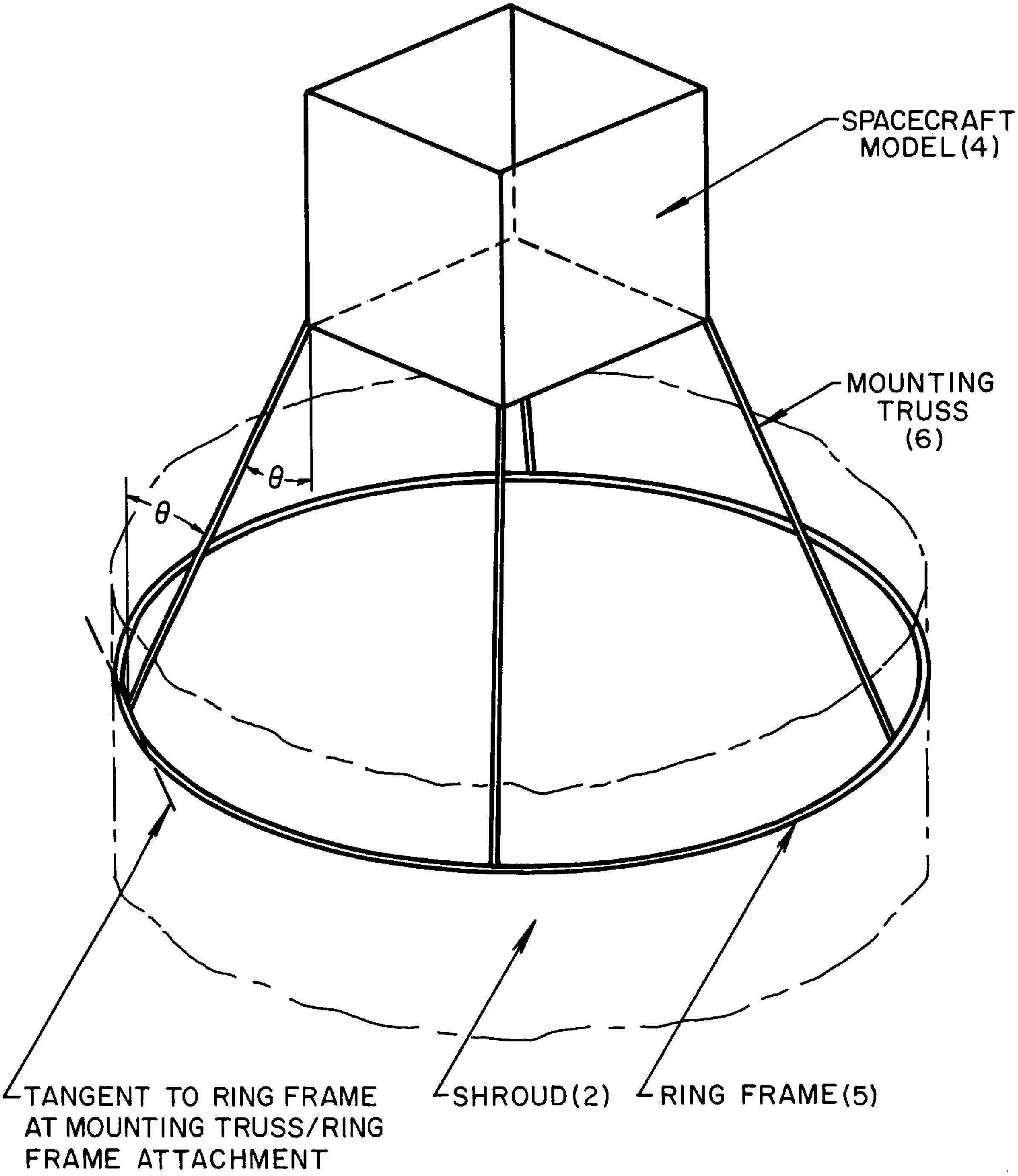

FIG.17 SPACECRAFT MODEL CONNECTED TO RING FRAME BY THE MOUNTING TRUSSES

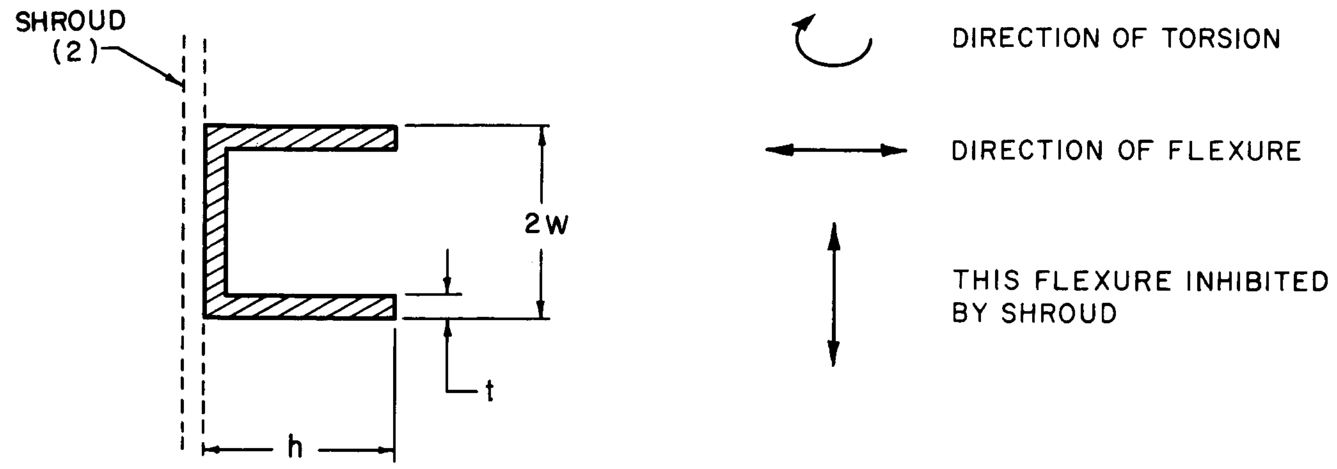

FIG.18 CHANNEL BEAM MODEL OF RING FRAME, ELEMENT (5)

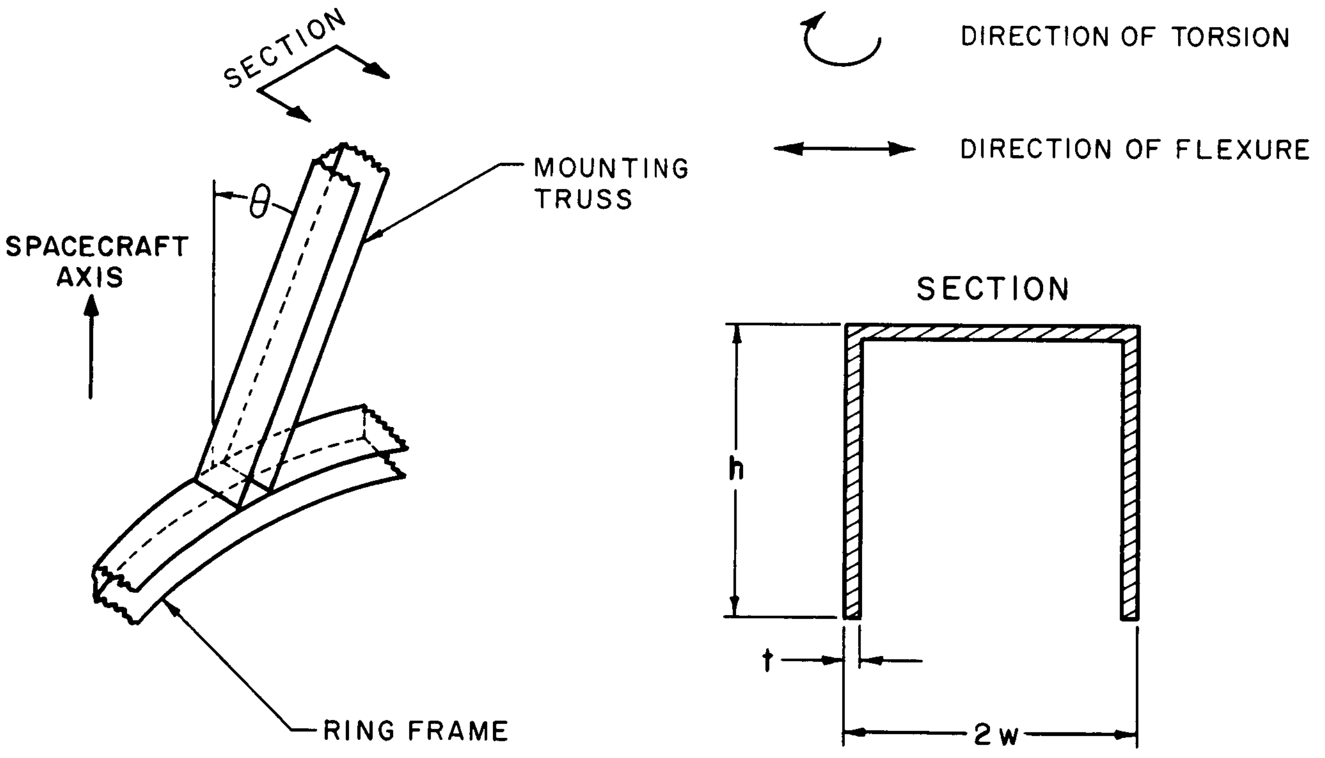

FIG.19 SINGLE CHANNEL BEAM MODEL OF MOUNTING TRUSS, ELEMENT (6)

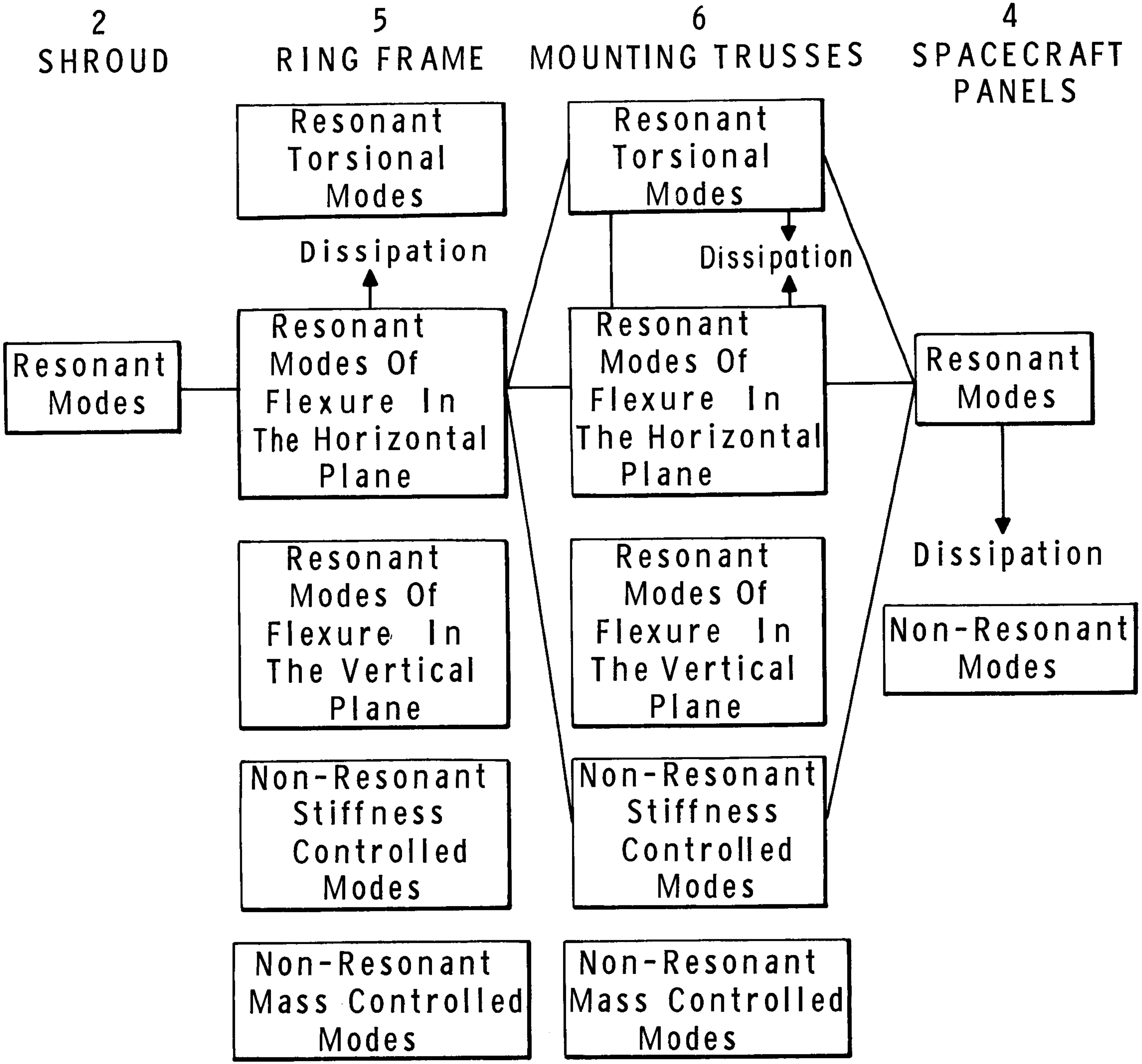

FIG.20 MODAL GROUPINGS FOR THE THEORETICAL TREATMENT OF THE MECHANICAL PATH

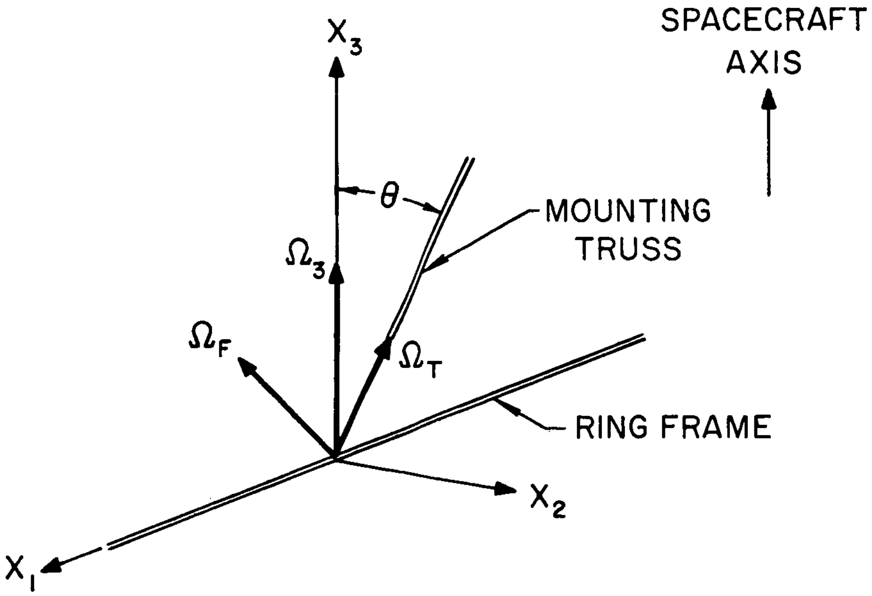

FIG.21 GEOMETRY OF RING FRAME-MOUNTING TRUSS CONNECTION

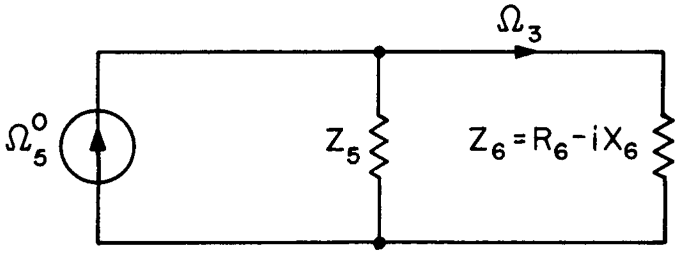

FIG. 22 EQUIVALENT CIRCUIT FOR DETERMINING RESONANT POWER FLOW FROM RING FRAME TO MOUNTING TRUSS

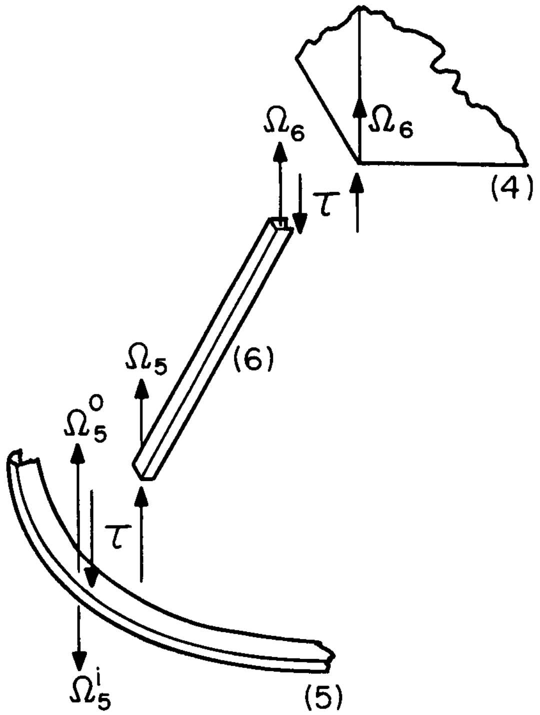

FIG. 23 MOMENT AND ANGULAR VELOCITY DEFINITIONS FOR ANALYSIS OF NONRESONANT MOUNTING TRUSS MOTION

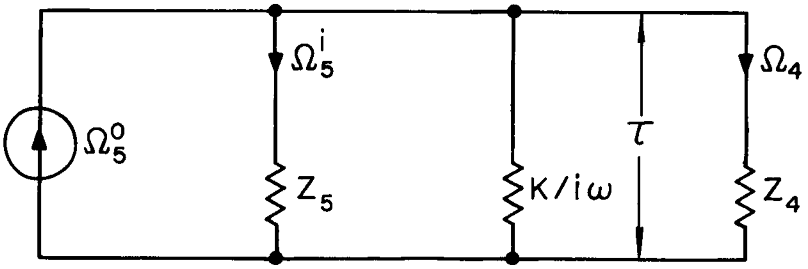

FIG. 24 EQUIVALENT CIRCUIT FOR DETERMINING POWER TRANSMITTED NONRESONANT MOUNTING TRUSS MOTION

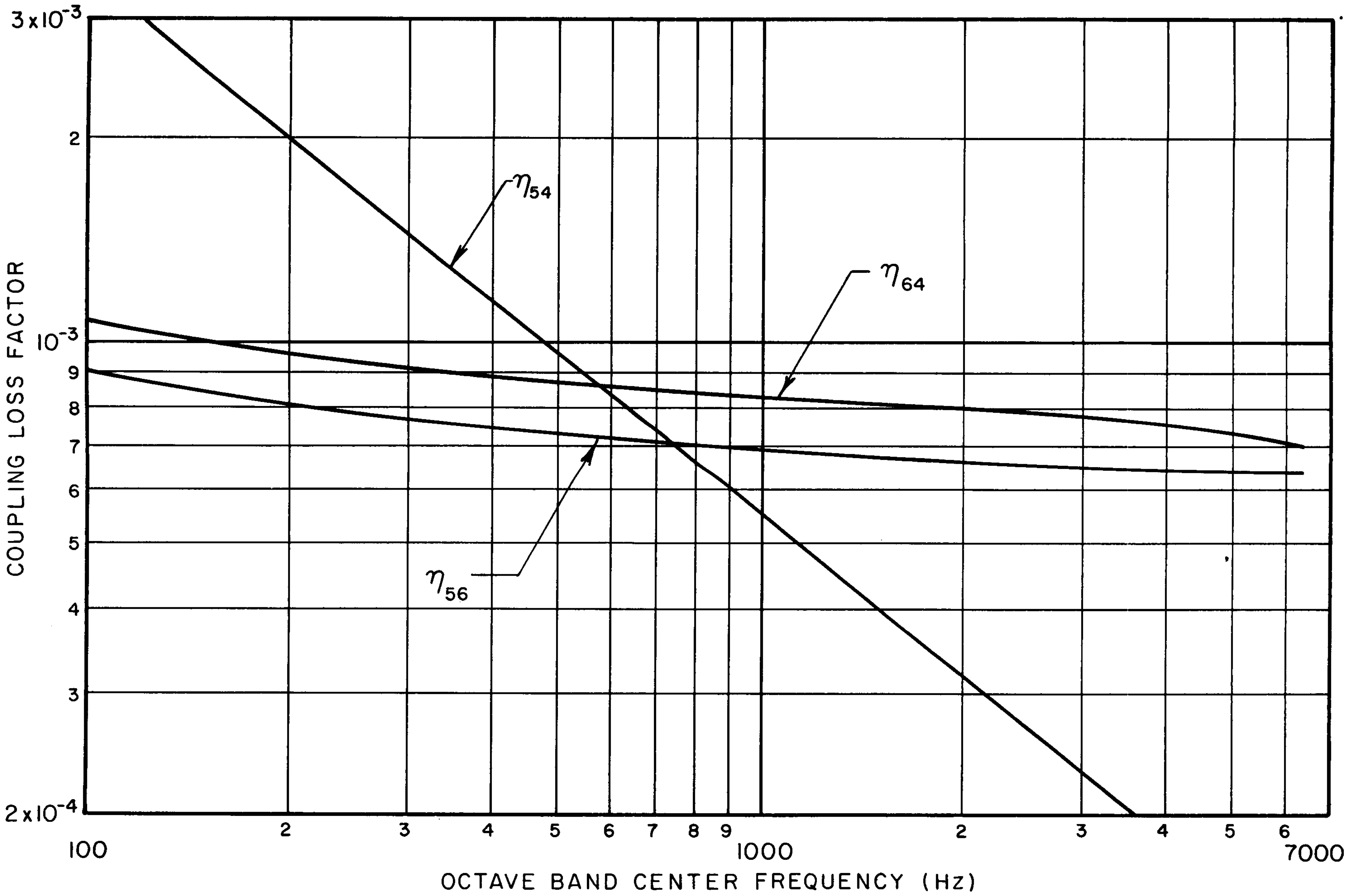

FIG. 25 COUPLING LOSS FACTORS FOR A MODEL OF THE OGO SPACECRAFT ASSEMBLY

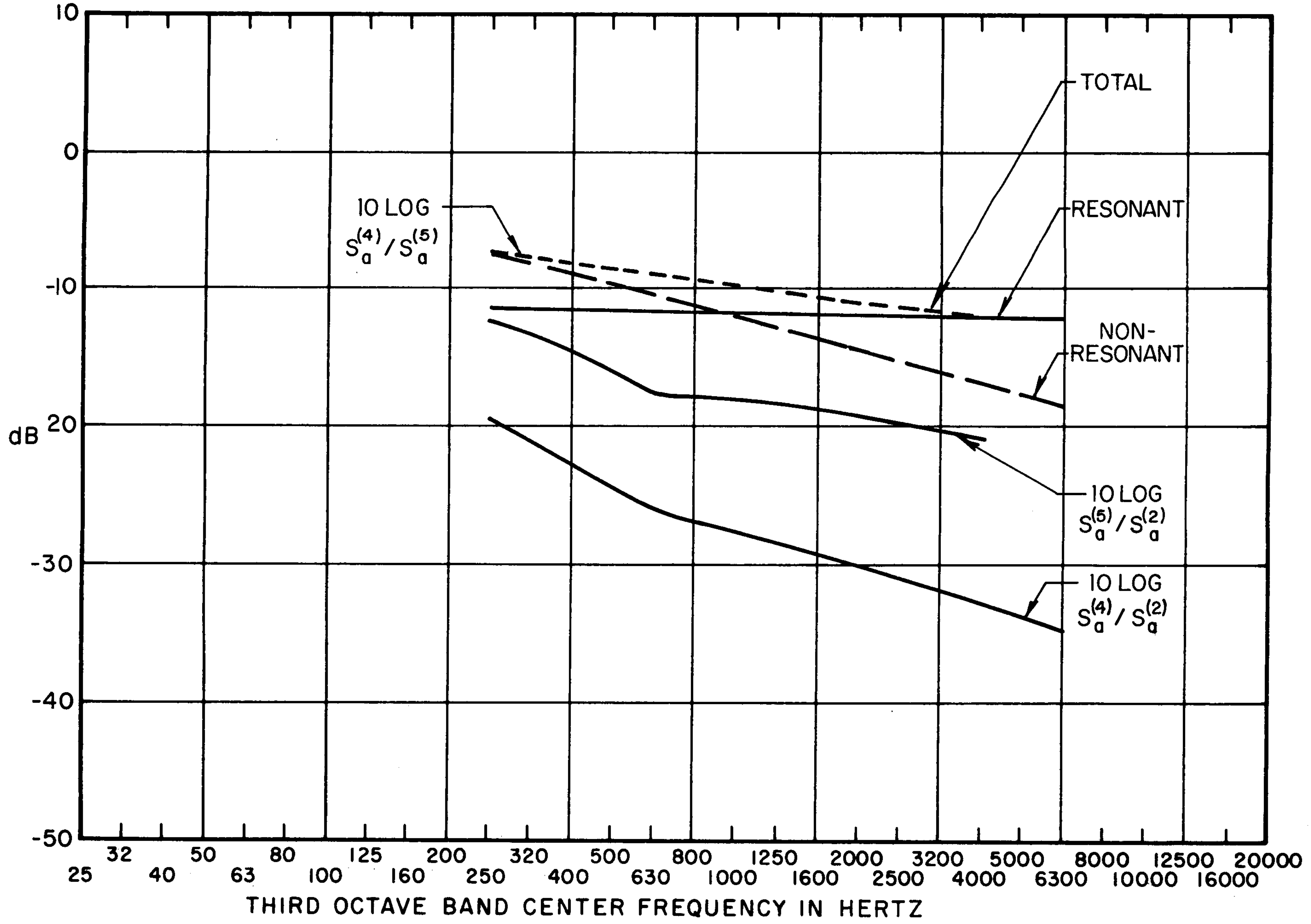

FIG. 26 RESPONSE RATIOS FOR THE ELEMENTS IN THE MECHANICAL TRANSMISSION PATH OF THE OGO MODEL SPACECRAFT ASSEMBLY

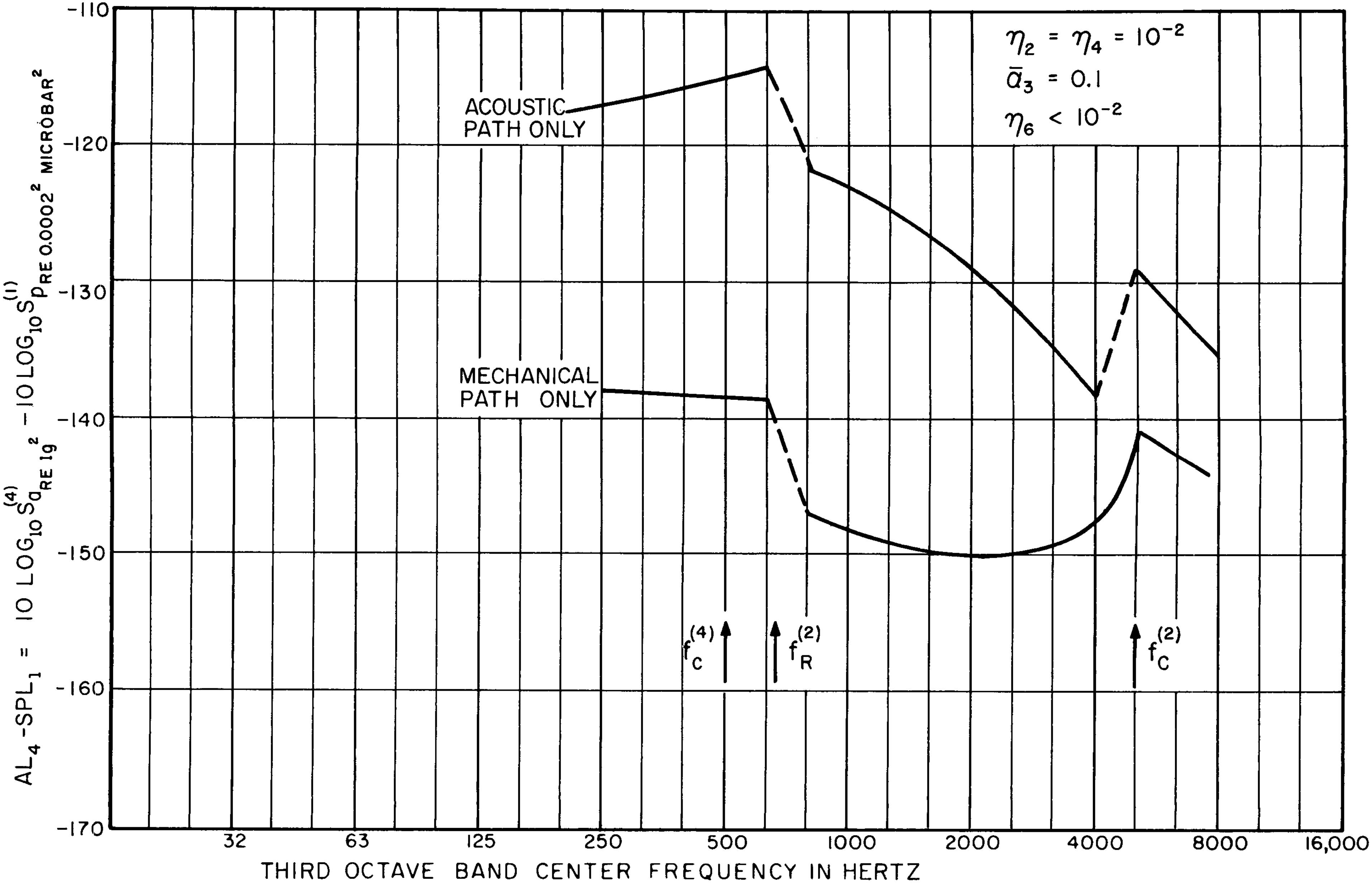

FIG. 27 RELATIVE EXCITATIONS OF SPACECRAFT BY ENERGY TRANSMITTED BY THE ACOUSTIC PATH AND THE MECHANICAL PATH

TABLE I. Parameter values for a model of the OGO spacecraft assembly.

A_2 = 276 ft^2 = 2.56 x 10^5 cm^2
ℓ_2 = 195 in. = 495 cm
ℓ_{2a} = 24 in. = 61 cm base of shroud to first rib
ℓ_{2b} = 30 in. = 76 cm first to second rib
ℓ_{2c} = 34 in. = 86.5 cm second to third rib
ℓ_{2d} = 42 in. = 107 cm third to fourth rib
a_2 = 32.5 in. = 82.5 cm
h = 0.13 in. = 0.33 cm
κ_2 = 0.0366 in. = 0.093 cm
f_r = 650 Hz
f_c = 5200 Hz
M_2 = 1.41 x 10^5 g
β = 0.00113
$c_\ell^{(2)}$ = 11 000 ft/sec = 3.35 x 10^5 cm/sec
ν_c = 8
$\rho_s^{(2)}$ = 1.225 lbs/ft^2 = 0.55 g/cm^2
ρ_o = 1.2 x 10^{-3} cm/sec
c_o = 1100 ft/sec = 3.4 x 10^4 cm/sec
$\rho_o c_o$ = 41 dyn-sec/cm^3
V_3 = 374 ft^3 = 1.07 x 10^7 cm^3
$\bar{\alpha}_3$ ≈ 0.1 (values of 0.1 and 0.3 are used in the calculations)
A_4 = 56.5 ft^2 = 5.25 x 10^4 cm^2 (all four panels included)

TABLE I. (con't)

κ_4	= 0.271 in.	= 0.688 cm
$c_\ell^{(4)}$	= 17 000 ft/sec	= 5.17×10^5 cm/sec
L_y	= 69 in.	= 175 cm (length of the panel in vertical direction)
L_x	= 29.5 in.	= 75 cm (length of one panel in vertical direction)
$\rho_s^{(4)}$	= 0.765 lb/ft^2	= 0.373 g/cm^2
M_4		= 1.96×10^4
f_c	= 500 Hz	
a_5		= 5 cm
t_5		= 0.64 cm
$2w_5$		= 5 cm
ℓ_5	= 204 in.	= 518 cm
$c_\ell^{(5)}$	= 17 000 ft/sec	= 5.17×10^5 cm/sec
$\rho_\ell^{(5)}$		= 25.9 g/cm
M_5		= 1.34×10^4 g
a_6		= 8.9 cm
t_6		= 0.152 cm
$2w_6$		= 7.6 cm
ℓ_6		= 200 cm (length of all four trusses)
$c_\ell^{(6)}$		= 5×10^5 cm/sec
$\rho_\ell^{(6)}$		= 10.4 g/cm
M_6		= 2.08×10^3 g(mass of all four trusses)